*Mineralogical Magazine* (2019), **83**, 123–135
doi:10.1180/mgm.2018.138

CAMBRIDGE UNIVERSITY PRESS

**Article**

# A hibonite-spinel-corundum-hematite assemblage in plagioclase-clinopyroxene pyrometamorphic rocks, Hatrurim Basin, Israel: mineral chemistry, genesis and formation temperatures

Victor V. Sharygin

Institute of Geology and Mineralogy SB RAS, pr. Koptyuga 3, Novosibirsk, 630090, Russia; and Novosibirsk State University, ul. Pirogova 2, Novosibirsk, 630090, Russia; and Institute of Physics and Technology, Ural Federal University, ul. Mira 19, Ekaterinburg, 620002, Russia

**Abstract**

The intergrowths of Fe-rich corundum + Al-rich hematite + spinel + hibonite have been found as an assemblage in a plagioclase-clinopyroxene rock (paralava, former hornfels) at the Hatrurim Basin, Hatrurim combustion metamorphic Formation. Most spinels show oriented exsolution structures and vary from $(Mg_{0.75}Fe^{2+}_{0.25})(Al_{1.80}Fe^{3+}_{0.20})O_4$ (with exsolutions) to $(Mg_{0.77}Fe^{2+}_{0.23})(Al_{1.95}Fe^{3+}_{0.05})O_4$ (homogeneous) indicating a tendency towards magnesioferrite and magnetite, and enrichment in NiO (up to 1.9 wt.%) and ZnO (up to 1.4 wt.%). Hibonite is Ti rich ($TiO_2 > 8$ wt.%) and close to $CaAl_9Fe^{3+}(Mg,Fe^{2+})TiO_{19}$. Corundum varies in $Fe_2O_3$ (4.2–11.8 wt.%). Hematite is also inhomogeneous and contains oriented exsolution structures of corundum. It shows variable concentrations of $TiO_2$ (0.7–5.6 wt.%), $Al_2O_3$ (0.7–8.6 wt.%), $Cr_2O_3$ (0.2–1.5 wt.%), $V_2O_3$ (0.1–1.0 wt.%) and MgO (0.3–2.0 wt.%). Crystallization of this specific assemblage is assumed to be at 1000–1200°C using evaluations for the corundum hematite pair with reference to published experimental data. The active role of superheated oxidised volatiles is suggested during both crystallisation of this corundum-bearing association and host-rock transformation (melting event for hornfels → paralava).

**Keywords:** corundum, hematite, hibonite, paralava, hornfels, corundum-hematite geothermometer, combustion metamorphism, Hatrurim Basin, Israel

(Received 2 November 2017; accepted 20 May 2018)

## Introduction

The Hatrurim Formation (also known as the 'Mottled Zone') is a unique complex of pyrogenic rocks involving various larnite, spurrite and other Ca-rich rock types from solid-state metamorphic rocks to paralavas. Previously, the mineral assemblages of the Hatrurim Formation were interpreted to indicate maximum temperatures of combustion metamorphism of 1000°C to 1100°C (Gross, 1977). The Hatrurim Formation has become a 'mineralogical Mecca' due to numerous new minerals being found in these unique rocks. In general, these discoveries were initiated due to the now famous works of Sh. Gross and Y. Bentor (Bentor *et al.*, 1963; Gross, 1977 and others). In last decade more than 20 new minerals have been found within the Hatrurim Formation: barioferrite; shulamitite; murashkoite; zadovite; gurimite; vapnikite; nabimusaite; aradite; gazeevite; fluormayenite; fluorkyuygenite; negevite; halamishite; zuktamrurite; silicocarnotite; flamite; tululite and others (Murashko *et al.*, 2011; Sharygin *et al.*, 2013; Galuskin *et al.*, 2014; 2015*a*–*c*; 2016; 2017; Galuskina *et al.*, 2014; 2017*a*,*b*; Britvin *et al.*, 2015; Sokol *et al.*, 2015; Khoury *et al.*, 2016). Most of these were identified in larnite and spurrite rocks and Ca-rich paralavas; and some could be used as indicator minerals to estimate the history of the rock formation. For example, shulamitite (+ Fe-perovskite) from the Hatrurim Basin larnite rocks indicates crystallisation under high temperatures (1150–1170°C) and low pressures (high-*T*-region of the spurrite–merwinite facies) (Sharygin *et al.*, 2008*a*; 2013). Coexistence of flamite and larnite in the Hatrurim Ca-Al-rich paralavas reveals a specific cooling history (quenching of melt) during their solidification (Sokol *et al.*, 2015). Estimating the formation temperatures is possible for the Hatrurim Formation Ca-rich silica-undersaturated rocks, but remains problematic for more silicic plagioclase-clinopyroxene hornfels and paralavas, due to the lack of indicator minerals. Investigation of different plagioclase-clinopyroxene paralavas has indicated minimal melting temperatures of >1100°C (Vapnik *et al.*, 2007), whereas the temperature regime of the same hornfels (solid phase transformation) remains enigmatic.

Corundum and hematite are rarely associated in terrestrial rocks, but sometimes occur in Al-rich metamorphic rocks after bauxites and laterites (Feenstra *et al.*, 2005 and references therein). Exsolution of hematite in gem-quality corundum of metamorphic or magmatic origin and reverse exsolution structure

**Author for correspondence:** Victor V. Sharygin, E-mail: sharygin@igm.nsc.ru
**Associate Editor:** Craig Storey
**Cite this article:** Sharygin V.V. (2019) A hibonite-spinel-corundum-hematite assemblage in plagioclase-clinopyroxene pyrometamorphic rocks, Hatrurim Basin, Israel: mineral chemistry, genesis and formation temperatures. *Mineralogical Magazine*, **83**, 123–135. https://doi.org/10.1180/mgm.2018.138

(corundum in hematite or another Fe-oxide minerals) are also rare phenomena (Feenstra *et al.*, 2005 and references therein; Kulikova and Varlamov, 2006; Izokh *et al.*, 2010). Fe-rich corundum, hibonite, dorrite-like minerals, Mn-Al-rich hematite and magnesioferrite have been found as a spongy aggregate in vugs from one of the 'metacarbonate nuts' of a burnt dump of the Kalinin coal mine, Donets coal basin, southeast Ukraine (Sharygin, 2010). The Fe-rich corundum + Al-rich hematite + spinel + hibonite assemblage in the Hatrurim plagioclase-clinopyroxene rock was described briefly in a previous publication (Sharygin *et al.*, 2008*b*). The present paper provides more details of the rock mineralogy, with implications for formation conditions of the specific Fe–Al–Mg-oxide assemblage.

## The Hatrurim Basin and the Hatrurim Formation: geological background

The Hatrurim Formation (Mottled Zone, MZ) complexes are located in the vicinity of the Dead Sea Transform (Gross, 1977; Novikov *et al.*, 2013), which is a prominent shear zone separating the Arabian plate from the Sinai microplate (Supplementary Fig. S1, based on data from Bentor and Vroman, 1960; Bentor *et al.*, 1965; Picard and Golani, 1965; Nissenbaum and Goldberg, 1980; Burg *et al.*, 1991, 1999; Gardosh *et al.*, 1997, 2008; Shen *et al.*, 1998; Hall *et al.*, 2005; Sokol *et al.*, 2007, 2010, 2014c; Hirsch *et al.*, 2010). The Dead Sea Transform system consists of six major, left-stepping strike-slip faults with deep rhomb-shaped depressions between each fault pair, the largest one is the Dead Sea basin. This depression is boarded by uplifted margins and filled with up to 10 km thick Miocene to Holocene sediments (Garfunkel, 1997; Maercklin, 2004). Along the eastern shore Lower Cretaceous to Cambrian Nubian sandstones are exposed, whereas the western margin is composed of a Permian to Cretaceous sedimentary sequence ~4 km thick. The Upper Cretaceous – Lower Tertiary marine sediments cover the area almost continuously and consist of limestone, chalk (including bituminous varieties), and dolomite with marl, phosphorite and chert intercalations (Zeigler, 2001; Hall *et al.*, 2005). The widths of Dead Sea Transform-related damage zones, consisting of minor fault fractures and fracture networks, range from metres to several hundreds of metres, and control the ascending fluid flow from subsurface (Gardosh *et al.*, 1997; Gvirtzman and Stanislavsky, 2000; Sokol *et al.*, 2014*c*). The ongoing activity appears as saline springs and methane outbursts from shallow wells, as well as famous asphalt floating blocks and 'springs' in the southern Dead Sea (Nissenbaum and Goldberg, 1980).

Tectonically, shores of the Dead Sea basin are composed of a series of step-faulted blocks (Garfunkel, 1997). The south-western shoulder of the rift within the Masada-Zohar block is prominent due to hydrocarbon accumulations, namely small commercial gas fields (Zohar, Kidod and Haqanaim) as well as non-commercial heavy oil (at Gurim-1 and -2) and light oil (Zuk-Tamrur-1) (Gardosh *et al.*, 1997). The Hatrurim Basin (11.3 km × 7.3 km, 47.8 km$^2$, Bentor and Vroman, 1960), one of the largest Mottled Zone complexes, is also located within the Masada-Zohar block (31°12′N, 35°16′E) (Fig. S1 A,B).

The specific non-stratigraphic unit of the MZ rocks lies at the top of the Upper Cretaceous – Lower Tertiary section of the area and reaches depths from 30–40 to 120 m below the surface (Fleischer and Varshavsky, 2002). The term 'MZ sequence' involves diverse sedimentary rocks, which underwent post-depositional alteration under different conditions. The section consists mainly of unevenly distributed brecciated sediments (mainly chalk enclosing phosphorite, chert and marl), which have undergone extensive low-temperature hydrothermal alteration and are cut by abundant veinlets containing calcite, aragonite, gypsum, various hydrated Ca-silicates, zeolites and ettringite. The uppermost part of the same section includes numerous foci of diverse anhydrous high- to ultrahigh-temperature combustion metamorphic rocks.

The conical hills are a characteristic feature of the geomorphology of the Hatrurim Basin. The low and middle parts of these hills are represented by the middle-temperature combustion metamorphism rocks: spurrite marbles ($T$ ~700–800°C). Relatively fresh marbles (rare) as well as their hydrated varieties (common) up to 4 m thick cover large areas and rim a set of circle structures with diameters from a few hundred metres to a few kilometres (Fig. S1 C). The upper part consists typically of coarse-clastic breccias with lumps of marl, limestone, phosphorite and flint from strata below. Occurrences of the rocks of the so-called 'olive unit' (Gross, 1977; Burg *et al.*, 1991) are confined to the top of the hills. These highly-porous rocks are composed mainly of calcite and zeolites, which cemented the quartz sand and clasts of the sediments below. They commonly form specific swells and structures of 'plugged land' (Vapnik *et al.*, 2007). The concentric swells (zones) are of high-temperature clinopyroxene-anorthite hornfels with paralava lenses and veinlets of the same mineral composition. The zones of calcination and metamorphism of parent marly sediments produce hornfels. The depth of these hornfel zones does not exceed 3 m. A supply channel now filled with brecciated sediments with carbonate and/or zeolite cement has been observed for some bodies. They form sharp downward cones 12–20 m deep (Vapnik *et al.*, 2007).

The high-temperature larnite-bearing rocks ($T$ = 1000–1400°C) were observed at several levels of the Hatrurim Formation section, mainly in the northern and central parts of the Hatrurim Basin (Fig. S1). In the lower section within 20 m above its basement, they are from a few tens of centimetres to a few metres thick and neighbour bodies of gehlenite hornfels. Both larnite and gehlenite combustion metamorphism rocks transform easily into the so-called 'pseudo-conglomerates' by retrograde hydration and/or carbonation. The secondary products are mainly calcite, aragonite, gypsum, ettringite and minor Ca silicate-hydrates. Up section, larnitic rocks occur as isolated mottles (to 10 m across) among extensively altered varieties. At hilltops, monolithic larnite rocks make up separate isometric massive blocks, plates or cliff scarps, up to 50 m across and 10 m thick (Gross, 1977, 1984; Burg *et al.*, 1991; Sharygin *et al.*, 2008*a*, 2013; Sokol *et al.*, 2014*b*; Galuskina *et al.*, 2015*a*–*c*). Descriptions of individual bodies of these rocks at the Hatrurim Basin are given in many publications (e.g. Kolodny and Gross, 1974; Gross, 1977; Burg *et al.*, 1991, 1999; Vapnik *et al.*, 2007; Sharygin *et al.*, 2008*a*; 2013; Sokol *et al.*, 2008; 2014*b*; Novikov *et al.*, 2013; Galuskina *et al.*, 2015*a*,*c*).

Many authors interpreted the Hatrurim Formation complexes as products of *in situ* combustion of low-calorific fuel, specifically, disseminated bituminous matter of marine chalk (Bentor *et al.*, 1963; Burg *et al.*, 1991; 1999; Khoury and Nassir, 1982; Techer *et al.*, 2006). Other authors attributed combustion metamorphism events within the Hatrurim Formation complexes to local breakthrough and ignition of high-calorific hydrocarbon gases, mainly methane, which might be derived from mud volcanism (Gilat, 1998, Vapnik *et al.*, 2007; Sharygin *et al.*, 2008*a*,*b*; 2013; Seryotkin *et al.*, 2012; Sokol *et al.*, 2008; 2010; 2014*b*; Novikov *et al.*, 2013). The mud volcanism is spatially and structurally related to the neotectonic movements, folds and deformation

zones, and may be considered as a response to the development of the Red Sea Fault and Levantine Transform Fault (Novikov *et al.*, 2013). According to $^{40}Ar/^{39}Ar$ radiometric age determination of different MZ rocks (Gur *et al.*, 1995; Sokol *et al.*, 2014*a*) the processes of fluid impact and further gas ignition occasionally occurred in the 7–0.5 Ma range, which corresponds to the main (most active) stage of the opening of the Dead Sea rift (Maercklin, 2004). Emissions of hydrocarbon gases in the geological past left an imprint in abundant foci of high- (800–1100°C) and ultrahigh-temperature (1200–1500°C) combustion metamorphism of sediments at the Hatrurim Basin and other localities (Vapnik *et al.*, 2007; Sokol *et al.*, 2008, 2012; 2014*b*; Sharygin *et al.*, 2008*a*,*b*; 2013; Seryotkin *et al.*, 2012). On exposure to air, methane reacted with atmospheric oxygen and ignited. Burning of the high-calorific fossil fuel released enough heat to maintain combustion metamorphism alteration and local melting of marly sediments. Burned carbonate rocks transformed into diverse calcium-rich metamorphic rocks with a typical clinker mineralogy (Sharygin *et al.*, 2008*a*), whereas marly sediments were melted at the same temperature, forming clinopyroxene-bearing paralavas (Vapnik *et al.*, 2007).

Regardless of different opinions their on genesis, all metamorphic rocks of the Hatrurim Basin and other MZ localities are considered to be the products of the high-temperature (900–1200°C) solid-state reactions during organic matter combustion, sometimes with further local melting events (1250–1500°C) (Bentor *et al.*, 1963; Kolodny, 1979; Matthews and Gross, 1980; Sokol *et al.*, 2005; 2007, 2008; 2010; 2014*b*; Zateeva *et al.*, 2007; Vapnik *et al.*, 2006; 2007; Sharygin *et al.*, 2008*a*,*b*; 2013; Geller *et al.*, 2012, Wang *et al.*, 2013; Kokh *et al.*, 2014; Galuskin *et al.*, 2015*c*; Galuskina *et al.*, 2017*a*,*b*).

## Analytical methods

Double-polished rock sections (~50 μm thick) were used for optical examination of a plagioclase-clinopyroxene rock in transmitted and reflected light. The identification of minerals was based on energy-dispersive spectra (EDS), back-scattered electron (BSE) images and elemental mapping (EDS system), using a JEOL 6380LA and TESCAN MIRA 3MLU scanning electron microscopes equipped with an INCA Energy 450 XMax 80 microanalysis system (Oxford Instruments Ltd.) at the V.S. Sobolev Institute of Geology and Mineralogy (IGM), Novosibirsk, Russia. The instruments were operated at an accelerating voltage of 20 kV and a probe current of 1 nA in low-vacuum (40–60 Pa) or high-vacuum modes. Energy-dispersive analysis was performed using a TESCAN MIRA 3MLU scanning electron microscope at an accelerating voltage of 20 kV, a probe current of 1 nA, and accumulation time of 20 s. The following simple compounds and metals were used as reference standards for most of the elements: $SiO_2$ (Si and O); $Al_2O_3$ (Al); diopside (Mg and Ca); albite (Na); orthoclase (K); $Ca_2P_2O_7$ (P); $BaF_2$ (Ba and F); $Cr_2O_3$ (Cr); pyrite (S); $CsRe_2Cl_6$ (Cl); $LaPO_4$ (La); $CePO_4$ (Ce); $SrF_2$ (Sr); metallic Ti, Fe, Mn, Zn, Ni, V and Y. Correction for matrix effects was done using the XPP algorithm, implemented in the software of the microanalysis system. Metallic Co served for quantitative optimization (normalization to probe current and energy calibration of the spectrometer).

Electron microprobe analyses (EMPA) in wavelength-dispersive (WDS) mode were performed for rock-forming and opaque minerals of the Hatrurim rock using a Camebax microprobe at IGM. The operating conditions were as follows: beam diameter of 1–2 μm, accelerating voltage of 20 kV, beam current of 20 nA (silicates) and 50–60 nA (opaque minerals), and counting time of 10 s (5 + 5). The following standards were used for opaque minerals: hematite (Fe); spessartine (Mn); diopside (Ca and Si); albite (Na); $MgAl_2O_4$ (Mg and Al); $ZnFe_2O_4$ (Zn); $NiFe_2O_4$ (Ni); ilmenite (Ti); $V_2O_5$ (V) and others. Correction for matrix effects was done using a PAP routine (Pouchou and Pichoir, 1985). The precision of analysis for major elements was better than 2% relative. The detection limits for elements are (in ppm): Si 210; Ti 162; Cr 248; V 170; Al 142; Fe 157; Mn 135; Mg 162; Ca 110; Sr 202; Ce 245; Na 310; Ni 208; Zn 293; and Cu 210.

Raman spectroscopy was used to identify some of the minerals in the Hatrurim plagioclase-clinopyroxene rock. We used a

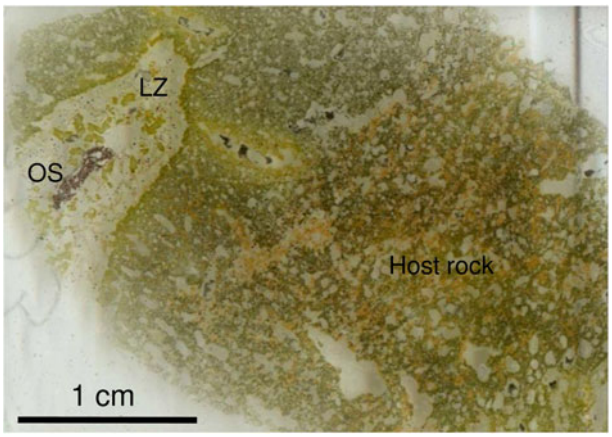


**Fig. 1.** General view of plagioclase-clinopyroxene rock with opaque mineral segregation with corundum (OS) and surrounding leucocratic zone (LZ), Hatrurim Basin, ordinary light. Host rock is intermediate between hornfels and paralava.

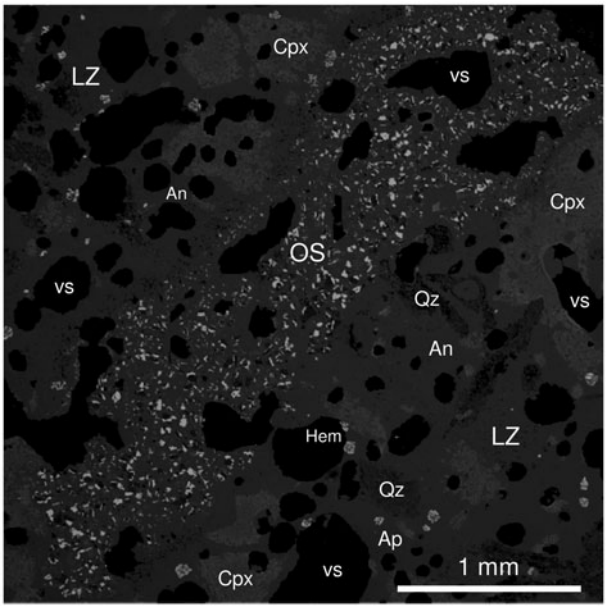


**Fig. 2.** Corundum-bearing opaque mineral segregation (OS) surrounded by leucocratic zone (LZ), plagioclase-clinopyroxene rock, Hatrurim Basin, BSE image. Symbols: An – fine-grained anorthite; Cpx – clinopyroxene; Qz – $SiO_2$ polymorph (quartz-tridymite), Hem – hematite, Ap – fluorapatite, vs – vesicle.

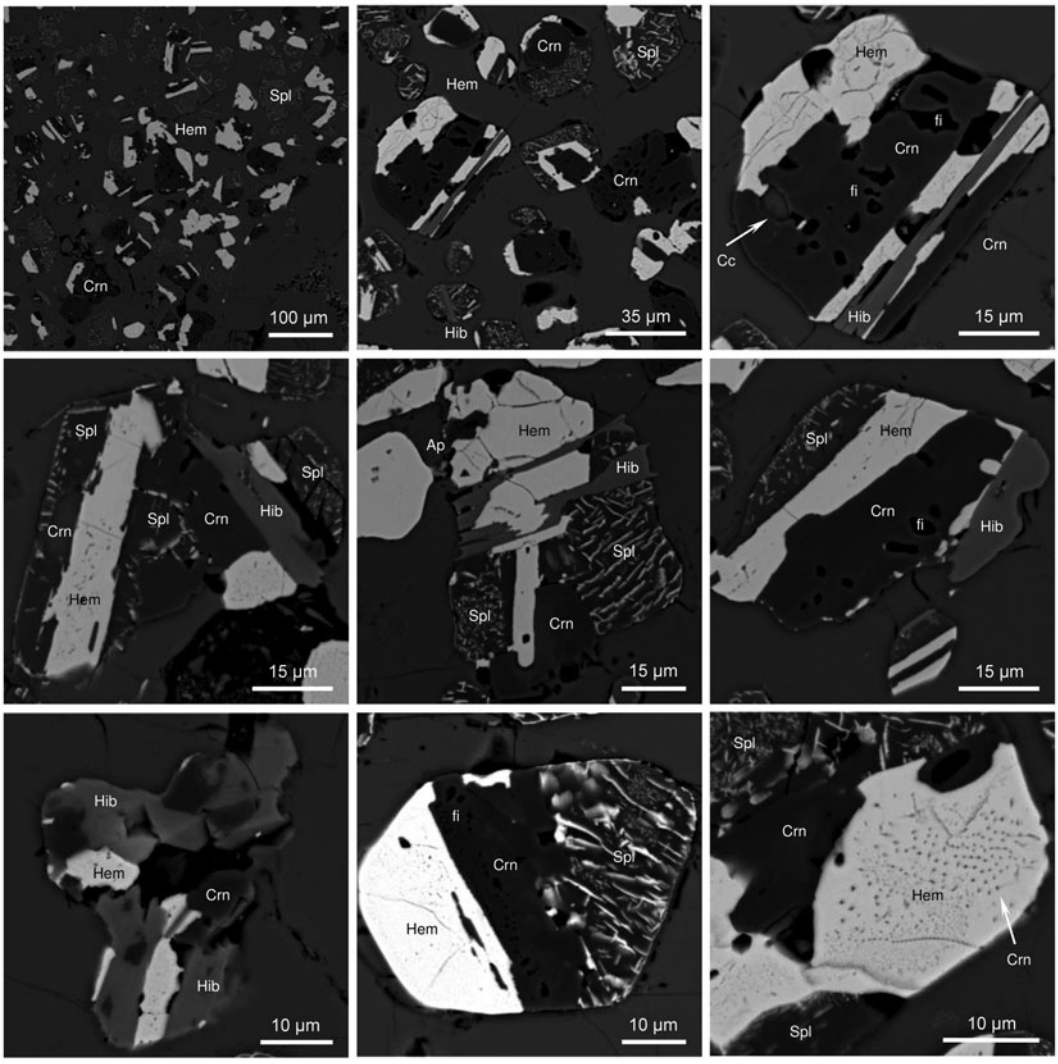


**Fig. 3.** Mineral intergrowths in coarse-grained anorthite from the opaque segregation, plagioclase-clinopyroxene rock, Hatrurim Basin, BSE images. Symbols: Hem – hematite; Spl – spinel; Crn – corundum; Hib – hibonite; Cc – calcite; Ap – fluorapatite; and fi – fluid inclusions in corundum.

LabRAM HR 800 mm (HORIBA Scientific Ltd.) spectrometer equipped with a CCD detector and coupled to an Olympus BX40 confocal microscope (×100 objective). A semiconductor laser emitting at 514.5 nm with a nominal power output of 50 mW was used for excitation. In each case, 20 spectra were recorded for 20 s each at a hole diameter of 100 μm and integrated. The spectra were recorded between 100 and 1200 $cm^{-1}$, and the monochromator was calibrated using the 520.7 $cm^{-1}$ Raman line of elemental Si.

## Mineralogy and petrography of plagioclase-clinopyroxene rock

A plagioclase-clinopyroxene rock sample (5203) was collected from the 'olive unit' on the top of a hill from the central part of the Hatrurim Basin (Fig. S1 C). A brief description of the rock was given in Sokol *et al.* (2005) and Sharygin *et al.* (2008*b*). The specific feature of this rock is the abundance of gas vesicles (100–300 μm) and the presence of lenticular segregation with Fe–Al–Mg-oxide minerals (up to 1 cm) with a leucocratic outer zone (Figs 1, 2). In general, the host rock is equigranular and vesicular and composed mainly of plagioclase ($An_{99}$) and zoned clinopyroxene (size of grains ≈ 30–50 μm) (Fig. 1). On the background of the plagioclase-clinopyroxene aggregate large crystals (300–600 μm) of a $SiO_2$ polymorph (quartz and/or tridymite) are shown clearly (Fig. 1, Fig S2). Elongated $SiO_2$ crystals and anhedral fluorapatite are riddled with inclusions of plagioclase and sometimes clinopyroxene (up to 10 μm). K-feldspar, fluorapatite, hematite, titanite, 'hyalophane' ($Cn_{51-69}$), Ti-andradite, celestine, baryte, calcite, anhydrite and an unidentified Mn-hydroxide occur as minor and accessory minerals in the rock (Fig. S2–S3). The opaque mineral assemblage is hematite ± titanite, these grains also contain numerous inclusions of plagioclase. Mineral relations are shown in Fig. S2–S3 and compositions of minerals of the host rock are given in Tables S1, S3 (Supplementary material). The vesicles in the host rock, opaque segregation and leucocratic zone are partly or completely filled with low-temperature calcite, zeolite-supergroup minerals, quartz and rare bassanite (or anhydrite) (Fig. S2–S3, Table S2). Some minerals (clinopyroxene, Ti-andradite, fluorapatite, K-feldspar) occasionally form well-faceted crystals in the vesicles. Previously we classified this

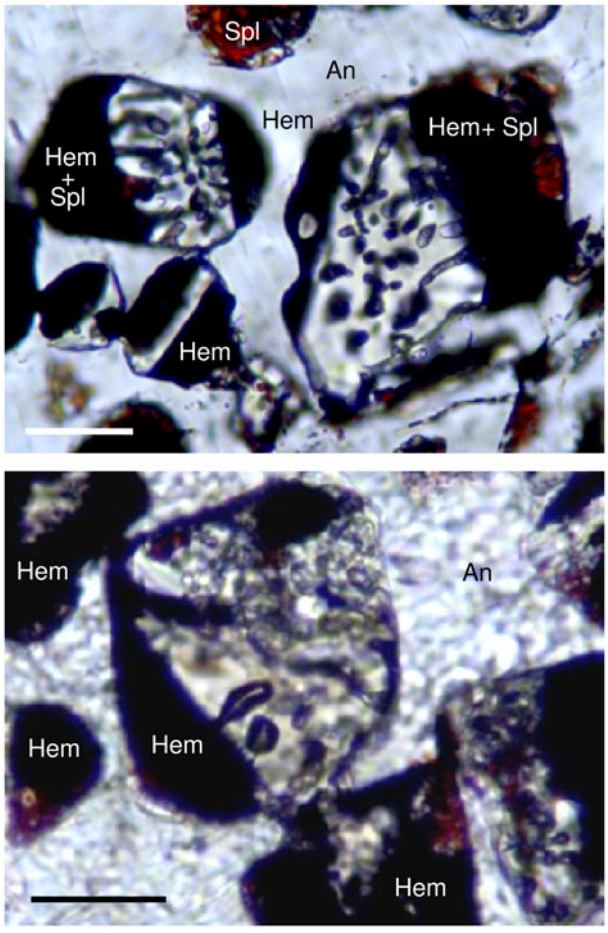


**Fig. 4.** Fluid and crystal inclusions in corundum from opaque mineral segregation, Hatrurim Basin, transmitted light. Spl – spinel; Hem – hematite; An – anorthite. Scale bar is 25 μm.

rock as plagioclase-clinopyroxene hornfels (Sharygin *et al.*, 2008*b*). However, the abundance of vesicles allows it to be interpreted as paralava, which was formed after hornfels.

The segregation with opaque phases (up to 1 cm, Fig. 2) contains intergrowths of Fe–Al–Mg-oxide phases (corundum, hematite, spinel, hibonite) in coarse-grained plagioclase (up to 1 mm). Clinopyroxene, fluorapatite and K-feldspar are minor-to-accessory and localised mainly in the interstices between plagioclase crystals. Individual Fe–Al–Mg-oxide intergrowths are up to 70 μm and the ratio of minerals in them is variable (Fig. 3). Fluid and crystal inclusions are common in corundum (Fig. 4); the latter are represented by plagioclase and rarely by hematite and calcite. The majority of spinels contain oriented exsolution structures of hematite (supported by Raman spectra), whereas homogenous grains are rare. Hematite is also inhomogeneous and encloses oriented μm-sized exsolved corundum and rare inclusions of unidentified Ti–Fe- and Ca–V–Fe-oxide phases (Fig. 3; Fig. S5).

The outer leucocratic zone is represented by fine-grained feldspathic aggregate (10–30 μm, plagioclase ± K-feldspar) with coarse grains (up to 1 mm) of clinopyroxene, $SiO_2$ polymorph and fluorapatite, which are riddled with plagioclase inclusions (Fig. 2, Fig. S3). The opaque minerals (hematite ± 'hemoilmenite' $(Fe^{2+},Fe^{3+})(Ti,Fe^{3+})O_3$ ± titanite ± perovskite) are also abundant (Fig. 2, Figs S3–S4). The association of Cr-rich hematite and spinel occurs scarcely, mainly near the opaque segregation (Fig. S4).

The compositions of silicates and phosphates from the host rock, opaque segregation and leucocratic zone are rather similar: plagioclase is anorthite ($An_{99}$); clinopyroxene is diopside-dominant ($Di_{30-55}Ess_{21-39}Hd_{10-27}Ts_{4-20}Acm_{1-2}$); K-feldspar has a moderate content of BaO (up to 2.5 wt.%); fluorapatite is enriched in $SiO_2$ (2.6–6.9 wt.%) and $SO_3$ (0.0–1.7 wt.%), sometimes in $V_2O_3$ (up to 2.3 wt.%) and oxides of light-rare-earth elements ($LREE_2O_3$ up to 0.5 wt.%), showing evolution to fluorellestadite. Clinopyroxene from the host rock is zoned, and the core-to-rim variation is directed towards the enrichment in the $Fe^{2+}$- and $Fe^{3+}$-rich end-members (hedenbergite and esseneite, respectively). Clinopyroxene in the leucocratic zone and segregation with opaque phases is yellowish indicating higher contents of esseneite. The composition of the above silicates and Fe-rich oxides is given in Tables S1–S4.

Note that a single opaque segregation with corundum has been observed in this investigation. Other rare opaque assemblages in vesicles or nearby in this rock reveals diverse mineral compositions: intergrowths of spinel, hematite, hibonite, orthorhombic $FeAlO_3$ and a dorrite-like phase (Sharygin and Sokol, 2017); hematite + Al-rich magnetite + dorrite-like phase + esseneite ± hibonite ± melilite/andradite or hematite + spinel ± ilmenite (author's unpublished data). Corundum is absent in these assemblages.

## Composition of oxide minerals in the corundum-bearing opaque segregation

Fe–Al–Mg-oxide phases in the opaque segregation are distinguished easily in transmitted and reflected polarised light. Corundum is colourless and contains abundant fluid inclusions; hematite is translucent and red; spinel is light brown and with abundant exsolution hematite; and hibonite is yellow to yellow-brown. The mineral relationships do not allow a clear crystallization sequence to be established, but, in general, corundum is an earlier phase than hibonite (Fig. 3, Fig. S5). All oxide phases seem to be formed before, or simultaneously with anorthite. The assemblage has particular mineral compositions, which are common to pyrometamorphic and combustion metamorphism phases (Reverdatto, 1970; Sokol *et al.*, 2005; Grapes, 2011).

### *Hibonite*

This mineral is a minor component within the intergrowths (Fig. 3). Most hibonites are Ti-rich ($TiO_2 > 8$ wt.%) with average composition $Ca_{0.95}(Al_{9.13}Fe^{3+}_{1.25}Ti_{0.77}Mg_{0.64}Fe^{2+}_{0.22}Si_{0.04})O_{19}$ (Table 1), expressed in simplified formula as $CaAl_9Fe^{3+}(Mg,Fe^{2+})TiO_{19}$. It is obviously not similar to 'ideal' hibonite $CaAl_{12}O_{19}$. Compositional variations of the Hatrurim hibonite are given in Fig. 5. The weak negative correlations are indicated between Al and Si, Ti and $Fe^{3+}$. In general, terrestrial and extraterrestrial hibonites (Agrell *et al.*, 1999; Simon *et al.*, 2001; Simon and Grossman, 2003; Ulianov *et al.*, 2005; Nagashima *et al.*, 2010; Rajesh *et al.*, 2010; Sharygin, 2010; Ananyev *et al.*, 2011; Doyle *et al.*, 2014; and references therein) show moderate-to-high concentrations of Ti and highlight that classification of the magnetoplumbite group needs revision, especially for Ca–Al-compositions.

### *Spinel*

According to the classification diagram (Fig. 6) all the minerals analysed in this group are spinel. However, individual grains or areas within the grains (homogeneous and with exsolution) differ

**Table 1.** Representative compositions of hibonite from opaque corundum-bearing segregation in plagioclase-clinopyroxene rock, Hatrurim Basin, Israel.

| Sample | Hib-1 | Hib-2 | Hib-3 | Hib-4 | Hib-5 | Hib-6 | Hib-7 | Hib-8 | Hib-9 |
|---|---|---|---|---|---|---|---|---|---|
| *n* | 9 | 5 | 3 | 4 | 3 | 3 | 3 | 3 | 3 |
| wt.% | | | | | | | | | |
| $SiO_2$ | 0.32 | 0.40 | 0.36 | 0.35 | 0.36 | 0.41 | 0.30 | 0.41 | 0.37 |
| $TiO_2$ | 8.26 | 9.12 | 8.56 | 8.55 | 7.81 | 8.25 | 8.27 | 8.91 | 8.49 |
| $Cr_2O_3$ | 0.11 | 0.65 | n.a. | n.a. | n.a. | n.a. | n.a. | n.a. | n.a. |
| $V_2O_3$ | 0.31 | 0.16 | n.a. | n.a. | n.a. | n.a. | n.a. | n.a. | n.a. |
| $Al_2O_3$ | 64.32 | 62.56 | 63.41 | 65.34 | 63.37 | 65.56 | 65.55 | 64.15 | 64.23 |
| $Fe_2O_3$* | 13.97 | 13.66 | 14.35 | 12.82 | 16.24 | 12.77 | 13.59 | 13.40 | 13.75 |
| FeO* | 1.92 | 2.35 | 3.02 | 2.15 | 1.99 | 2.36 | 1.85 | 2.06 | 1.82 |
| MnO | 0.08 | 0.13 | n.a. | n.a. | n.a. | n.a. | n.a. | n.a. | n.a. |
| MgO | 3.52 | 3.66 | 3.43 | 3.69 | 3.40 | 3.58 | 3.61 | 3.85 | 3.56 |
| CaO | 7.06 | 7.10 | 6.81 | 7.19 | 7.13 | 7.01 | 7.27 | 7.29 | 7.53 |
| SrO | 0.04 | 0.04 | 0.02 | 0.04 | 0.05 | 0.05 | 0.01 | 0.08 | 0.07 |
| $Ce_2O_3$ | 0.04 | 0.05 | 0.04 | 0.05 | 0.05 | 0.05 | 0.05 | 0.06 | 0.05 |
| $Na_2O$ | 0.08 | 0.09 | 0.06 | 0.06 | 0.06 | 0.05 | 0.09 | 0.06 | 0.06 |
| NiO | 0.10 | 0.07 | n.a. | n.a. | n.a. | n.a. | n.a. | n.a. | n.a. |
| ZnO | 0.13 | 0.16 | n.a. | n.a. | n.a. | n.a. | n.a. | n.a. | n.a. |
| CuO | 0.00 | 0.03 | n.a. | n.a. | n.a. | n.a. | n.a. | n.a. | n.a. |
| Sum | 100.28 | 100.22 | 100.07 | 100.23 | 100.47 | 100.10 | 100.59 | 100.27 | 99.92 |
| Formula on the basis of 13 cations and 19 oxygens | | | | | | | | | |
| Si | 0.04 | 0.05 | 0.04 | 0.04 | 0.04 | 0.05 | 0.04 | 0.05 | 0.05 |
| Ti | 0.75 | 0.83 | 0.78 | 0.77 | 0.71 | 0.74 | 0.74 | 0.80 | 0.77 |
| Cr + V | 0.04 | 0.08 | | | | | | | |
| Al | 9.12 | 8.92 | 9.04 | 9.22 | 9.02 | 9.26 | 9.22 | 9.08 | 9.12 |
| $Fe^{3+}$ | 1.26 | 1.24 | 1.31 | 1.15 | 1.48 | 1.15 | 1.22 | 1.21 | 1.25 |
| $Fe^{2+}$ | 0.19 | 0.24 | 0.31 | 0.22 | 0.20 | 0.24 | 0.18 | 0.21 | 0.18 |
| Mn | 0.01 | 0.01 | | | | | | | |
| Mg | 0.63 | 0.66 | 0.62 | 0.66 | 0.61 | 0.64 | 0.64 | 0.69 | 0.64 |
| Ca | 0.91 | 0.92 | 0.88 | 0.92 | 0.92 | 0.90 | 0.93 | 0.94 | 0.97 |
| Sr + Ce | 0.01 | 0.01 | 0.01 | 0.01 | 0.01 | 0.01 | 0.01 | 0.01 | 0.01 |
| Na | 0.02 | 0.02 | 0.01 | 0.01 | 0.01 | 0.01 | 0.02 | 0.01 | 0.01 |
| Ni + Zn + Cu | 0.02 | 0.02 | | | | | | | |

*n* = number of analyses (WDS); $La_2O_3$, $Y_2O_3$, $K_2O$ and $ZrO_2$ are below detection limits (<<0.01 wt.%); n.a. = not analysed.
*$Fe_2O_3$ and FeO are calculated from charge balance.

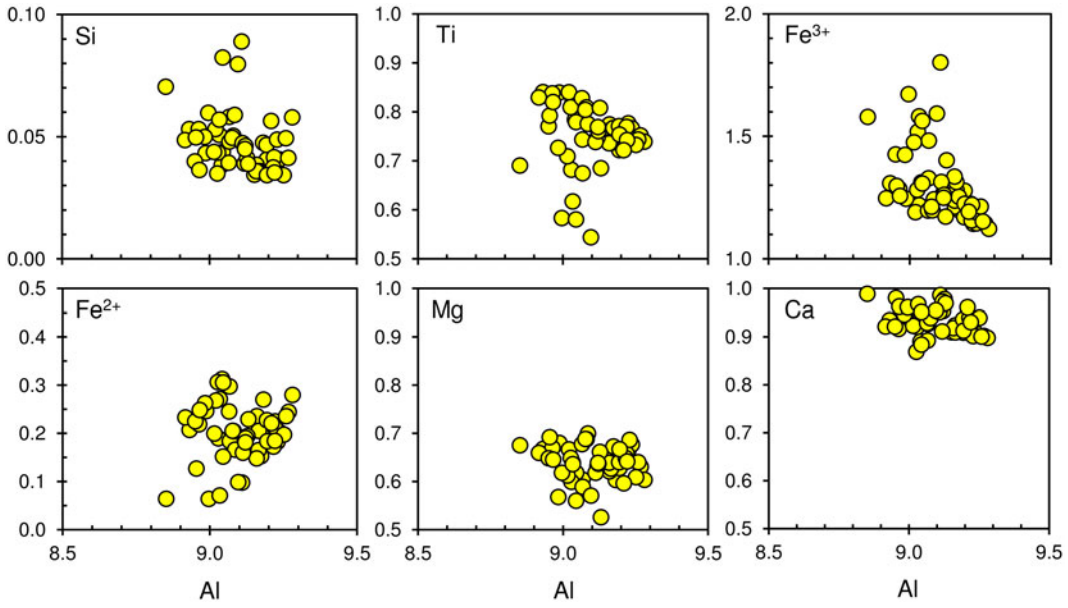


**Fig. 5.** Variations of Al *vs.* major elements (in atoms per formula unit) for hibonite from opaque segregation in plagioclase-clinopyroxene rock, Hatrurim Basin, Israel.

in composition. Dominant spinel (with exsolution) has the average formula $(Mg_{0.75}Fe^{2+}_{0.20}Ni_{0.03}Zn_{0.01}Mn_{0.01})(Al_{1.79}Fe^{3+}_{0.20}Cr_{0.01})O_4$ ($n = 40$), whereas homogeneous species have $(Mg_{0.77}Fe^{2+}_{0.17}Ni_{0.03}Zn_{0.02}Mn_{0.01})(Al_{1.94}Fe^{3+}_{0.05}Cr_{0.01})O_4$ ($n = 24$). This indicates evolution towards the magnesioferrite and magnetite end-members. Representative compositions of the Hatrurim spinel

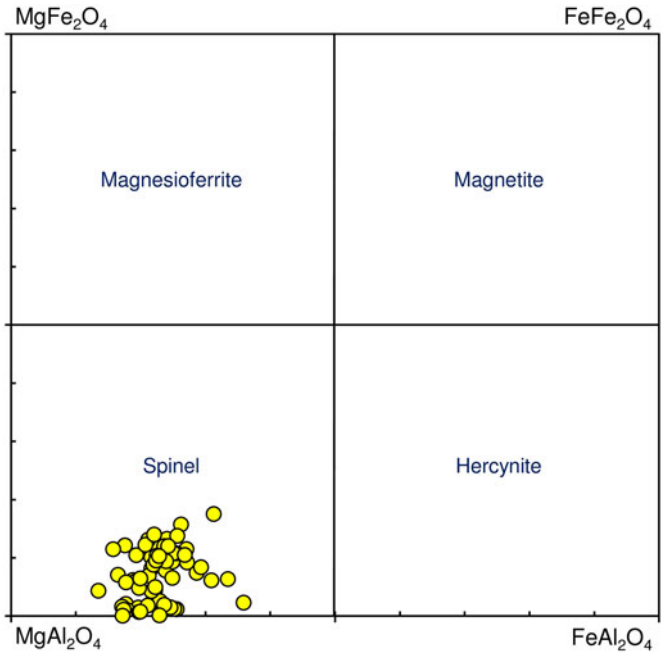


**Fig. 6.** Classification diagram for spinel from opaque segregation in plagioclase-clinopyroxene rock, Hatrurim Basin, Israel.

are given in Table 2. In general, both types of spinel are rich in NiO (up to 1.9 wt.) and ZnO (up to 1.4 wt.%); the content of other minor oxides is negligible (<0.15 wt.%). Thus, solid phase decay of an initial Fe-rich spinel with formation of hematite might be explained by the reaction of partial oxidation: $2(Mg_{0.5}Fe^{2+}_{0.5})(Al_{1.0}Fe^{3+}_{1.0})O_4 + 0.25O_2 \rightarrow MgAl_2O_4 + 1.5Fe_2O_3$.

### *Corundum and hematite*

Corundum and hematite are the main constituents of most opaque intergrowths (Fig. 3). Corundum essentially varies in $Fe_2O_3$ (4.2–11.8 wt.%); minor components are $Cr_2O_3$ (up to 0.6 wt.%) and $TiO_2$ (up to 0.4 wt.%). The content of other minor oxides is negligible (<0.1 wt.%). Variations in $Fe_2O_3$ content for the Hatrurim corundum are given in Fig. 7. In general, some corundum grains show mosaic (spotty) zonation, especially in direct contact with hematite (Fig. 3, Fig. S5). The compositions richer in Fe are common near the corundum-hematite boundary. Solid inclusions in corundum are represented by anorthite, hematite and calcite. No oriented exsolution structure is found in this mineral.

As noted above, orthorhombic $FeAlO_3$ was identified in one of the opaque assemblages in vesicles in the rock investigated (Sharygin and Sokol, 2017). Therefore hematite from the corundum-bearing segregation was investigated for other polymorphic modifications of $Fe_2O_3$ using Raman spectroscopy, Fig. S6. Five crystalline polymorphs of $Fe_2O_3$ are known: hematite ($\alpha$-$Fe_2O_3$, trigonal); maghemite ($\gamma$-$Fe_2O_3$, cubic with tetragonal superstructure); luogufengite ($\varepsilon$-$Fe_2O_3$, orthorhombic) (Sakurai *et al.*, 2009; Xu *et al.*, 2017); $\beta$-$Fe_2O_3$ (synthetic, cubic) (Zboril *et al.*, 1999; Sakurai *et al.*, 2009), and $\xi$-$Fe_2O_3$ (synthetic, monoclinic) (Tucek *et al.*, 2015). In addition, orthorhombic $\varepsilon$-$FeAlO_3$, perovskite and post-perovskite $FeAlO_3$ and $AlFeO_3$ have been synthesised (Polli *et al.*, 1996; Majzlan *et al.*, 2002; Feenstra *et al.*, 2005; Pissas *et al.*, 2008; Caracas, 2010). The hematite studied from the Hatrurim Basin differs drastically from $FeAlO_3$ with lower $Al_2O_3$. Raman spectra indicate a suite of bands characteristic of hematite (Hanesch, 2009; Jubb and Allen, 2010) and it differs significantly from maghemite and, possibly, from other polymorphs (Fig. S6).

**Table 2.** Representative compositions (wt.%) of spinel from opaque segregation in plagioclase-clinopyroxene rock, Hatrurim Basin, Israel.

| Spinel | hom | hom | hom | hom | hom | hom | decay | decay | decay | decay | decay | decay | decay | decay |
|---|---|---|---|---|---|---|---|---|---|---|---|---|---|---|
| *n* | 1 | 1 | 2 | 3 | 3 | 1 | 2 | 1 | 1 | 1 | 1 | 1 | 2 | 3 |
| wt.% | | | | | | | | | | | | | | |
| $TiO_2$ | 0.10 | 0.01 | 0.00 | 0.05 | 0.11 | 0.03 | 0.01 | b.d.l. | 0.03 | 0.01 | 0.02 | 0.11 | 0.06 | 0.02 |
| $Cr_2O_3$ | 0.30 | 0.76 | 0.44 | 0.44 | 0.33 | 0.33 | 0.45 | 0.37 | 0.50 | 0.63 | 0.35 | 0.33 | 0.60 | 0.44 |
| $V_2O_3$ | 0.05 | 0.10 | 0.08 | 0.06 | 0.05 | 0.05 | 0.04 | 0.11 | 0.06 | 0.04 | 0.11 | 0.06 | 0.05 | 0.10 |
| $Al_2O_3$ | 66.26 | 64.76 | 64.24 | 65.57 | 65.05 | 63.50 | 62.76 | 61.41 | 60.12 | 60.38 | 59.31 | 60.79 | 59.14 | 56.62 |
| $Fe_2O_3$* | 2.06 | 2.18 | 4.41 | 1.44 | 2.87 | 4.56 | 6.15 | 7.10 | 8.37 | 8.05 | 9.46 | 6.23 | 8.89 | 11.47 |
| FeO* | 6.75 | 8.05 | 6.47 | 9.27 | 9.08 | 8.45 | 7.27 | 7.85 | 8.12 | 9.28 | 9.57 | 12.99 | 11.22 | 10.44 |
| MnO | 0.21 | 0.25 | 0.32 | 0.41 | 0.24 | 0.33 | 0.22 | 0.29 | 0.34 | 0.31 | 0.28 | 0.20 | 0.22 | 0.23 |
| MgO | 21.72 | 20.22 | 21.48 | 19.25 | 20.36 | 20.09 | 21.09 | 20.28 | 20.05 | 19.43 | 19.22 | 17.28 | 18.32 | 18.27 |
| CaO | 0.05 | 0.11 | 0.09 | 0.11 | 0.06 | 0.05 | 0.10 | 0.09 | 0.04 | 0.04 | 0.11 | 0.08 | 0.08 | 0.05 |
| NiO | 1.51 | 1.81 | 1.75 | 1.84 | 1.45 | 1.67 | 1.47 | 1.72 | 1.60 | 1.50 | 1.59 | 1.53 | 1.53 | 1.58 |
| ZnO | 0.86 | 0.92 | 0.71 | 1.38 | 0.46 | 0.87 | 0.69 | 0.71 | 0.69 | 0.86 | 0.59 | 0.53 | 0.48 | 0.57 |
| CuO | n.a. | n.a. | n.a. | 0.07 | 0.00 | n.a. | 0.03 | n.a. | 0.03 | 0.01 | n.a. | n.a. | n.a. | 0.00 |
| Sum | 99.87 | 99.18 | 99.97 | 99.88 | 100.06 | 99.93 | 100.27 | 99.93 | 99.95 | 100.53 | 100.62 | 100.13 | 100.57 | 99.79 |
| Formula on the basis of 3 cations and 4 oxygens | | | | | | | | | | | | | | |
| Ti | 0.00 | 0.00 | 0.00 | 0.00 | 0.00 | 0.00 | 0.00 | | 0.00 | 0.00 | 0.00 | 0.00 | 0.00 | 0.00 |
| Cr + V | 0.01 | 0.02 | 0.01 | 0.01 | 0.01 | 0.01 | 0.01 | 0.01 | 0.01 | 0.01 | 0.01 | 0.01 | 0.01 | 0.01 |
| Al | 1.95 | 1.94 | 1.90 | 1.96 | 1.93 | 1.90 | 1.87 | 1.85 | 1.83 | 1.83 | 1.81 | 1.87 | 1.81 | 1.76 |
| $Fe^{3+}$ | 0.04 | 0.04 | 0.08 | 0.03 | 0.05 | 0.09 | 0.12 | 0.14 | 0.16 | 0.15 | 0.18 | 0.12 | 0.17 | 0.23 |
| $Fe^{2+}$ | 0.14 | 0.17 | 0.14 | 0.20 | 0.19 | 0.18 | 0.15 | 0.17 | 0.18 | 0.20 | 0.21 | 0.28 | 0.25 | 0.23 |
| Mn | 0.00 | 0.01 | 0.01 | 0.01 | 0.01 | 0.01 | 0.01 | 0.01 | 0.01 | 0.01 | 0.01 | 0.01 | 0.01 | 0.01 |
| Mg | 0.81 | 0.77 | 0.81 | 0.73 | 0.77 | 0.76 | 0.80 | 0.77 | 0.77 | 0.75 | 0.74 | 0.67 | 0.71 | 0.72 |
| Ca | | | | 0.00 | 0.00 | | 0.00 | | 0.00 | 0.00 | | | | 0.00 |
| Ni + Zn + Ni | 0.05 | 0.05 | 0.05 | 0.06 | 0.04 | 0.05 | 0.04 | 0.05 | 0.04 | 0.05 | 0.04 | 0.04 | 0.04 | 0.04 |

*n* = number of analyses (WDS); hom = homogeneous spinel; decay = spinel with solid phase decay structure; n.a. = not analysed; b.d.l = below detection limit.
*$Fe_2O_3$ and FeO are calculated from charge balance.

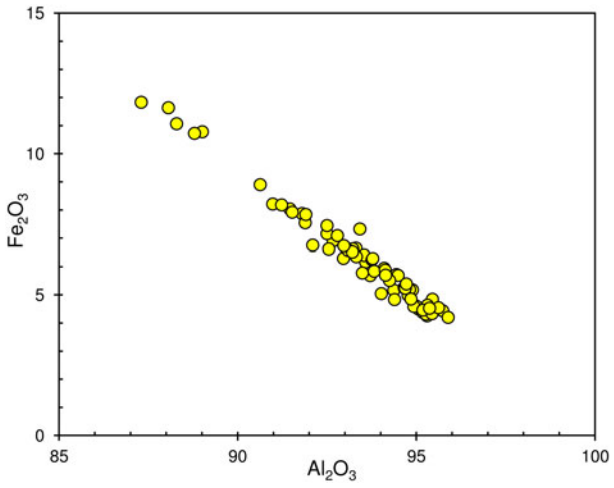


**Fig. 7.** Variations of $Al_2O_3$ *vs.* $Fe_2O_3$ contents (in wt.%) in corundum from opaque segregation in plagioclase-clinopyroxene rock, Hatrurim Basin, Israel.

Hematite also varies notably in composition (in wt.%): $TiO_2$ 0.7–5.6; $Al_2O_3$ 0.7–8.6; $Cr_2O_3$ 0.2–1.5; $V_2O_3$ 0.1–1.0; MgO 0.3–2.0; and up to 0.4 MnO, NiO and CaO. Compositional variations of hematite from the opaque segregation in comparison with those from the leucocratic zone and host rock are shown in Fig. 8. In general, hematite from the opaque segregation is richer in $Al_2O_3$, $Cr_2O_3$, $V_2O_3$ and MgO and poorer in $TiO_2$ and FeO than the same mineral from other associations (Fig. 8). In addition to these peculiarities, hematite from the opaque segregation is inhomogeneous and sporadically contains oriented exsolution structures of corundum (Fig. 3, Fig. S5). Rare μm-sized inclusions of unidentified Ti–Fe- and Ca–V–Fe-oxide phases were also found in this hematite (Fig. S5). Within intergrowths the Ti–Fe phase (ilmenite ?) occurs both in hematite and at the boundary with other oxide minerals. The average EDS compositions for Ca–V–Fe oxide is (in wt.%, excitation of host hematite is possible): $TiO_2$ 3.19; $Cr_2O_3$ 0.14; $V_2O_3$ 20.39; $Al_2O_3$ 4.45; $Fe_2O_3$ 47.58; and MgO 0.61.

The compositions of the coexisting corundum and hematite within intergrowths for Hatrurim are given in Table 3 (WDS spot analyses, 1–2 μm) and Table S5 (EDS rastered analyses, >3 μm ×3 μm).

## Discussion

### *Anorthite-clinopyroxene rock: hornfels or paralava?*

As noted above the plagioclase-clinopyroxene rock investigated might be interpreted as paralava (the product of a local melting event), which formed after hornfels. This conclusion is supported by petrographic observations, in particular, by the high abundance of vesicles, which are now partly or completely filled with secondary minerals, such as calcite, zeolite-supergroup minerals, quartz and Ca-sulfates (Fig. S2–S3, Table S2). The classic term 'hornfels' refers to a dense fine-grained metamorphic rock, the product of solid-state transformations. The appearance of vesicles in the sample investigated is evidence of at least partial (or precursor) melting of parent plagioclase-clinopyroxene hornfels possibly near 1240°C (temperature of the anorthite–diopside eutectic) by the influence of superheated oxidised gases. An investigation of different plagioclase-clinopyroxene paralavas in the 'olive' unit at Hatrurim Basin indicated minimal melting temperatures as high as 1100°C (Vapnik *et al.*, 2007), whereas the formation of the same hornfels (solid phase transformation) remains enigmatic in the temperature context. Such a two-stage model of sedimentary transformation (initial marly sediment → hornfel/clinker → paralava) was suggested for some Hatrurim plagioclase-clinopyroxene and melilite-rich paralavas (Sharygin *et al.*, 2006; Vapnik *et al.*, 2007; Sokol *et al.*, 2008; 2010; 2012; 2015;

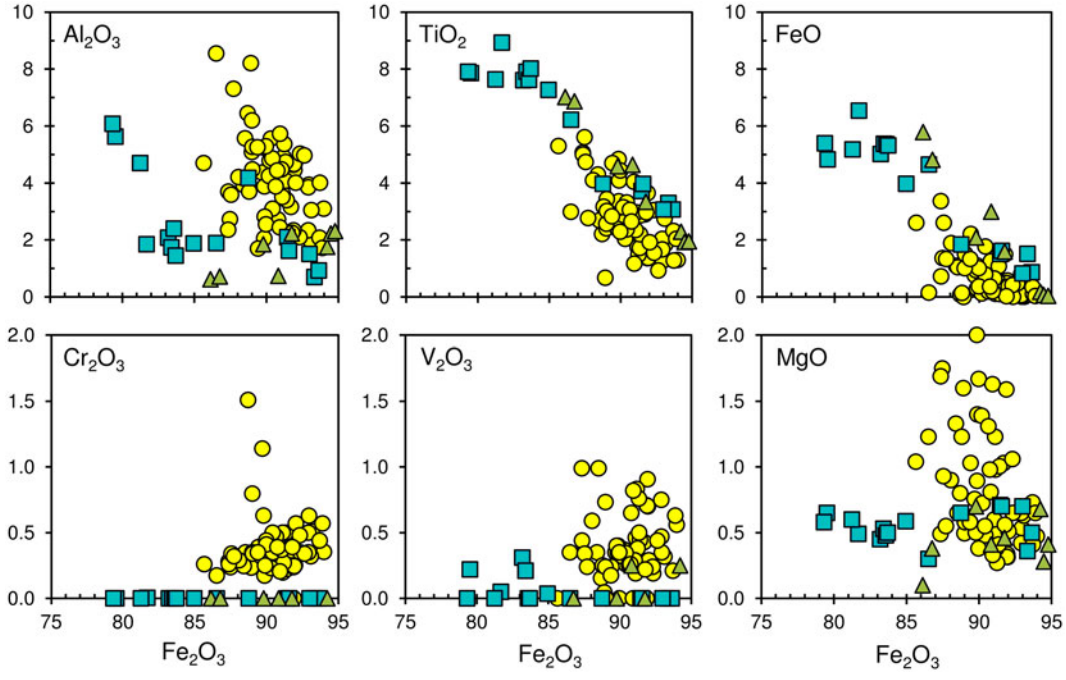


**Fig. 8.** Variations of $Fe_2O_3$ *vs.* major oxides (in wt.%) for hematite from the opaque segregation (circles), leucocratic zone (squares) and host plagioclase-clinopyroxene rock (triangles), Hatrurim Basin, Israel.

**Table 3.** Representative composition (WDS, wt.%) of coexisting corundum (Crn) and hematite (Hem) from opaque segregation in plagioclase-clinopyroxene rock, Hatrurim Basin, Israel.

| | 1 | | 2 | | 3 | | 4 | | 5 | | 6 | | 7 | |
|---|---|---|---|---|---|---|---|---|---|---|---|---|---|---|
| Mineral | Crn | Hem | Crn | Hem | Crn | Hem | Crn | Hem | Crn | Hem | Crn | Hem | Crn | Hem |
| $TiO_2$ | 0.07 | 2.41 | 0.05 | 1.75 | 0.06 | 1.85 | 0.06 | 1.47 | 0.05 | 2.21 | 0.12 | 0.98 | 0.08 | 2.99 |
| $Cr_2O_3$ | 0.30 | 0.80 | 0.16 | 0.27 | 0.23 | 0.51 | 0.14 | 0.33 | 0.54 | 1.51 | 0.18 | 0.44 | 0.06 | 0.17 |
| $V_2O_3$ | 0.05 | 0.73 | 0.06 | 0.83 | 0.09 | 0.32 | 0.07 | 0.91 | 0.02 | 0.15 | 0.07 | 0.59 | n.a. | n.a. |
| $Al_2O_3$ | 95.30 | 5.09 | 94.97 | 4.91 | 95.00 | 3.05 | 94.97 | 4.46 | 94.39 | 6.45 | 93.66 | 9.08 | 93.58 | 8.55 |
| $Fe_2O_3$* | 4.26 | 89.33 | 4.31 | 91.18 | 4.60 | 93.35 | 4.72 | 91.83 | 4.83 | 88.46 | 5.80 | 87.90 | 6.17 | 86.51 |
| FeO* | 0.00 | 1.09 | 0.00 | 0.59 | 0.00 | 0.00 | 0.00 | 0.58 | 0.00 | 0.00 | 0.00 | 0.00 | 0.00 | 0.15 |
| MnO | 0.06 | b.d.l. | 0.07 | b.d.l. | 0.07 | 0.10 | 0.03 | b.d.l. | 0.05 | 0.17 | 0.04 | 0.10 | b.d.l. | 0.10 |
| MgO | 0.05 | 0.50 | 0.05 | 0.38 | 0.05 | 0.83 | 0.04 | 0.34 | 0.05 | 0.85 | 0.05 | 0.88 | 0.07 | 1.23 |
| CaO | 0.04 | 0.12 | 0.05 | 0.20 | 0.03 | 0.17 | 0.04 | 0.11 | 0.04 | 0.24 | 0.04 | 0.37 | 0.07 | 0.19 |
| NiO | 0.02 | 0.05 | 0.02 | 0.05 | 0.02 | 0.12 | n.a. | n.a. | n.a. | n.a. | n.a. | n.a. | n.a. | n.a. |
| ZnO | b.d.l. | b.d.l. | 0.03 | b.d.l. | 0.02 | b.d.l. | b.d.l. | b.d.l. | 0.01 | b.d.l. | 0.01 | 0.01 | n.a. | n.a. |
| Sum | 100.14 | 100.11 | 99.76 | 100.17 | 100.18 | 100.30 | 100.07 | 100.03 | 99.99 | 100.04 | 99.95 | 100.33 | 100.03 | 99.90 |
| Formula on the basis of 2 cations and 3 oxygens | | | | | | | | | | | | | | |
| Ti | 0.00 | 0.05 | 0.00 | 0.03 | 0.00 | 0.04 | 0.00 | 0.03 | 0.00 | 0.04 | 0.00 | 0.02 | 0.00 | 0.06 |
| Cr + V | 0.01 | 0.02 | 0.00 | 0.02 | 0.00 | 0.02 | 0.00 | 0.03 | 0.01 | 0.03 | 0.00 | 0.02 | 0.00 | 0.00 |
| Al | 1.93 | 0.16 | 1.94 | 0.15 | 1.94 | 0.09 | 1.94 | 0.14 | 1.93 | 0.19 | 1.92 | 0.26 | 1.92 | 0.25 |
| $Fe^{3+}$ | 0.06 | 1.72 | 0.06 | 1.76 | 0.06 | 1.81 | 0.06 | 1.78 | 0.06 | 1.70 | 0.08 | 1.66 | 0.08 | 1.63 |
| $Fe^{2+}$ | 0.00 | 0.02 | 0.00 | 0.01 | 0.00 | 0.00 | 0.00 | 0.01 | 0.00 | 0.00 | 0.00 | 0.00 | 0.00 | 0.00 |
| Mn | 0.00 | 0.00 | 0.00 | | 0.00 | 0.00 | 0.00 | | 0.00 | 0.00 | 0.00 | 0.00 | | 0.00 |
| Mg | 0.00 | 0.02 | 0.00 | 0.02 | 0.00 | 0.03 | 0.00 | 0.01 | 0.00 | 0.03 | 0.00 | 0.03 | 0.00 | 0.05 |
| Ca + Ni + Zn | 0.00 | 0.01 | 0.00 | 0.01 | 0.00 | 0.01 | 0.00 | 0.00 | 0.00 | 0.01 | 0.00 | 0.01 | 0.00 | 0.01 |
| $X_{Al_2O_3}$ | 0.97 | 0.10 | 0.97 | 0.09 | 0.97 | 0.06 | 0.97 | 0.08 | 0.97 | 0.12 | 0.96 | 0.15 | 0.96 | 0.14 |
| $X_{Fe_2O_3}$ | 0.03 | 0.90 | 0.03 | 0.91 | 0.03 | 0.94 | 0.03 | 0.92 | 0.03 | 0.88 | 0.04 | 0.85 | 0.04 | 0.86 |

| | 8 | | 9 | | 10 | | 11 | | 12 | | 13 | | 14 | |
|---|---|---|---|---|---|---|---|---|---|---|---|---|---|---|
| Mineral | Crn | Hem | Crn | Hem | Crn | Hem | Crn | Hem | Crn | Hem | Crn | Hem | Crn | Hem |
| $TiO_2$ | 0.12 | 2.19 | 0.16 | 2.64 | 0.19 | 2.64 | 0.13 | 5.61 | 0.22 | 2.43 | 0.08 | 1.36 | 0.39 | 3.36 |
| $Cr_2O_3$ | 0.15 | 0.37 | 0.19 | 1.14 | 0.15 | 0.38 | 0.25 | 0.24 | 0.32 | 0.28 | 0.32 | 0.24 | 0.33 | 0.33 |
| $V_2O_3$ | 0.08 | 0.53 | n.a. | n.a. | n.a. | n.a. | n.a. | n.a. | 0.03 | 0.37 | 0.19 | 0.71 | n.a. | n.a. |
| $Al_2O_3$ | 93.10 | 3.93 | 92.37 | 4.37 | 92.50 | 4.79 | 91.80 | 2.73 | 89.01 | 3.05 | 87.96 | 4.64 | 87.30 | 3.88 |
| $Fe_2O_3$* | 6.50 | 91.52 | 6.91 | 90.25 | 7.16 | 90.23 | 7.87 | 87.80 | 10.45 | 92.51 | 11.52 | 91.98 | 11.83 | 90.08 |
| FeO* | 0.00 | 0.08 | 0.03 | 0.76 | 0.01 | 0.74 | 0.03 | 1.36 | 0.00 | 0.00 | 0.00 | 0.48 | 0.08 | 1.10 |
| MnO | 0.04 | 0.02 | 0.00 | 0.03 | b.d.l. | 0.01 | b.d.l. | 0.09 | 0.04 | 0.11 | 0.06 | b.d.l. | b.d.l. | 0.05 |
| MgO | 0.04 | 0.74 | 0.05 | 0.76 | 0.06 | 0.72 | 0.05 | 1.75 | 0.09 | 1.48 | 0.05 | 0.32 | 0.08 | 0.89 |
| CaO | 0.03 | 0.42 | 0.02 | 0.18 | 0.04 | 0.26 | b.d.l. | 0.37 | 0.07 | 0.33 | 0.08 | 0.10 | 0.10 | 0.22 |
| NiO | n.a. | n.a. | n.a. | n.a. | n.a. | n.a. | n.a. | n.a. | n.a. | n.a. | 0.02 | 0.05 | n.a. | n.a. |
| ZnO | 0.00 | 0.00 | n.a. | n.a. | n.a. | n.a. | n.a. | n.a. | 0.00 | 0.00 | 0.00 | 0.00 | n.a. | n.a. |
| Sum | 100.06 | 99.82 | 99.72 | 100.13 | 100.11 | 99.77 | 100.13 | 99.95 | 100.23 | 100.57 | 100.29 | 99.88 | 100.11 | 99.92 |
| Formula on the basis of 2 cations and 3 oxygens | | | | | | | | | | | | | | |
| Ti | 0.00 | 0.04 | 0.00 | 0.05 | 0.00 | 0.05 | 0.00 | 0.11 | 0.00 | 0.04 | 0.00 | 0.03 | 0.00 | 0.07 |
| Cr+V | 0.00 | 0.02 | 0.00 | 0.02 | 0.00 | 0.01 | 0.00 | 0.01 | 0.01 | 0.01 | 0.01 | 0.02 | 0.01 | 0.01 |
| Al | 1.91 | 0.12 | 1.91 | 0.13 | 1.91 | 0.14 | 1.90 | 0.08 | 1.85 | 0.09 | 1.83 | 0.14 | 1.83 | 0.12 |
| $Fe^{3+}$ | 0.09 | 1.78 | 0.09 | 1.74 | 0.09 | 1.74 | 0.10 | 1.69 | 0.14 | 1.80 | 0.16 | 1.79 | 0.16 | 1.74 |
| $Fe^{2+}$ | 0.00 | 0.00 | 0.00 | 0.02 | 0.00 | 0.01 | 0.00 | 0.03 | 0.00 | 0.00 | 0.00 | 0.01 | 0.00 | 0.02 |
| Mn | 0.00 | 0.00 | 0.00 | 0.00 | | 0.00 | | 0.00 | 0.00 | 0.00 | 0.00 | | | 0.00 |
| Mg | 0.00 | 0.03 | 0.00 | 0.03 | 0.00 | 0.03 | 0.00 | 0.07 | 0.00 | 0.05 | 0.00 | | | 0.03 |
| Ca + Ni + Zn | 0.00 | 0.01 | 0.00 | 0.01 | 0.00 | 0.01 | | 0.01 | 0.00 | 0.01 | 0.00 | 0.00 | 0.00 | 0.01 |
| $X_{Al_2O_3}$ | 0.96 | 0.07 | 0.95 | 0.08 | 0.95 | 0.08 | 0.95 | 0.05 | 0.93 | 0.06 | 0.92 | 0.08 | 0.92 | 0.07 |
| $X_{Fe_2O_3}$ | 0.04 | 0.93 | 0.05 | 0.92 | 0.05 | 0.92 | 0.05 | 0.95 | 0.07 | 0.94 | 0.08 | 0.92 | 0.08 | 0.93 |

n.a. = not analysed; b.d.l. = below detection limit; *$Fe_2O_3$ and FeO are calculated from charge balance; other data (EDS) are given in Table S4 (Supplementary material).

Seryotkin *et al.*, 2012; Galuskin *et al.*, 2015*c*) and for melted combustion metamorphism rocks from natural coal fires and coal-mine burned dumps (Sokol *et al.*, 2005; Grapes, 2011; Grapes *et al.*, 2011 and references therein).

### *Genesis and temperature estimation for the opaque segregation with corundum*

The origin of the corundum-bearing opaque segregation (as well as other opaque assemblages) in the Hatrurim Basin plagioclase-clinopyroxene rock remains enigmatic. In principle, they might result from high-temperature transformation of segregations with Al- and Fe-rich oxy/hydroxides (gibbsite, diaspore, böhmite and goethite) originally present in sediments. Note however that all opaque assemblages are localised inside or near large vesicles. In this respect, another possibility might be that hot oxidised gases provoked local melting of hornfels and subsequent recrystallization with Fe–Al-oxide components accumulating into, or near, gas vesicles (Sharygin *et al.*, 2008*b*). The participation of hot gas jets in a melting event is supported by the presence of fluid inclusions in the Hatrurim corundum (Fig. 4). Possibly, the gas effect was a one-time event, which led to formation of both the paralava and Fe–Al-oxide opaque assemblages. Nevertheless, all the Fe–Al-oxide associations are

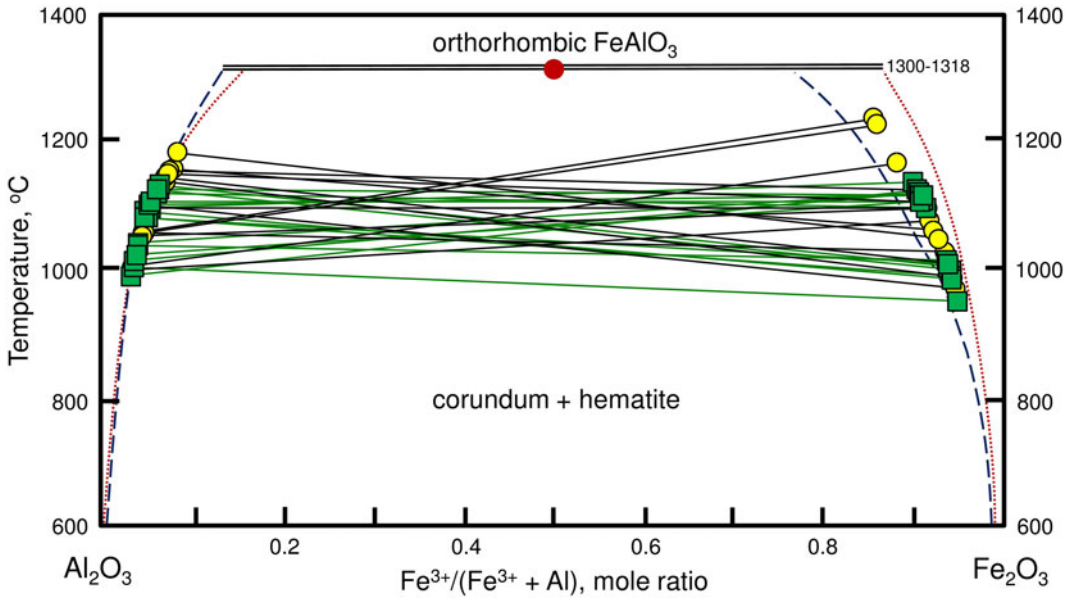


**Fig. 9.** Compositions of Fe-rich corundum and Al-rich hematite from the opaque segregation in plagioclase-clinopyroxene rock (Hatrurim Basin) on the $Al_2O_3$–$Fe_2O_3$ diagram after Muan and Gee (1956), Popović *et al.* (1995), Polli *et al.* (1996), Majzlan *et al.* (2002) and Feenstra *et al.* (2005). Dotted curve = data from Majzlan *et al.* (2002); dashed curve = data from Feenstra *et al.* (2005). Our data: circle is WDS spot analysis (1–2 μm); square is EDS rastered analysis (>3 × 3 μm). Initial data see Tables 3 and S5. Values for hematite were assumed as intermediate between two experimental lines.

quite different in mineralogy, possibly due to variable rate of temperature decrease (quenching) near individual vesicles. The maximum temperature for crystallisation of the Hatrurim assemblage with orthorhombic $FeAlO_3$ may be estimated as $T \geq 1318$°C (Sharygin and Sokol, 2017) according to experimental data for the system $Al_2O_3$–$Fe_2O_3$ (Muan and Gee, 1956; Popović *et al.*, 1995; Polli *et al.*, 1996; Majzlan *et al.*, 2002). It should be noted that natural orthorhombic ε-$Fe_2O_3$ (luogufengite) was also noted in vesicles, in late Pleistocene basaltic scoria from the Menan Volcanic Complex, Idaho, USA (Xu *et al.*, 2017). This mineral is considered to be an oxidation product of Fe-bearing basaltic glass at high temperature and is associated with maghemite and hematite.

The Hatrurim corundum-bearing assemblage (Figs 1,2) apparently crystallised at a lower temperature. In general, the presence of hibonite, spinel, Fe-rich corundum and Al-rich hematite indicates high-temperature crystallization (>900–1000°C). In addition, the absence of orthorhombic $FeAlO_3$ implies a temperature lower than 1318°C, as according to the $Al_2O_3$–$Fe_2O_3$ diagram the phase $FeAlO_3$ should inevitably decay with gradual temperature decrease into Fe-rich corundum and Al-rich hematite (Muan and Gee, 1956; Polli *et al.*, 1996; Majzlan *et al.*, 2002; Feenstra *et al.*, 2005). More exact constraints on the crystallization temperature of the corundum-bearing assemblage were obtained using the corundum–hematite pair. The limitations in application of this pair as a geothermometer were discussed by Feenstra *et al.* (2005). Primarily, the available experimental data for the behaviour of hematite at high temperatures are controversial (Majzlan *et al.*, 2002, Feenstra *et al.*, 2005), possibly, because of different quenching conditions, though the data for corundum are more consistent. Moreover, hematite from the Hatrurim corundum-bearing assemblage obviously contains oriented exsolution structures of corundum (Fig. 3, Fig. S6) indicating further solid phase decay after the corundum-hematite co-crystallisation. Thus, the concentration of $Fe_2O_3$ in corundum in the case of the corundum-hematite coexistence could be used for a better temperature estimation. In general, the Fe-rich corundum + Al-rich hematite + spinel + hibonite assemblage in the plagioclase-clinopyroxene rock at Hatrurim Basin allows the temperature to be estimated as 1000–1200°C (Fig. 9).

It should be noted that all multi-stage transformations in the plagioclase-clinopyroxene rock investigated (initial siliceous marly sediment → hornfels → paralava → segregation of Fe–Al–Mg-oxides) are related to crystallisation at high oxygen fugacity (possibly higher or near the HM buffer). In the case of the corundum-bearing assemblage (as the culmination of the combustion metamorphic process) it is indicated by: (1) the presence of hematite; (2) high concentrations of $Fe_2O_3$ in corundum, hibonite and spinel; and (3) gradual increasing of the esseneite component in clinopyroxene.

## Final remarks

The presence of abundant hematite incrustations around cavities in rocks is a common phenomenon for the Hatrurim Basin, especially for the 'olive unit' (Vapnik *et al.*, 2007). However, its formation (at active participation of a gas phase) does not always suggest a very high-temperature process. Crystallisation of the specific hibonite-spinel-corundum-hematite association in the Hatrurim Basin plagioclase-clinopyroxene rock can be assumed at 1000–1200°C using the corundum–hematite pair (Fig. 9). Feenstra *et al.* (2005) noted that "the corundum–hematite solvus has limited potential as a geothermometer because of the scarcity of suitable rock types for application and the restricted $Fe^{3+}$–Al exchange in the solution at $T \leq 1000$°C that introduces large inaccuracy in $T$". Meanwhile, the Hatrurim Basin is an example of realisitic temperature evaluations for both the host rock and this specific mineral pair.

**Supplementary material.** To view supplementary material for this article, please visit https://doi.org/10.1180/mgm.2018.138

**Acknowledgements.** The author thanks N.S. Karmanov, M.V. Khlestov, L.N. Pospelova and E.N. Nigmatulina for help with scanning microscope and microprobe studies at the V.S. Sobolev Institute of Geology and Mineralogy, Novosibirsk, Russia. E.V. Sokol (IGM, Novosibirsk, Russia) and Ye. Vapnik (Beer-Sheva, Israel) are thanked for helpful comments on an earlier version of the manuscript. The last version of the manuscript was improved through comments and suggestions by T. Perepelova, a translator of an Elsevier journal (IGM, Novosibirsk), L.A. Hartmann and an anonymous reviewer. This work was supported by the Russian Science Foundation (grant 17-17-01056).

## References

Agrell S.O., Chinner G.A. and Rowley P.D. (1999) The black skarns of Pine Canyon, Piute County, Utah. *Geological Magazine*, **136**, 343–359.

Ananyev S.A., Konovalenko S.I., Rastsvetaeva R.K., Aksenov S.M., Chukanov N.V., Sapozhnikov A.N., Zagorsky V.E. and Virus A.A. (2011) Tashelgite, $CaMgFe^{2+}Al_9O_{16}(OH)$, a new mineral species from calc-skarnoid in Gorny Shoria. *Geology of Ore Deposits*, **53**, 751–757.

Bentor Y.K., Gross Sh. and Heller L. (1963) High temperature minerals in non-metamorphosed sediments in Israel. *Nature*, **199**, 478–479.

Bentor Y.K. and Vroman A. (1960) *The Geological Map of Israel 1:100000, Sheet 16 – Mount Sedom (with explanatory text)*. Geological Survey of Israel, Jerusalem.

Britvin S.N., Murashko M.N., Vapnik Y., Polekhovsky Y.S. and Krivovichev S.V. (2015) Earth's phosphides in Levant and insights into the source of Archean prebiotic phosphorus. *Scientific Reports*, **5**, 8355.

Burg A., Starinsky A., Bartov Y. and Kolodny Ye. (1991) Geology of the Hatrurim Formation ("Mottled Zone") in the Hatrurim basin. *Israel Journal of Earth Sciences*, **40**, 107–124.

Burg A., Kolodny Ye. and Lyakhovsky V. (1999) Hatrurim-2000: the "Mottled Zone" revisited, forty years later. *Israel Journal of Earth Sciences*, **48**, 209–223.

Caracas R. (2010) Spin and structural transitions in $AlFeO_3$ and $FeAlO_3$ perovskite and post-perovskite. *Physics of the Earth and Planetary Interiors*, **182**, 10–17.

Doyle P.M., Schofield P.F., Berry A.J., Walker A.M. and Knight K.S. (2014) Substitution of $Ti^{3+}$ and $Ti^{4+}$ in hibonite ($CaAl_{12}O_{19}$). *American Mineralogist*, **99**, 1369–1382.

Feenstra A., Samann S., Wunder B., 2005. An experimental study of Fe-Al-solubility in the system corundum-hematite up to 40 kbar and 1300°C. *Journal of Petrology*, **46**, 1881–1892.

Fleischer L. and Varshavsky A. (2002) *A Lithostratigraphic Data Base of Oil and Gas Wells Drilled in Israel*. Ministry of National Infrastructures, Oil and Gas Unit. Report No. OG/9/02. Geophysical Institute of Israel, Report No 874/202/02, 280 p.

Galuskin E.V., Galuskina I.O., Kusz J., Armbruster T., Marzec K.M., Dzierżanowski P. and Murashko M. (2014) Vapnikite $Ca_3UO_6$ – a new double-perovskite mineral from pyrometamorphic larnite rocks of the Jabel Harmun, Palestinian Autonomy, Israel. *Mineralogical Magazine*, **78**, 571–581.

Galuskin E.V., Gfeller F., Armbruster T., Galuskina I.O., Vapnik Ye., Dulski M., Murashko M., Dzierżanowski P., Sharygin V.V., Krivovichev S.V. and Wirth R. (2015*a*) Mayenite supergroup, Part III: Fluormayenite, $Ca_{12}Al_{14}O_{32}[\square_4F_2]$ and fluorkyuygenite, $Ca_{12}Al_{14}O_{32}[(H_2O)_4F_2]$, two new minerals from pyrometamorphic rock of the Hatrurim Complex, Southern Levant. *European Journal of Mineralogy*, **27**, 123–136.

Galuskin E.V., Gfeller F., Armbruster T., Galuskina I.O., Vapnik Y., Murashko M., Wlodyka R. and Dzierżanowski P. (2015*b*). New minerals with a modular structure derived from hatrurite from the pyrometamorphic Hatrurim Complex. Part I. Nabimusaite, $KCa_{12}(SiO_4)_4(SO_4)_2O_2F$, from larnite rocks of Jabel Harmun, Palestinian Autonomy, Israel. *Mineralogical Magazine*, **79**, 1061–1072.

Galuskin E.V., Gfeller F., Galuskina I.O., Pakhomova A., Armbruster T., Vapnik Ye., Wlodyka R., Dzierżanowski P. and Murashko M. (2015*c*) New minerals with a modular structure derived from hatrurite from the pyrometamorphic Hatrurim Complex. Part II. Zadovite, $BaCa_6[(SiO_4)(PO_4)](PO_4)_2F$ and aradite, $BaCa_6[(SiO_4)(VO_4)](VO_4)_2F$, from paralavas of the Hatrurim Basin, Negev Desert, Israel. *Mineralogical Magazine*, **79**, 1073–1087.

Galuskin E.V., Galuskina I.O., Gfeller F., Krueger B., Kusz J., Vapnik, Ye., Dulski M. and Dzierzanowski P. (2016) Silicocarnotite, $Ca_5[(SiO_4)(PO_4)](PO_4)$, a new "old" mineral from the Negev Desert, Israel, and the ternesite-silicocarnotite solid solution: indicators of high-temperature alteration of pyrometamorphic rocks of the Hatrurim Complex, Southern Levant. *European Journal of Mineralogy*, **28**, 105–123.

Galuskin E.V., Gfeller F., Galuskina I.O., Armbruster T., Krzatala A., Vapnik Y., Kusz J., Dulski M., Gardocki M., Gurbanov A.G. and Dzierżanowski P. (2017) New minerals with a modular structure derived from hatrurite from the pyrometamorphic rocks. Part III. Gazeevite, $BaCa_6(SiO_4)_2(SO_4)_2O$, from Israel and the Palestine Autonomy, South Levant, and from South Ossetia, Greater Caucasus. *Mineralogical Magazine*, **81**, 499–513.

Galuskina I.O., Vapnik Y., Lazic B., Armbruster T., Murashko M. and Galuskin E.V. (2014) Harmunite $CaFe_2O_4$: A new mineral from the Jabel Harmun, West Bank, Palestinian Autonomy, Israel. *American Mineralogist*, **99**, 965–975.

Galuskina I.O., Galuskin E.V., Pakhomova A.S., Widmer R., Armbruster T., Krueger B., Grew E.S., Vapnik Ye., Dzierzanowski P. and Murashko M. (2017*a*) Khesinite, $Ca_4Mg_2Fe^{3+}_{10}O_4[(Fe^{3+}_{10}Si_2)O_{36}]$, a new rhonite-group (sapphirine supergroup) mineral from the Negev Desert, Israel – natural analogue of the SFCA phase. *European Journal of Mineralogy*, **29**, 101–116.

Galuskina I.O., Galuskin E.V., Prusik K., Vapnik Y., Juroszek R., Jeżak L. and Murashko M. (2017*b*) Dzierżanowskite, $CaCu_2S_2$ – a new natural thiocuprate from Jabel Harmun, Judean Desert, Palestine Autonomy, Israel. *Mineralogical Magazine*, **81**, 777–789.

Gardosh M., Kashai E., Salhov S., Shulman H. and Tannenbaum E. (1997) Hydrocarbon explosion in the southern Dead Sea area. Pp. 57–72 in: *The Dead Sea: the Lake and its Setting* (T.N. Niemi, Z. Ben-Avraham, J.R. Gat, editors). Oxford Press, Oxford, UK.

Gardosh M., Druckman Y., Buchbinder B. and Rybakov M. (2008) The Levant Basin Offshore Israel: Stratigraphy, Structure, Tectonic Evolution and Implications for Hydrocarbon Exploration. Revised edition. Geological Survey of Israel, Jerusalem, Report GSC/4, 119 pp.

Garfunkel Z. (1997) The history and formation of the Dead Sea basin. Pp. 36–56 in: *The Dead Sea: the Lake and its Setting* (T.N. Niemi, Z. Ben-Avraham, J.R. Gat, editors). Oxford Press, Oxford, UK.

Geller Y.I., Burg A., Halicz L. and Kolodny Y. (2012) System closure during the combustion metamorphic "Mottled Zone" event, Israel. *Chemical Geology*, **334**, 25–36.

Gilat A. (1998) Hydrothermal activity and hydro-explosions as a cause of natural combustion and pyrolysis of bituminous rocks: The case of Pliocene metamorphism in Israel (Hatrurim Formation). *Geological Survey of Israel: Current Research*, **11**, 96–102.

Grapes R. (2011) *Pyrometamorphism*. Second Edition. Springer Berlin Heidelberg, 365 pp.

Grapes R., Korzhova S., Sokol E. and Seryotkin Yu. (2011) Paragenesis of unusual Fe-cordierite (sekaninaite)-bearing paralava and clinker from the Kuznetsk coal basin, Siberia, Russia. *Contributions to Mineralogy and Petrology*, **162**, 253–273.

Gross Sh. (1977) *The Mineralogy of the Hatrurim Formation, Israel*. Geological Survey of Israel Bulletin, **70**, 80 pp.

Gross Sh. (1984) Occurrence of ye'elimite and ellestadite in an unusual cobble from the "pseudo-conglomerate" of the Hatrurim Basin, Israel. *Geological Survey of Israel, Current Research*, **1983–84**, 1–4.

Gvirtzman H. and Stanislavsky E. (2000) Palaeohydrology of hydrocarbon maturation, migration and accumulation in the Dead Sea Rift. *Basin Research*, **12**, 79–93.

Gur D., Steinitz G., Kolodny Y., Starinsky A. and McWilliams M. (1995) $^{40}Ar/^{39}Ar$ dating of combustion metamorphism ("Mottled Zone", Israel). *Chemical Geology*, **122**, 171–184.

Hall J.K., Krasheninnikov A., Hirsch F., Benjamini C. and Flexer A. (2005) *Geological framework of the Levant. Volume II: The Levantine Basin and Israel*. Historical Productions, Hall, Jerusalem, 826 p.

Hanesch M. (2009) Raman spectroscopy of iron oxides and (oxy)hydroxides at low laser power and possible applications in environmental magnetic studies. *Geophysical Journal International*, **177**, 941–948.

Hirsch F., Burg A. and Avni Y. (2010) *Geological Map of Israel. Scale 1:50,000. Arad sheet 15–IV*. Geological Survey of Israel, Jerusalem.

Izokh A.E., Smirnov S.Z., Egorova V.V., Tran T.A., Kovyazin S.V., Ngo T.P. and Kalinina V.V. (2010) The conditions of formation of sapphire and zircon in the areas of alkali-basaltoid volcanism in Central Vietnam. *Russian Geology and Geophysics*, **51**, 719–733.

Jubb A.M. and Allen H.C. (2010) Vibrational spectroscopic characterization of hematite, maghemite, and magnetite thin films produced by vapor deposition. *ACS Applied Materials and Interfaces*, **2**(10), 2804–2812.

Khoury H. and Nassir S. (1982) High temperature mineralization in Maqarin area, North Jordan. *Neues Jahrbuch für Mineralogie – Abhandlungen*, **144**, 197–213.

Khoury H.N., Sokol E.V., Kokh S.N., Seryotkin Y.V., Nigmatulina E.N., Goryainov S.V., Belogub E.V. and Clark I.D. (2016) Tululite, $Ca_{14}(Fe^{3+}, Al)(Al,Zn,Fe^{3+},Si,P,Mn,Mg)_{15}O_{36}$: a new Ca zincate-aluminate from combustion metamorphic marbles, central Jordan. *Mineralogy and Petrology*, **110**, 125–140.

Kokh S.N., Sokol E.V. and Sharygin V.V., 2014. Ellestadite-group minerals in combustion metamorphic rocks. Pp. 543–562 in: *Coal and Peat Fires: A Global Perspective* (G.B. Stracher, A. Prakash and E.V. Sokol, editors). Elsevier B.V., New York. Volume 3: Case studies – Coal fires.

Kolodny Y. (1979) Natural cement factory: a geological story. Pp. 203–216 in: *Cement Production and Use* (J. Skalny, editor). Franklin Pierce College, Rindge, New Hampshire, USA.

Kolodny Y. and Gross S. (1974) Thermal metamorphism by combustion of organic matter: isotopic and petrological evidence. *The Journal of Geology*, **82**, 489–506.

Kulikova K.V. and Varlamov D.A. (2006) The first finding of corundum in exsolution structures of oxides in gabbroic rocks from the Polar Urals. *Doklady of Earth Sciences*, **407**, 246–249.

Maercklin N., Haberland C., Ryberg T., Weber M. and Bartov Y. (2004) Imaging the Dead Sea Transform with scattered seismic waves. *Geophysical Journal International*, **158**, 179–186.

Majzlan J., Navrotsky A. and Evans B.J. (2002) Thermodynamics and crystal chemistry of the hematite-corundum solid solution and the $FeAlO_3$ phase. *Physics and Chemistry of Minerals*, **29**, 515–526.

Matthews A. and Gross Sh. (1980) Petrologic evolution of the "Mottled Zone" (Hatrurim) metamorphic complex of Israel. *Israel Journal of Earth Sciences*, **29**, 93–106.

Murashko M.N., Chukanov N.V., Mukhanova A.A., Vapnik Ye., Britvin S.N., Krivovichev S.V., Polekhovsky Yu.S. and Ivakin I.D. (2011) Barioferrite $BaFe^{3+}_{12}O_{19}$: a new mineral species of the magnetoplumbite group from the Hatrurim Formation in Israel. *Geology of Ore Deposits*, **53**, 558–563.

Muan A. and Gee C.L. (1956) Phase equilibrium studies in the system iron oxide – $Al_2O_3$ in air and at 1 atm. $O_2$ pressure. *Journal of the American Ceramic Society*, **39**, 207–214.

Nagashima M., Armbruster T. and Hainschwang T. (2010) A temperature-dependent structure study of gem-quality hibonite from Myanmar. *Mineralogical Magazine*, **74**, 871–885.

Nissenbaum A. and Goldberg M. (1980) Asphalts, heavy oils, ozocerite and gases in the Dead Sea Basin. *Organic Geochemistry*, **2**, 167–180.

Novikov I., Vapnik Ye. and Safonova I. (2013) Mud volcano origin of the Mottled Zone, South Levant. *Geoscience Frontiers*, **4**, 597–619.

Picard L.Y. and Golani U. (1965) *Geological Map of Israel. Scale 1:250,000. Northern Sheet, sheets 1–2*. Geological Survey of Israel, Jerusalem.

Pissas M., Stamopoulos D., Sanakis Y. and Simopoulos A. (2008) Magnetic properties of the magnetoelectric $Al_{2-x}Fe_xO_3$ ($x = 0.8$, 0.9 and 1). *Journal of Physics: Condensed Matter*, **20**, 415222.

Polli A.D., Lange F.E. and Levi C.G. (1996) Crystallization behavior and microstructure evolution of $(Al,Fe)_2O_3$ synthesized from liquid precursors. *Journal of American Ceramic Society*, **79**, 1745–1755.

Popović S., Ristić M. and Musić S. (1995) Formation of solid solutions in the system $Al_2O_3$–$Fe_2O_3$. *Materials Letters*, **23**, 139–142.

Pouchou I.L. and Pichoir F. (1985) "PaP" (phi-rho-z) procedure for improved quantitative microanalysis. Pp. 104–106. in: *Microbeam Analysis* (I.T. Armstrong, editor). San Francisco Press; San Francisco, USA.

Rajesh V.J., Arai S., Santosh M. and Tamura A. (2010) LREE-rich hibonite in ultrapotassic rocks in southern India. *Lithos*, **115**, 40–50.

Reverdatto V.V. (1970) *Facies of Contact Metamorphism*. Nedra, Moscow, 271 p. [in Russian].

Sakurai S., Namai A., Hashimoto K. and Ohkoshi S. (2009) First observation of phase transformation of all four $Fe_2O_3$ phases ($\gamma \rightarrow \varepsilon \rightarrow \beta \rightarrow \alpha$-phase). *Journal of American Chemical Society*, **131**, 18299–18303.

Seryotkin Y.V., Sokol E.V. and Kokh S.N. (2012) Natural pseudowollastonite: crystal structure, associated minerals, and geological context. *Lithos*, **133–135**, 75–90.

Sharygin V.V. (2010) Mineralogy of Ca-rich metacarbonate rocks from burned dumps of the Donetsk coal basin. Pp. 162–170. in: *Proceedings of "ICCFR2–Second Int. Conf. on Coal Fire Research"*, Berlin, Germany.

Sharygin V.V. and Sokol E.V. (2017) Phase $FeAlO_3$ in plagioclase-clinopyroxene rock at Hatrurim Basin, Israel. Pp. 323–325 in: *200th Anniversary Meeting of the Russian Mineralogical Society*. S.-Petersburg, Vol. 2. [in Russian].

Sharygin V.V., Vapnik Ye., Sokol E.V., Kamenetsky V.S. and Shagam R. (2006) Melt inclusions in minerals of schorlomite-rich veins of the Hatrurim Basin, Israel: composition and homogenization temperatures. Pp. 189–192 in: *ACROFI I*, program with abstracts (P. Ni and Z. Li, editors). Nanjing University PH, China.

Sharygin V.V., Sokol E.V. and Vapnik Ye. (2008*a*) Minerals of the pseudobinary perovskite–brownmillerite series from combustion metamorphic larnite rocks of the Hatrurim Formation (Israel). *Russian Geology and Geophysics*, **49**, 709–726.

Sharygin V.V., Vapnik Ye. and Sokol E.V. (2008*b*) Association of hibonite-corundum-spinel-hematite in clinopyroxene-plagioclase hornfels of the Hatrurim Formation, Israel. Pp. 125–128 in: *Proceedings of "Fedorov session-2008"*. S.-Petersburg, Russia [in Russian].

Sharygin V.V., Lazic B., Armbruster T.M., Murashko M.N., Wirth R., Galuskina I.O., Galuskin E.V., Vapnik Ye., Britvin S.N. and Logvinova A.M. (2013) Shulamitite $Ca_3TiFe^{3+}AlO_8$ – a new perovskite-related mineral from Hatrurim Basin, Israel. *European Journal of Mineralogy*, **25**, 97–111.

Shen A., Bartov Y., Rosensaft M. and Weissbort T. (1998) *Geological Map of Israel. Scale 1:200,000, sheets 1–4*. Geological Survey of Israel, Jerusalem.

Simon S.B. and Grossman L. (2003) Petrography and mineral chemistry of the anhydrous component of the Tagish Lake carbonaceous chondrite. *Meteoritics and Planetary Science*, **38**, 815–825.

Simon S.B., Davis A.M. and Grossman L. (2001) Formation of orange hibonite, as inferred from some Allende inclusions. *Meteoritics and Planetary Science*, **36**, 331–350.

Sokol E.V., Maksimova N.V., Nigmatulina E.N., Sharygin V.V. and Kalugin V.M. (2005) *Combustion Metamorphism*. Izd. SO RAN, Novosibirsk. 284 pp. [in Russian].

Sokol E.V., Novikov I.S., Vapnik Ye. and Sharygin V.V. (2007) Gas fire from mud volcanoes as a trigger for the appearance of high-temperature pyrometamorphic rocks of the Hatrurim Formation (Dead Sea area). *Doklady of Earth Sciences*, **413**, 474–480.

Sokol E.V., Novikov I.S., Zateeva S.N., Sharygin V.V. and Vapnik Ye. (2008) Pyrometamorphic rocks of the spurrite-merwinite facies as indicators of hydrocarbon discharge zones (the Hatrurim Formation, Israel). *Doklady of Earth Sciences*, **420**, 608–614.

Sokol E., Novikov I., Zateeva S., Vapnik Ye., Shagam R. and Kozmenko O. (2010) Combustion metamorphic rocks as indicators of fossil mud volcanism: New implications for the origin of the Mottled Zone, Dead Sea rift area. *Basin Research*, **22**, 414–438.

Sokol E.V., Kozmenko O.A., Kokh S.N. and Vapnik Ye. (2012) Gas reservoirs in the Dead Sea area: evidence from chemistry of combustion metamorphic rocks in Nabi Musa fossil mud volcano. *Russian Geology and Geophysics*, **53**, 745–762.

Sokol E.V., Gaskova O.L., Kozmenko O.A., Kokh S.N., Vapnik E.A., Novikova S.A. and Nigmatulina E.N. (2014*a*) Clastic dikes of the

Hatrurim basin (western flank of the Dead Sea) as natural analogues of alkaline concretes: Mineralogy, solution chemistry, and durability. *Doklady of Earth Sciences*, **459**, 1436–1441.

Sokol E.V., Kokh S.N., Vapnik Y., Thiery V. and Korzhova S.A. (2014*b*) Natural analogs of belite sulfoaluminate cement clinkers from Negev Desert, Israel. *American Mineralogist*, **99**, 1471–1487.

Sokol E., Kozmenko O., Smirnov S., Sokol I., Novikova S., Tomilenko A., Kokh S., Ryazanova T., Reutsky V., Bul'bak T., Vapnik Y. and Deyak M. (2014*c*) Geochemical assessment of hydrocarbon migration phenomena: Case studies from the south-western margin of the Dead Sea Basin. *Journal of Asian Earth Sciences*, **93**, 211–228.

Sokol E.V., Seryotkin Yu.V., Kokh S.N., Vapnik Ye., Nigmatulina E.N., Goryainov S.V., Belogub E.V. and Sharygin V.V. (2015) Flamite (Ca,Na,K)$_2$(Si,P)O$_4$, a new mineral from the ultrahigh-temperature combustion metamorphic rocks, Hatrurim Basin, Negev Desert, Israel. *Mineralogical Magazine*, **79**, 583–596.

Techer I., Khoury H.N., Salameh E., Rassineux F., Claude C., Clauer N., Pagel M., Lancelot J., Hamelin B. and Jacquot E. (2006) Propagation of high-alkaline fluids in an argillaceous formation: Case study of the Khushaym Matruk natural analogue (Central Jordan). *Journal of Geochemical Exploration*, **90**, 53–67.

Tucek J., Machala L., Ono S., Namai A., Yoshikiyo M., Imoto K., Tokoro H., Ohkoshi S. and Zboril R. (2015) Zeta-$Fe_2O_3$ – A new stable polymorph in iron(III) oxide family. *Scientific Reports*, **5**, 15091.

Ulianov A., Kalt A. and Pettke T. (2005) Hibonite, Ca(Al,Cr,Ti,Si,Mg,$Fe^{2+}$)$_{12}$O$_{19}$, in granulite xenoliths from the Chyulu Hills volcanic field, Kenya. *European Journal of Mineralogy*, **17**, 357–366.

Vapnik Ye., Sokol E., Murashko M. and Sharygin V. (2006) The enigma of Hatrurim. *Mineralogical Almanac*, **10**, 69–77.

Vapnik Y., Sharygin V.V., Sokol E.V. and Shagam R. (2007) Paralavas in combustion metamorphic complex at the Hatrurim Basin, Israel. Pp. 133–153 in: *Geology of Coal Fires: Case Studies from Around the World* (G. Stracher, editor). GSA Review in Engineering Geology, XVIII.

Wang H.-W., Anovitz L.M., Burg A., Cole D.R., Allard L.F., Jackson A.J., Stack A.G. and Rother G. (2013) Multi-scale characterization of pore evolution in a combustion metamorphic complex, Hatrurim basin, Israel: Combining (ultra) small-angle neutron scattering and image analysis. *Geochimica et Cosmochimica Acta*, **121**, 339–362.

Xu H., Lee S. and Xu H. (2017) Luogufengite: A new nano-mineral of $Fe_2O_3$ polymorph with giant coercive field. *American Mineralogist*, **102**, 711–719.

Zateeva S.N., Sokol E.V. and Sharygin V.V. (2007) Specificity of pyrometamorphic minerals of the ellestadite group. *Geology of Ore Deposits*, **49**, 792–805.

Zboril R., Mashlan M., Krausova D. and Pikal P. (1999) Cubic β-$Fe_2O_3$ as the product of the thermal decomposition of $Fe_2(SO_4)_3$. *Hyperfine Interactions*, **120**, 497–501.

Zeigler M. (2001) Late Permian to Holocene paleofacies evolution of the Arabian plate and its hydrocarbon occurrences. *GeoArabia*, **6**, 445–504.

# Supplementary data

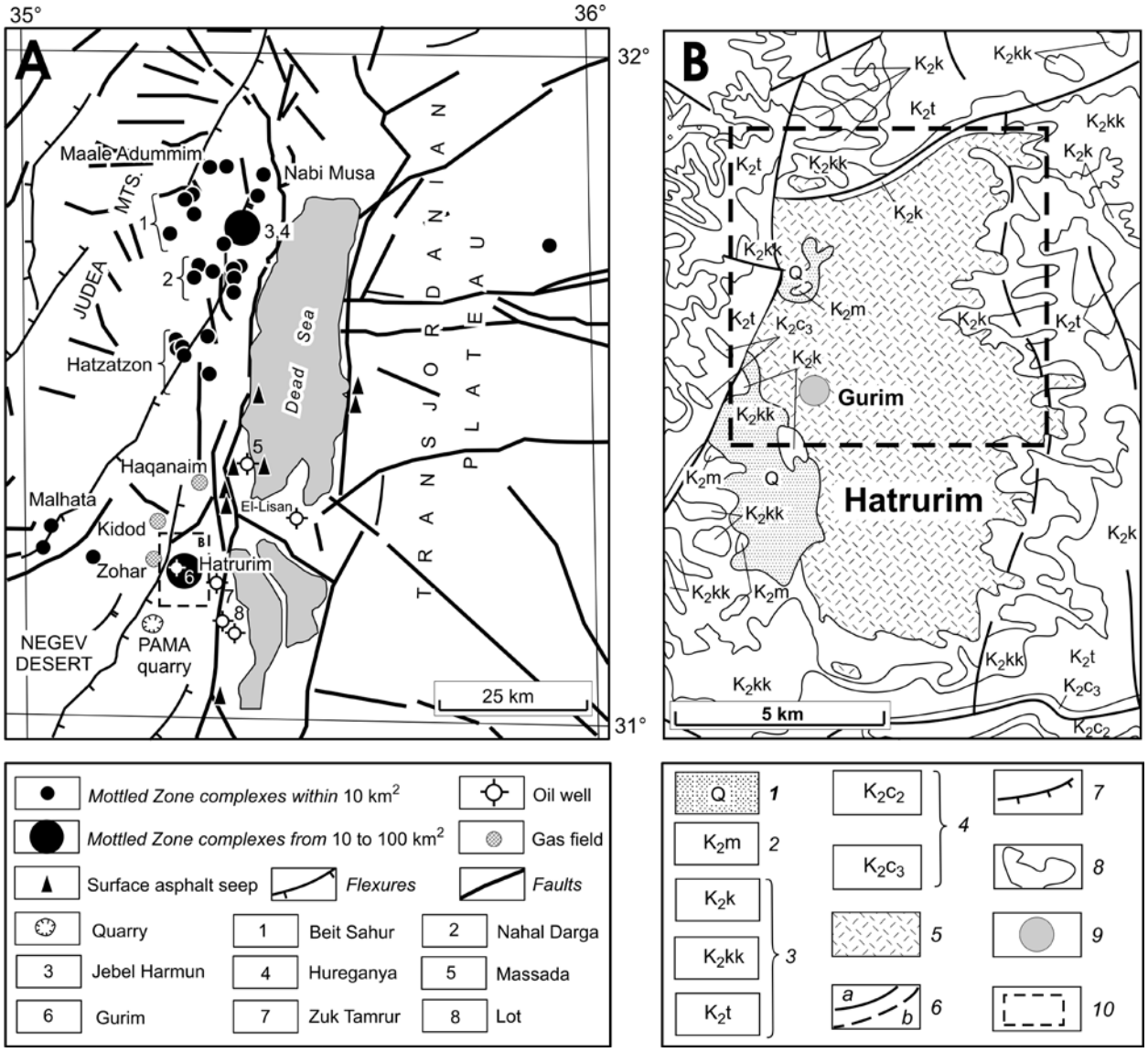


**Fig. S1 A-B.**

**A.** Generalized geology of the Dead Sea Transform area with locations of the Mottled Zone complexes, gas fields, asphalt shows, and oil wells, after (Nissenbaum and Goldberg, 1980; Gardosh et al., 1996, 2008; Hall et al., 2005; Sokol et al., 2010, 2014).

**B.** Generalized geological map of Hatrurim Basin. Geology simplified after the 1:200,000 Geological Map of Israel (Bentor et al., 1965; Picard and Golani, 1965; Shen et al., 1998), after (Hall et al., 2005), as well as after (Burg et al., 1991; 1999; Sokol et al., 2007, 2010).

1 – Pleistocene sand, carbonate, and clay marine sediments (Q);

2 – Maastrichtian organic-rich marine chalk ($K_2m$);

3 – Campanian ($K_2k$), Santonian ($K_2kk$), and Turonian ($K_2t$) limestone, chalk, and dolomite with chert and phosphorite intercalations;

4 – Cenomanian ($K_2c_3$, $K_2c_2$) limestone, dolomite, and chalk;

5 – Hatrurim Formation rocks;

6 – observed (a) and inferred (b) faults;

7 – folds;

8 – stratigraphic boundaries;

9 – Gurim anticline;

10 – fragment of map, shown in Fig. S1 C.

Bentor, Y.K., Vroman, A., Zak, I. (Eds.), 1965. Geological Map of Israel. Scale 1:250,000. Southern Sheet, Geol. Surv. Isr., Jerusalem, sheets 1–2.

Burg, A., Starinsky, A., Bartov, Y., Kolodny, Y., 1991. Geology of the Hatrurim Formation ("Mottled Zone") in the Hatrurim basin. Isr. J. Earth Sci. 40, 107–124.

Burg, A., Kolodny, Ye., Lyakhovsky, V., 1999. Hatrurim-2000: The "Mottled Zone" revisited, forty years later. Isr. J. Earth Sci. 48, 209–223.

Gardosh, M., Kashai, E., Salhov, S., Shulman, H., Tannenbaum, E., 1996. Hydrocarbon explosion in the southern Dead Sea area. In: Niemi, T.N., Ben-Avraham, Z., Gat, J.R. (Eds.), The Dead Sea: the Lake and its Setting. Oxford Press, Oxford, pp. 57–72.

Gardosh, M., Druckman, Y., Buchbinder, B., Rybakov, M., 2008. The Levant Basin Offshore Israel: Stratigraphy, Structure, Tectonic Evolution and Implications for Hydrocarbon Exploration. Revised edition. Geological Survey of Israel Report GSC/4, Jerusalem, 119 p.

Hall, J.K., Krasheninnikov, A., Hirsch, F., Benjamini, C., Flexer, A., 2005. Geological framework of the Levant. Volume II: The Levantine Basin and Israel. Historical Productions - Hall, Jerusalem, pp. 826.

Nissenbaum, A., Goldberg, M., 1980. Asphalts, heavy oils, ozocerite and gases in the Dead Sea Basin. Org. Geochem. 2, 167–180.

Picard, L.Y., Golani, U. (Eds.), 1965. Geological Map of Israel. Scale 1:250,000. Northern Sheet. Geol. Surv. Isr., Jerusalem, sheets 1–2.

Shen, A., Bartov, Y., Rosensaft, M., Weissbort, T. (Eds.), 1998. Geological Map of Israel. Scale 1:200,000. Geol. Surv. Isr., Jerusalem, sheets 1–4.

Sokol, E.V., Novikov, I.S., Vapnik, Ye., Sharygin, V.V., 2007. Gas fire from mud volcanoes as a trigger for the appearance of high temperature pyrometamorphic rocks of the Hatrurim Formation (Dead Sea area). Dokl. Earth Sci. 413A, 474–480.

Sokol, E.V., Novikov, I.S., Zateeva, S.N., Vapnik, Ye, Shagam, R., Kozmenko, O.A., 2010. Combustion metamorphism in Nabi Musa dome: New implications for a mud volcanic origin of the Mottled Zone, Dead Sea area. Basin Res. 22 (6), 414–438.

Sokol E., Kozmenko O., Tomilenko A., Sokol I., Smirnov S., Korzhova S., Kokh S., Ryazanova T., Reutsky V., Vapnik Ye., Deyak M. Geochemical assessment of hydrocarbons migration phenomena: Case studies from the south-western margin of the Dead Sea Basin // Journal of Asian Earth Sciences, 2014, v. 93, p. 211-228

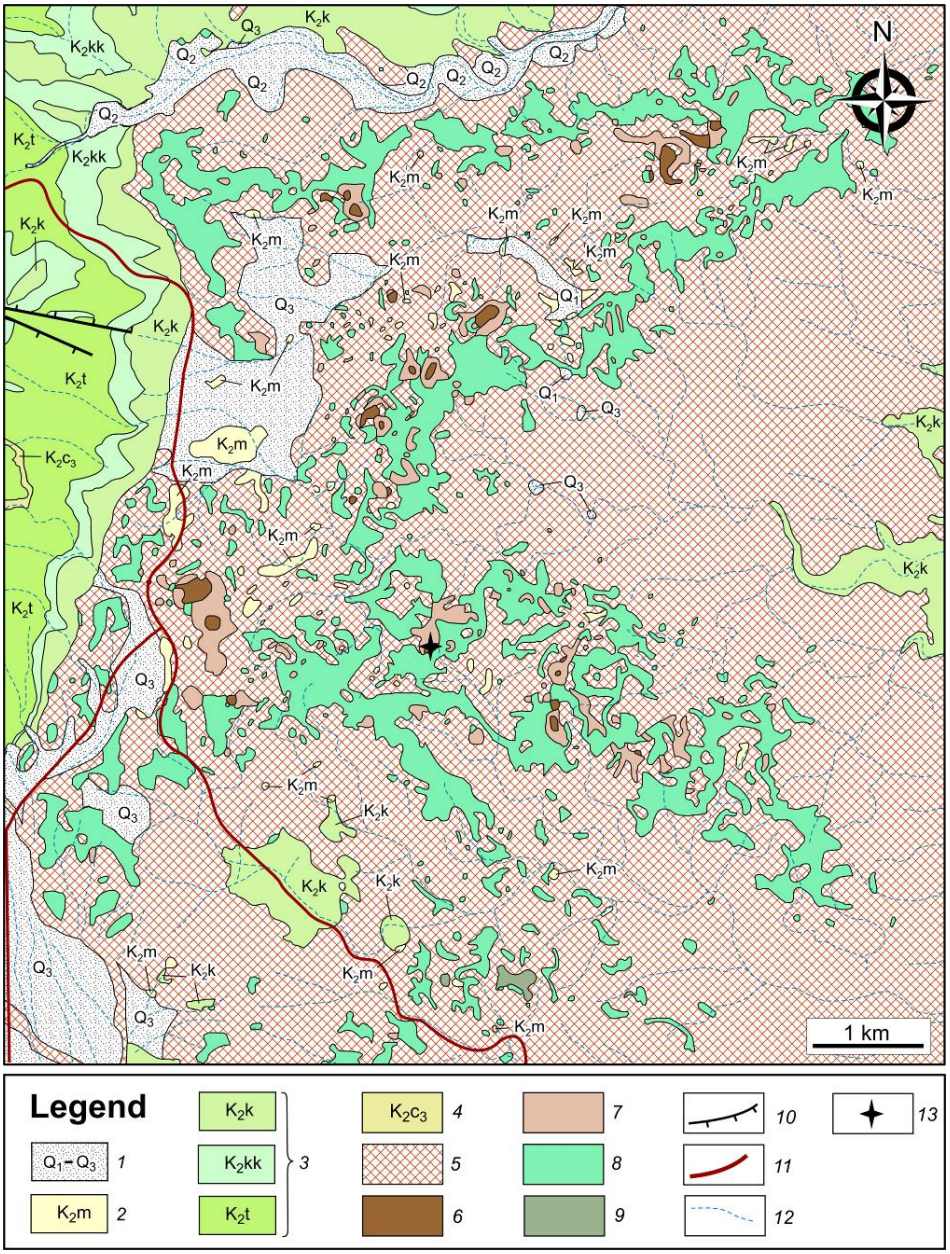


**Fig. S1 C.** Geological map of NW part of Hatrurim Basin, modified after the 1:50.000 Geological Map of Israel (Hirsch et al., 2010).

1 – Pleistocene terrace conglomerates ($Q_1$, $Q_2$, $Q_3$);
2 – Maastrichtian organic-rich marine chalk ($K_2m$);
3 – Campanian ($K_2k$), Santonian ($K_2kk$), and Turonian ($K_2t$) limestone, chalk, and dolomite with chert and phosphorite intercalations;
4 – Cenomanian ($K_2c_3$) limestone, dolomite, and chalk;
5 – Low-grade Hatrurim Formation rocks;
6 – Larnite rocks (High-grade Hatrurim Formation rocks);
7 – the "Olive rocks" (Hatrurim Formation);
8 – Spurrite marbles (Medium-grade Hatrurim Formation rocks);
9 – Pseudoconglomerates;
10 – Faults;
11 – Road;
12 – Wadi;
13 – Sampling site.

Hirsch, F., Burg, A., Avni, Y. (Eds.), 2010. Geological Map of Israel. Scale 1:50,000. Geol. Surv. Isr., Jerusalem, Arad sheet 15–IV.

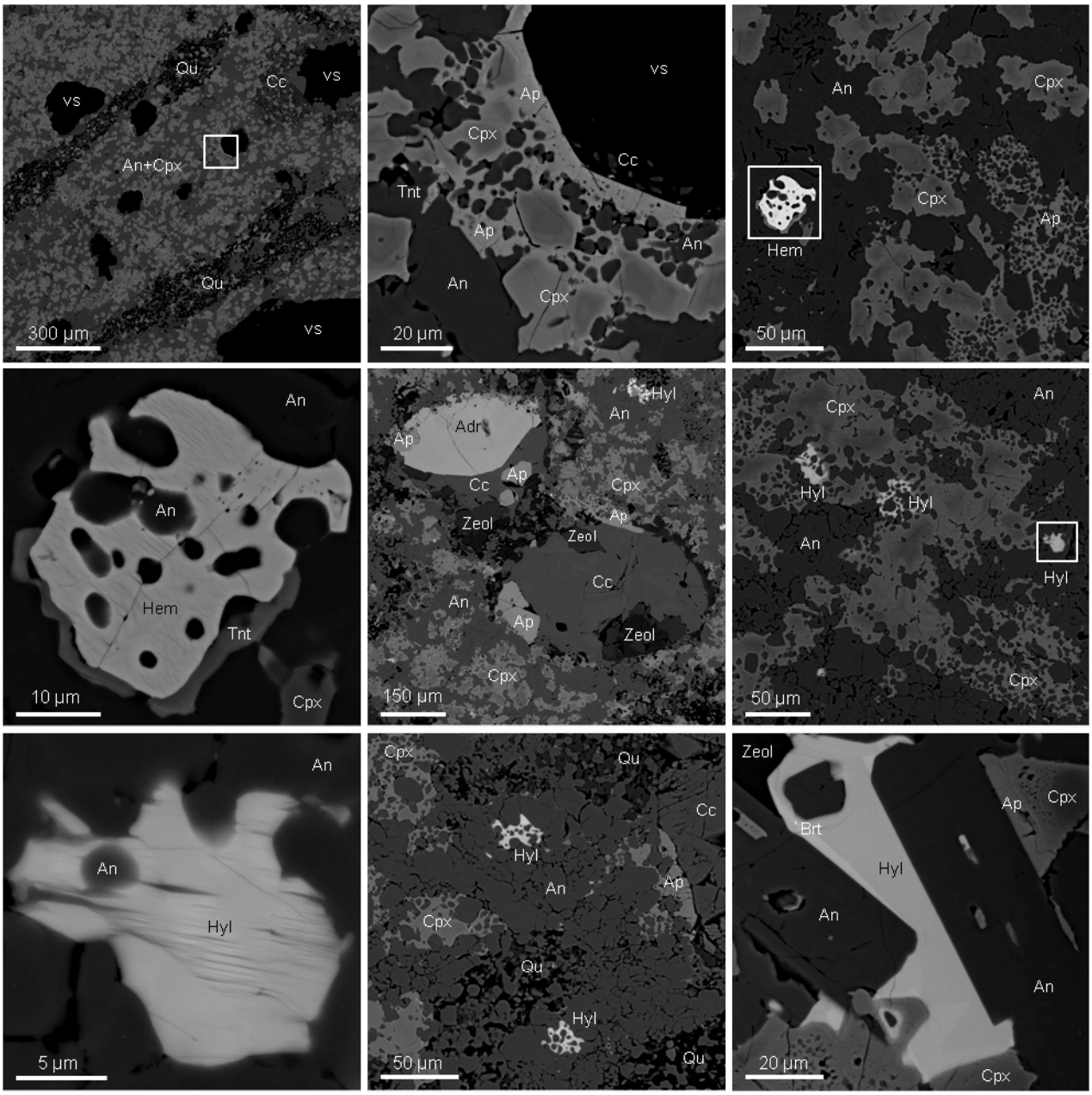


Fig. S2. Mineral association in plagioclase-clinopyroxene rock, Hatrurim Basin, BSE images.
Symbols: An – anorthite; Cpx – clinopyroxene; Qu – $SiO_2$ polymorph; Ap – fluorapatite; Ttn – titanite; Hem – hematite, Adr – Ti-andradite; Cc – calcite; Zeol – zeolite-supergroup minerals; Hyl – "hyalophane"; Brt – baryte; vs – vesicle.

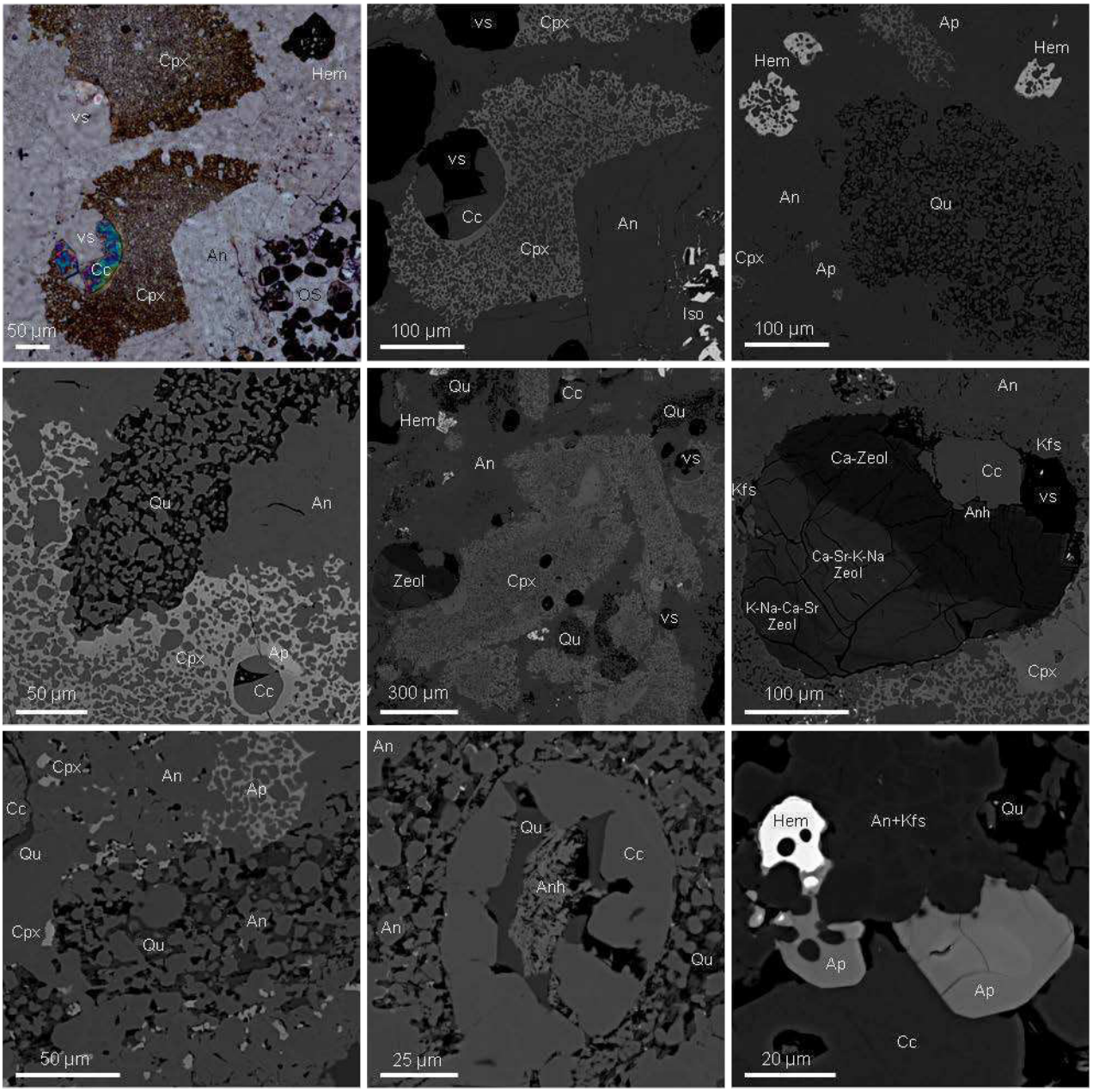


Fig. S3. Mineral relations in leucocratic zone of plagioclase-clinopyroxene rock, Hatrurim Basin, BSE images and photo in polarized light.

Symbols: An – anorthite; Hem – hematite; Cc – calcite; vs – vesicle; OS – opaque corundum-bearing segregation; Cpx - clinopyroxene; Ap – fluorapatite; Qu – $SiO_2$ polymorph; Zeol – zeolite-supergroup minerals; Kfs – K-feldspar; Anh – bassanite-anhydride.

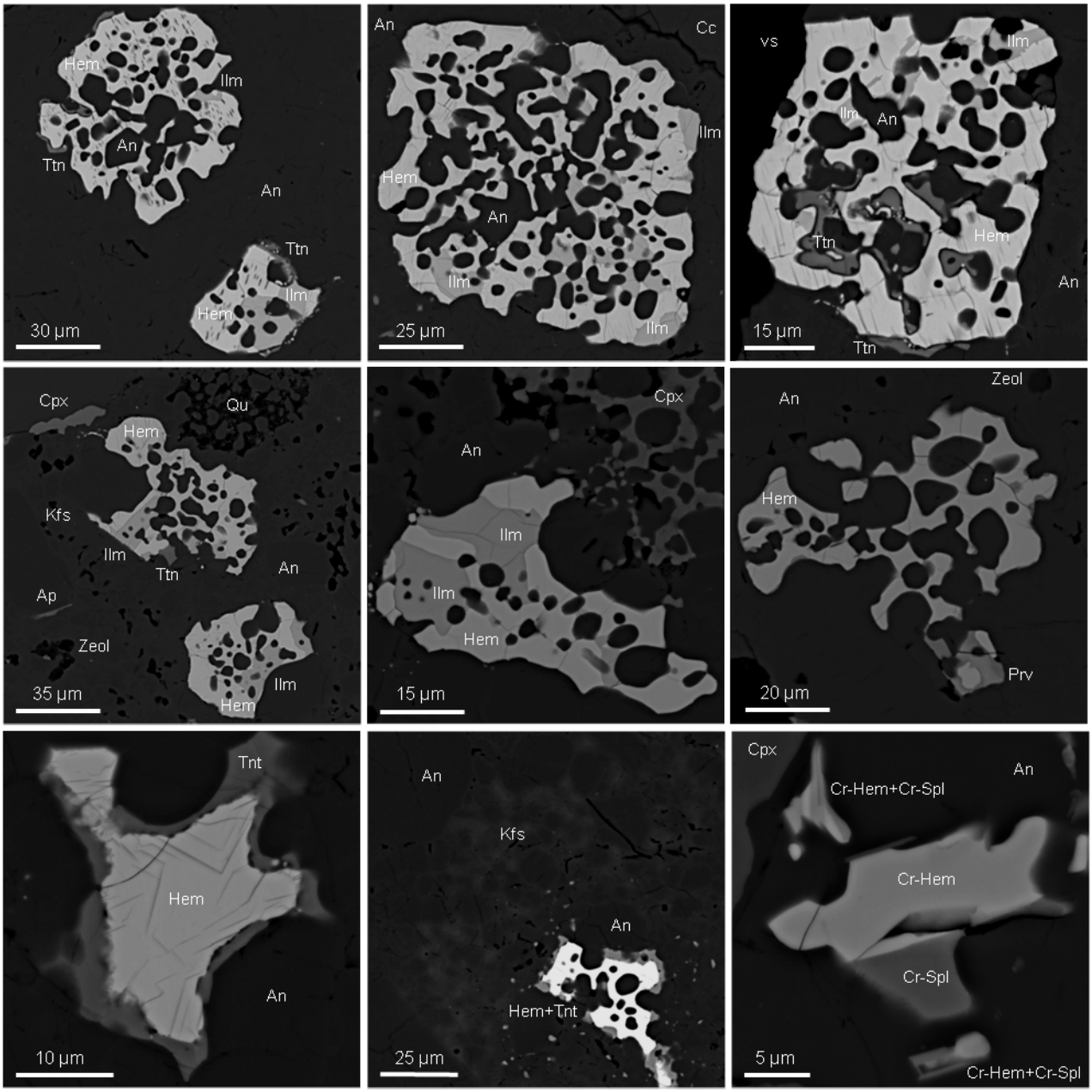


Fig. S4. Opaque minerals in leucocratic zone of plagioclase-clinopyroxene rock, Hatrurim Basin, BSE images.
Symbols: An – anorthite; Hem – hematite; Ilm – hemoilmenite; Tnt – titanite; Cc – calcite; vs – vesicle; Cpx - clinopyroxene; Ap – fluorapatite; Qu – $SiO_2$ polymorph; Zeol – a zeolite-supergroup mineral; Kfs – K-feldspar; Prv – perovskite; Cr-Hem-Cr-Spl – Cr-rich hematite and spinel.

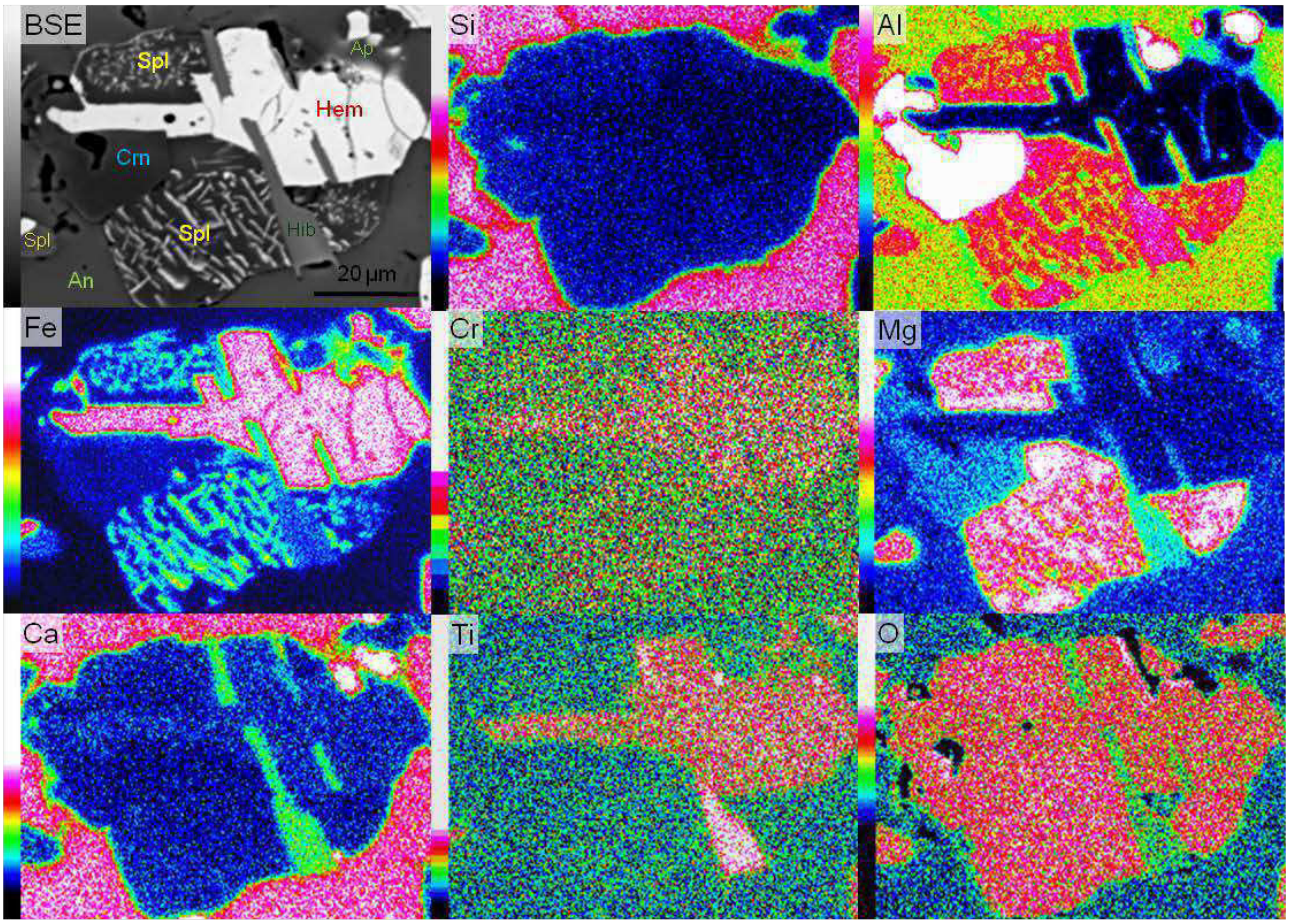
BSE
Spl
Ap
Hem
Crn
Spl
Spl
Hib
An
20 µm
Si
Al
Fe
Cr
Mg
Ca
Ti
O

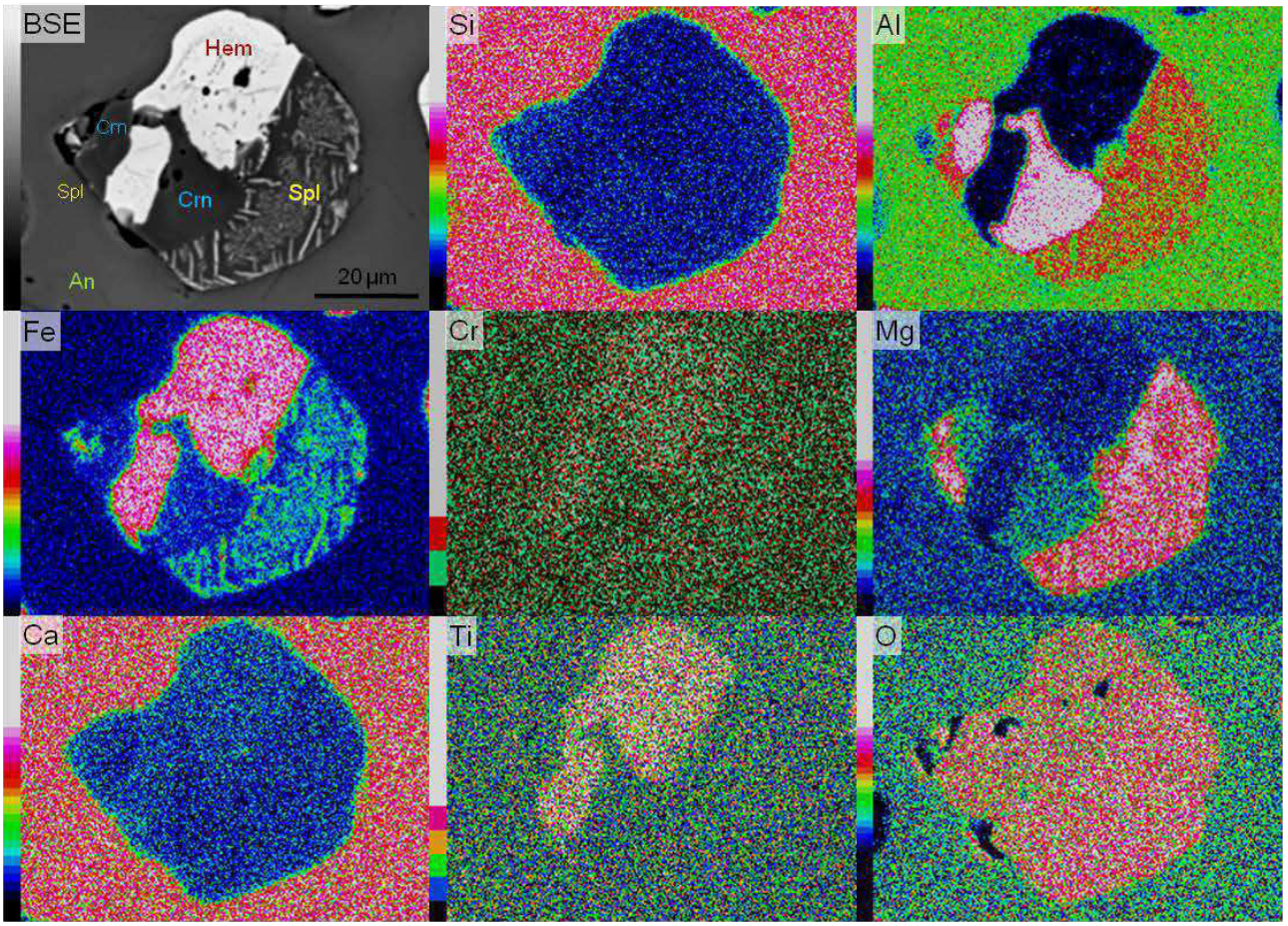
BSE
Hem
Crn
Spl
Crn
Spl
An
20 µm
Si
Al
Fe
Cr
Mg
Ca
Ti
O

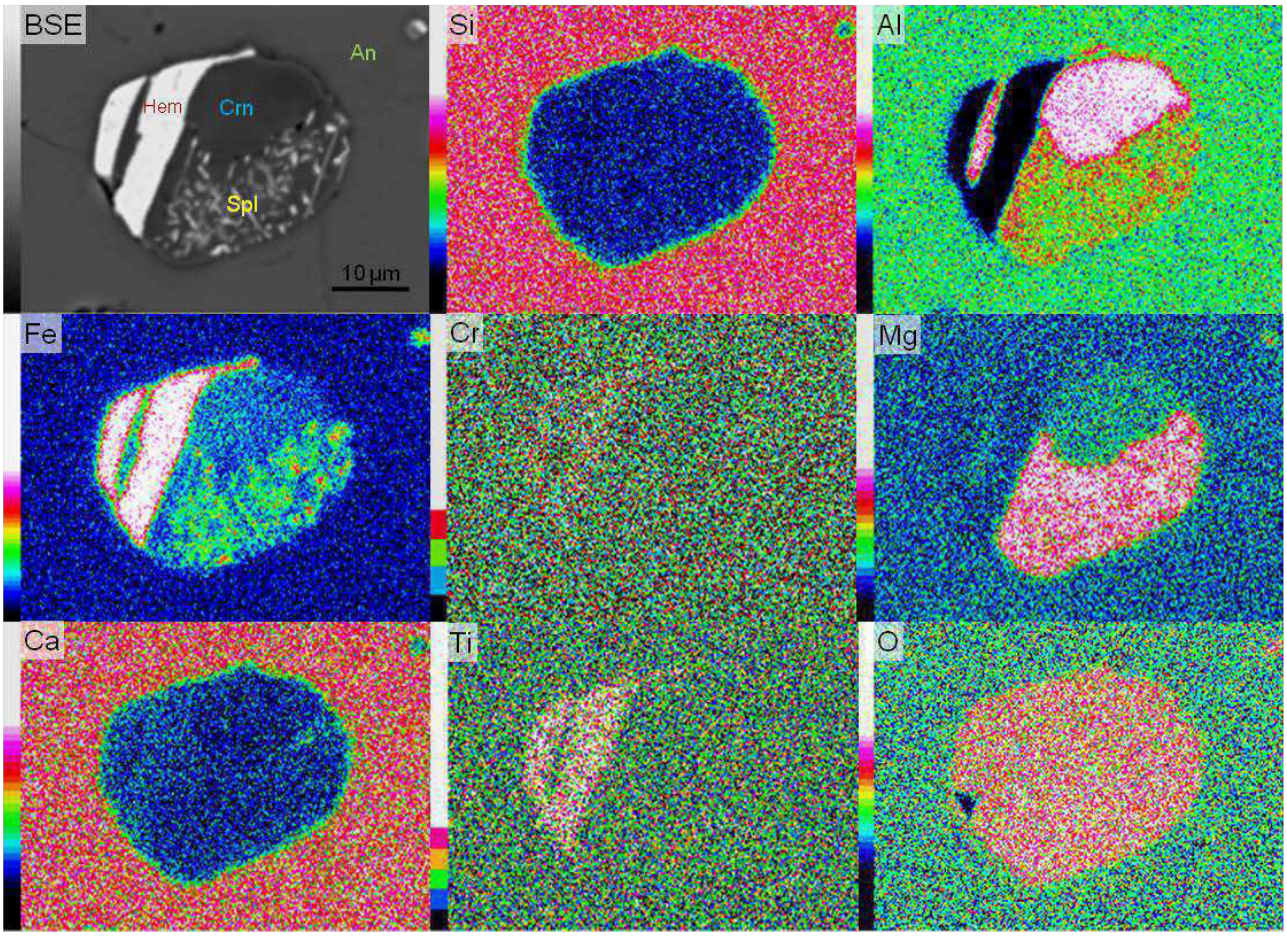
BSE
An
Hem
Crn
Spl
10 µm
Si
Al
Fe
Cr
Mg
Ca
Ti
O

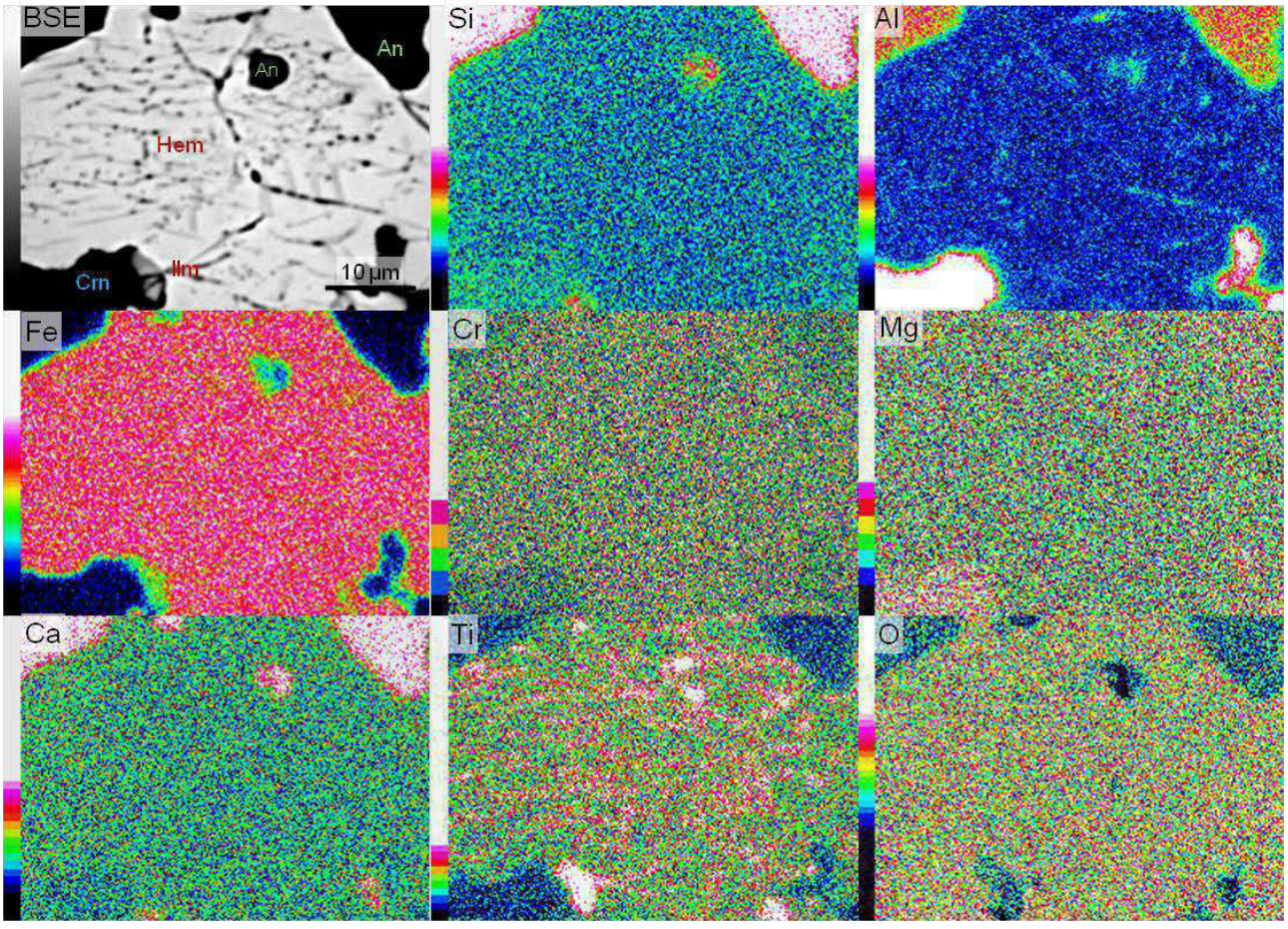
BSE
An
An
Hem
Crn
Ilm
10 µm
Si
Al
Fe
Cr
Mg
Ca
Ti
O

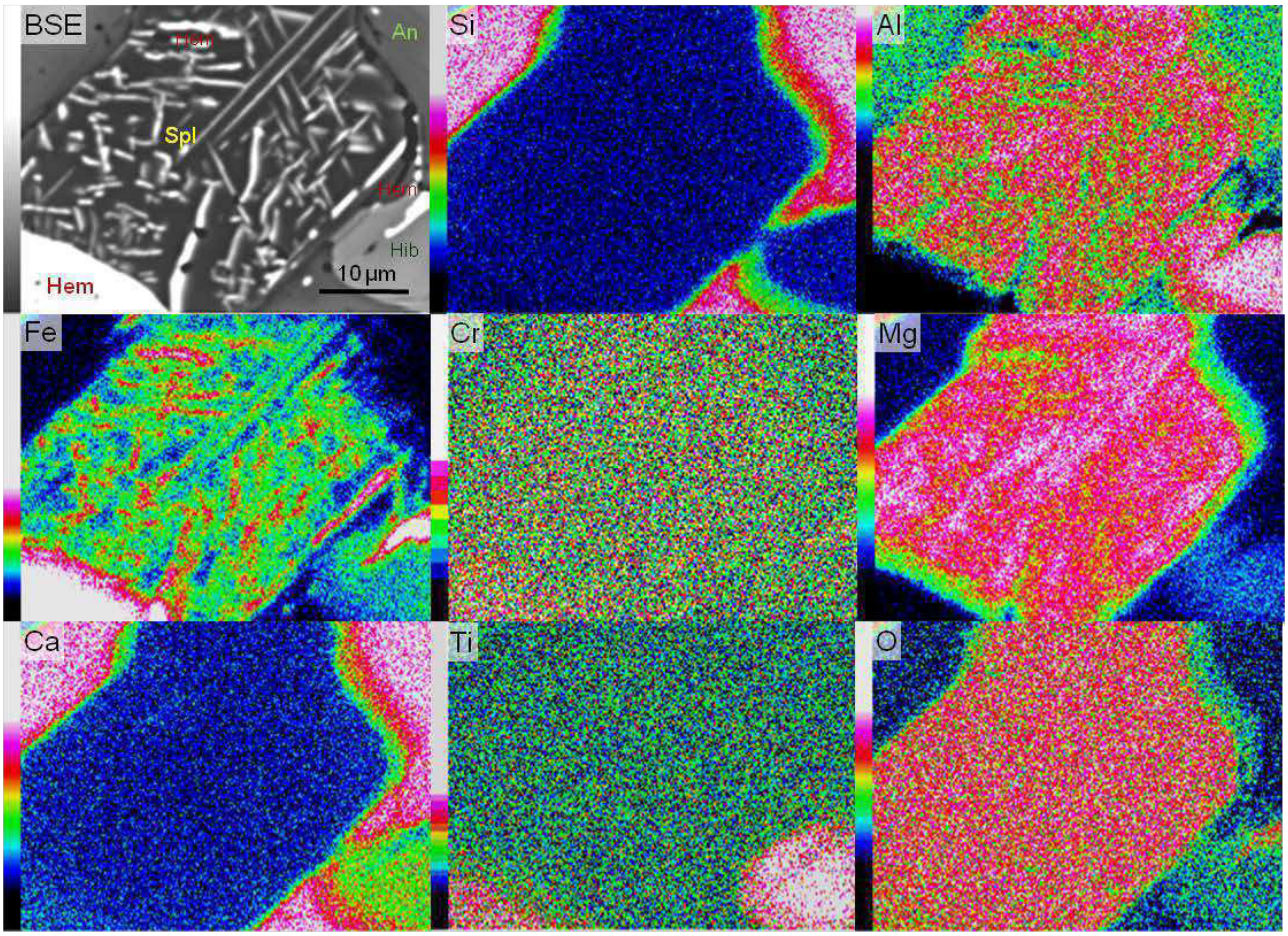
BSE
An
Spl
Hem
Hib
Hem
10 µm
Si
Al
Fe
Cr
Mg
Ca
Ti
O

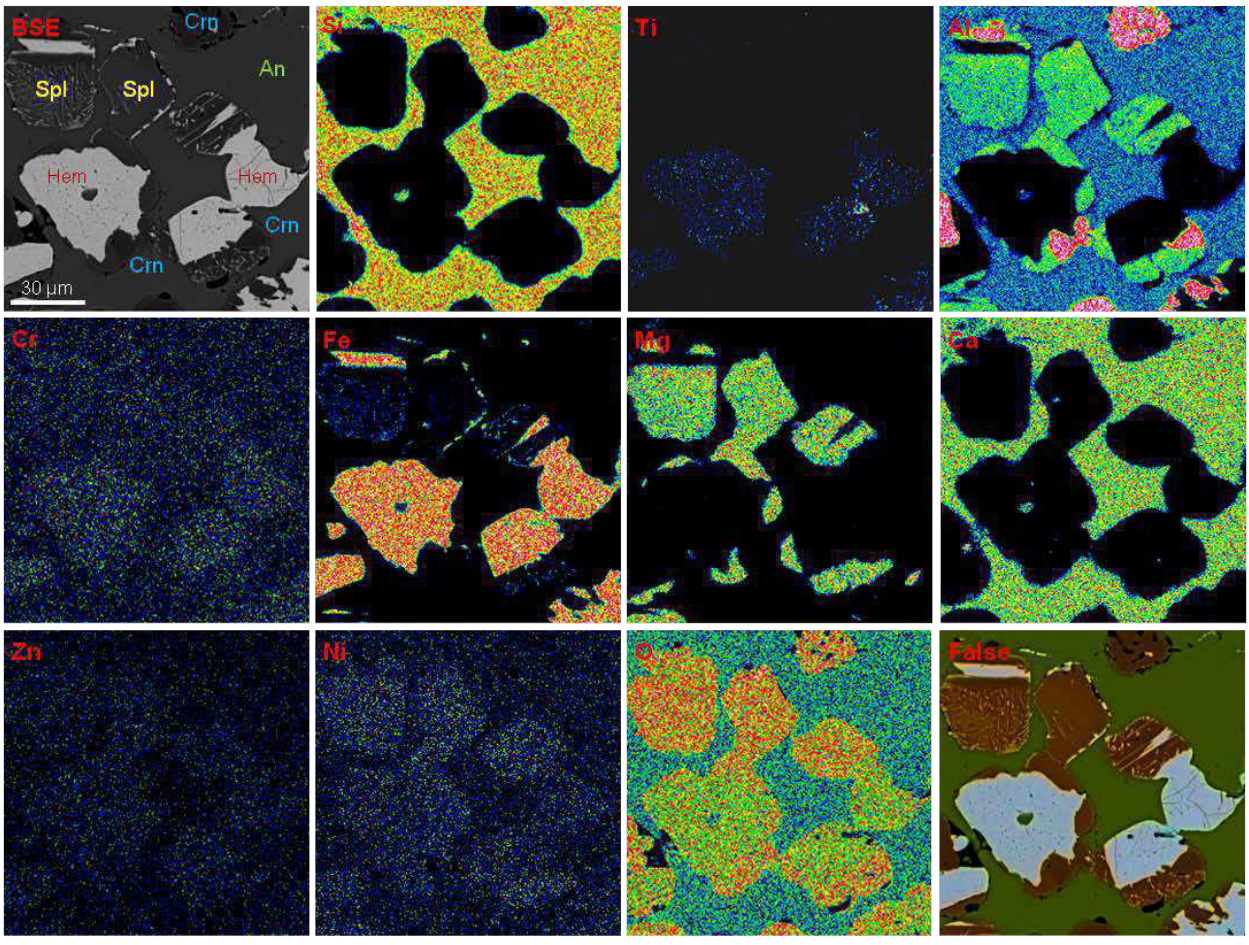
BSE
Crn
An
Spl
Spl
Hem
Hem
Crn
Crn
30 µm
Si
Ti
Al
Cr
Fe
Mg
Ca
Zn
Ni
O
False

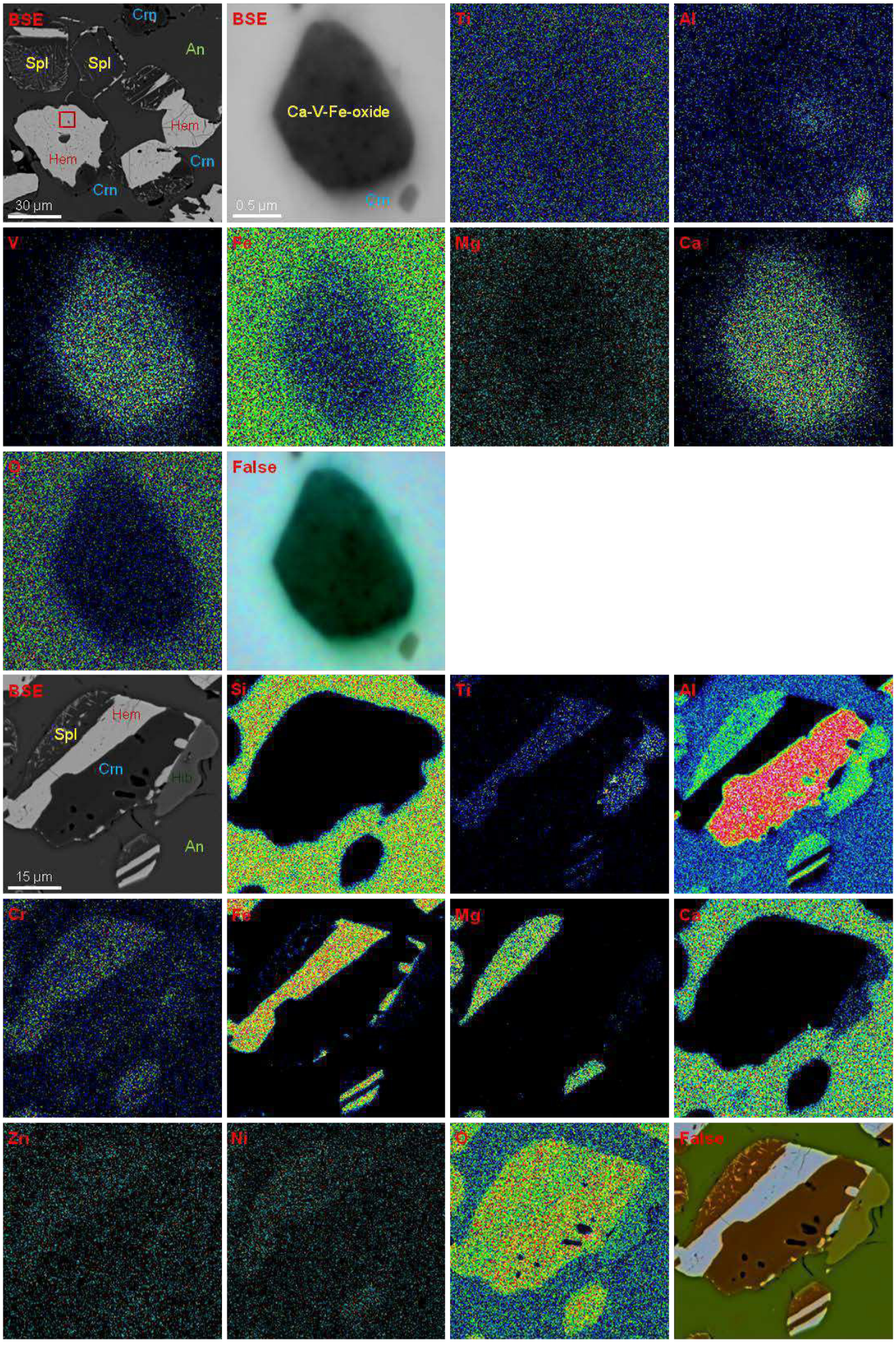
BSE
Crn
An
Spl
Spl
Hem
Hem
Crn
Crn
30 µm
BSE
Ca-V-Fe-oxide
0.5 µm
Crn
Ti
Al
V
Fe
Mg
Ca
O
False
BSE
Hem
Spl
Crn
Hb
An
15 µm
Si
Ti
Al
Cr
Fe
Mg
Ca
Zn
Ni
O
False

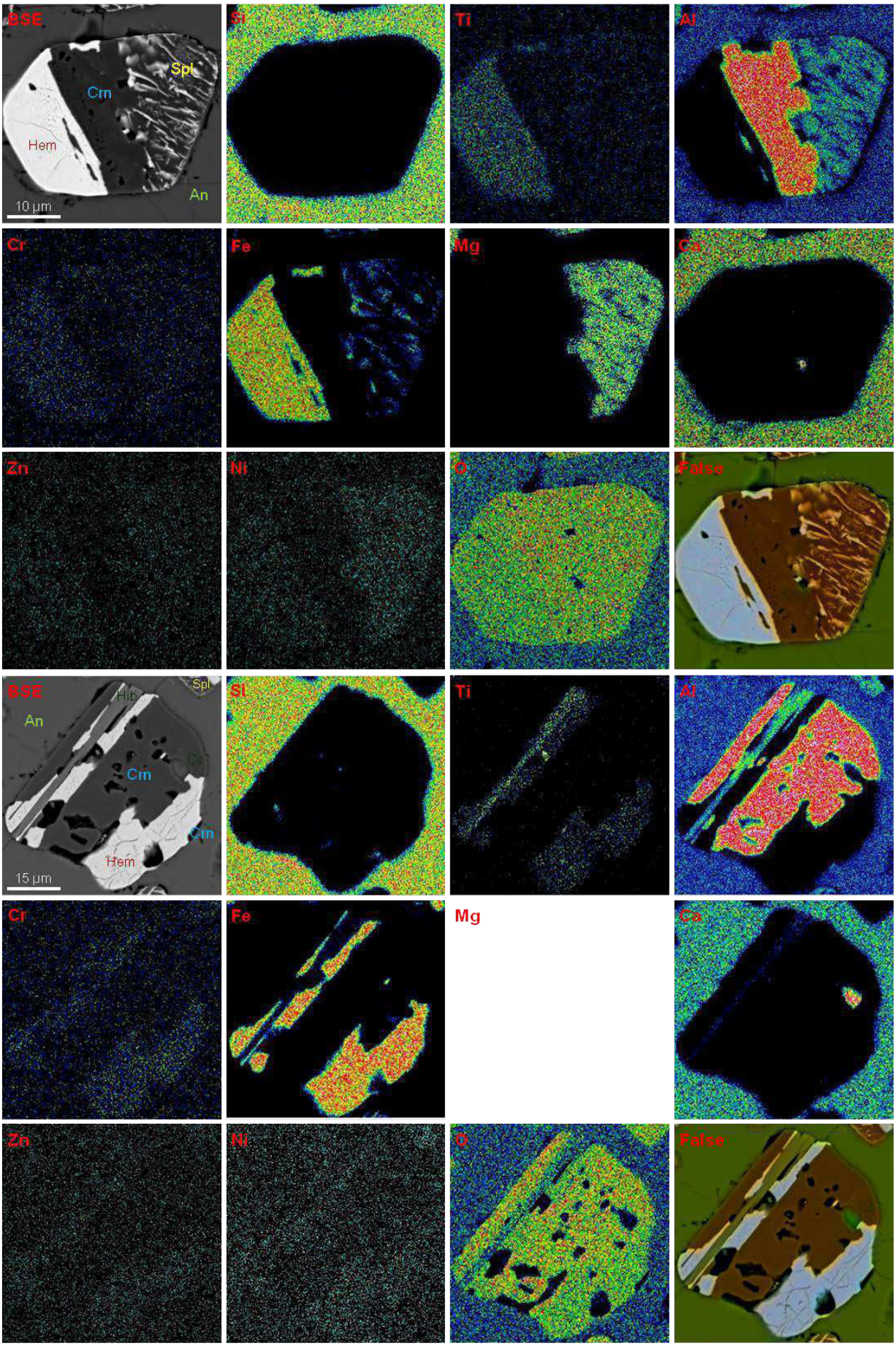


Fig. S5. BSE images and elemental maps for individual intergrowths in opaque isolation from host plagioclase-clinopyroxene rock, Hatrurim Basin, Israel.
Crn – corundum, Spl – spinel, Hem – hematite, Hib – hibonite, An – anorthite, Ap – fluorapatite, Ilm – ilmenite.

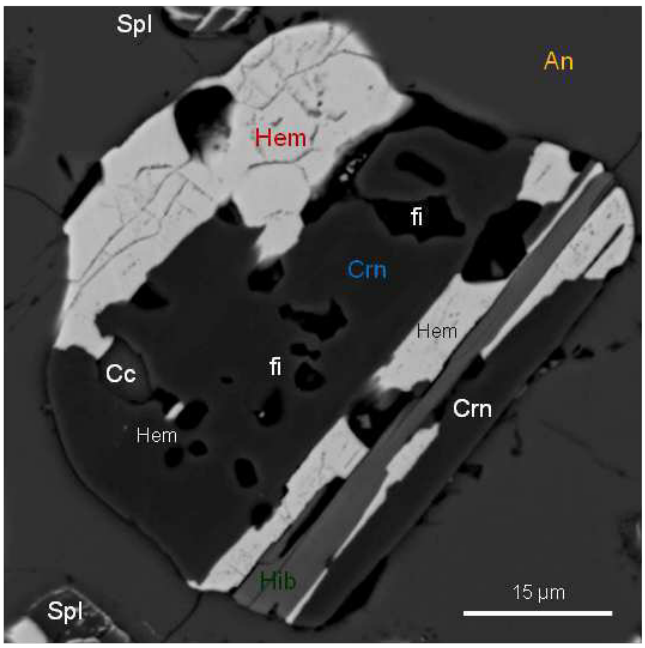


| Sample | iso-6 | |
|---|---|---|
| Phase | Crn | Hem |
| *n* | *2* | *2* |
| $TiO_2$ | 0.09 | 2.37 |
| $Cr_2O_3$ | 0.00 | 0.50 |
| $V_2O_3$ | | 0.35 |
| $Al_2O_3$ | 95.37 | 4.87 |
| $Fe_2O_3$ | 4.53 | 90.41 |
| FeO | 0.08 | 0.79 |
| MnO | 0.00 | 0.00 |
| MgO | 0.00 | 0.55 |
| CaO | | 0.28 |
| Sum | 100.06 | 100.11 |
| $XAl_2O_3$ | 0.97 | 0.09 |
| $XFe_2O_3$ | 0.03 | 0.91 |

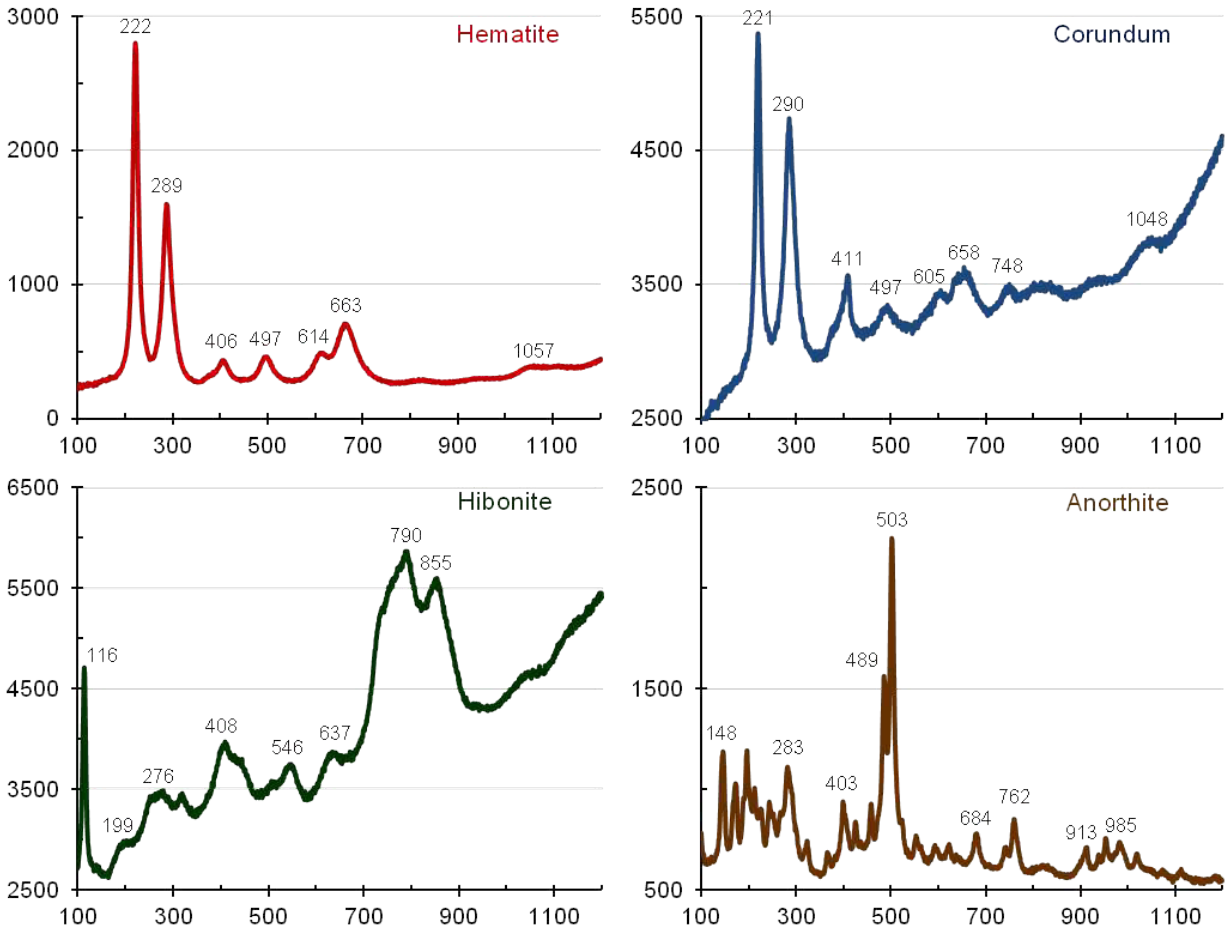


Fig. S6. Raman spectra for mineral intergrowth in anorthite from the opaque segregation, plagioclase-clinopyroxene rock, Hatrurim Basin (BSE image and chemical composition).
Symbols: Hem – hematite, Crn – corundum, Hib – hibonite, Cc – calcite, Spl – spinel, An – anorthite; fi – fluid inclusions in corundum.

Table S1. Chemical composition (EDS+WDS, wt.%) of principal minerals in host plagioclase-clinopyroxene rock, Hatrurim Basin, Israel.

| | $SiO_2$ | $TiO_2$ | $Cr_2O_3$ | $V_2O_3$ | $Al_2O_3$ | FeO | MnO | MgO | CaO | SrO | BaO | $Na_2O$ | $K_2O$ | $P_2O_5$ | $SO_3$ | F | Cl | Sum |
|---|---|---|---|---|---|---|---|---|---|---|---|---|---|---|---|---|---|---|
| **Anorthite** | | | | | | | | | | | | | | | | | | |
| | 42.96 | n.a. | n.a. | n.a. | 35.54 | 0.55 | n.a. | n.a. | 19.50 | n.a. | n.a. | 0.26 | 0.00 | n.a. | n.a. | n.a. | n.a. | 98.81 |
| | 44.03 | n.a. | n.a. | n.a. | 35.69 | 0.64 | n.a. | n.a. | 19.42 | n.a. | n.a. | 0.39 | 0.10 | n.a. | n.a. | n.a. | n.a. | 100.27 |
| | 43.51 | n.a. | n.a. | n.a. | 35.09 | 1.34 | n.a. | n.a. | 19.28 | n.a. | n.a. | 0.23 | 0.00 | n.a. | n.a. | n.a. | n.a. | 99.45 |
| | 45.44 | 0.00 | 0.00 | n.a. | 33.34 | 1.87 | 0.00 | 0.00 | 18.37 | 0.00 | 0.00 | 0.71 | 0.24 | n.a. | n.a. | n.a. | n.a. | 99.97 |
| **Clinopyroxene** | | | | | | | | | | | | | | | | | | |
| c | 43.73 | 1.68 | 0.00 | 0.00 | 8.84 | 12.68 | 0.00 | 8.71 | 23.87 | n.a. | n.a. | 0.00 | n.a. | n.a. | n.a. | n.a. | n.a. | 99.51 |
| r | 40.22 | 2.89 | 0.00 | 0.00 | 11.03 | 16.93 | 0.00 | 4.93 | 23.06 | n.a. | n.a. | 0.00 | n.a. | n.a. | n.a. | n.a. | n.a. | 99.06 |
| c | 44.88 | 1.25 | 0.47 | 0.00 | 7.84 | 11.93 | 0.00 | 9.04 | 23.49 | n.a. | n.a. | 0.19 | n.a. | n.a. | n.a. | n.a. | n.a. | 99.09 |
| r | 41.85 | 1.72 | 0.00 | 0.00 | 8.26 | 17.55 | 0.19 | 6.52 | 23.25 | n.a. | n.a. | 0.27 | n.a. | n.a. | n.a. | n.a. | n.a. | 99.61 |
| c | 46.38 | 0.82 | 0.38 | 0.25 | 7.33 | 9.92 | 0.00 | 9.88 | 24.11 | n.a. | n.a. | 0.00 | n.a. | n.a. | n.a. | n.a. | n.a. | 99.07 |
| r | 41.70 | 2.34 | 0.00 | 0.19 | 10.11 | 15.73 | 0.00 | 6.37 | 23.25 | n.a. | n.a. | 0.00 | n.a. | n.a. | n.a. | n.a. | n.a. | 99.69 |
| c | 46.68 | 1.27 | 0.18 | 0.00 | 7.44 | 9.94 | 0.00 | 10.07 | 23.77 | n.a. | n.a. | 0.18 | n.a. | n.a. | n.a. | n.a. | n.a. | 99.53 |
| c | 39.31 | 2.32 | 0.18 | | 10.11 | 18.29 | 0.12 | 5.92 | 23.05 | n.a. | n.a. | 0.19 | n.a. | n.a. | n.a. | n.a. | n.a. | 99.49 |
| c | 44.67 | 1.50 | 0.00 | 0.19 | 8.28 | 11.99 | 0.00 | 8.84 | 23.88 | n.a. | n.a. | 0.00 | n.a. | n.a. | n.a. | n.a. | n.a. | 99.35 |
| c | 41.76 | 2.35 | 0.00 | 0.22 | 8.33 | 17.37 | 0.00 | 5.67 | 23.30 | n.a. | n.a. | 0.19 | n.a. | n.a. | n.a. | n.a. | n.a. | 99.19 |
| **Fluorapatite** | | | | | | | | | | | | | | | | | | |
| | 6.91 | n.a. | n.a. | 0.00 | 0.55 | 0.67 | n.a. | n.a. | 52.02 | 1.89 | 0.44 | 0.00 | n.a. | 37.10 | 0.00 | 2.33 | n.a. | 101.91 |
| | 6.10 | n.a. | n.a. | 0.26 | 1.32 | 0.48 | n.a. | 0.30 | 51.36 | 1.65 | 0.45 | 0.00 | n.a. | 35.78 | 1.15 | 1.00 | 0.15 | 100.00 |
| | 6.14 | n.a. | n.a. | 0.00 | 1.10 | 0.42 | n.a. | 0.22 | 51.21 | 1.60 | n.a. | 0.00 | n.a. | 36.24 | 1.00 | 1.49 | 0.11 | 99.53 |
| | 6.89 | n.a. | n.a. | 0.00 | 1.10 | 0.42 | n.a. | 0.27 | 51.25 | 1.70 | n.a. | 0.00 | n.a. | 36.74 | 0.97 | 1.00 | 0.12 | 100.46 |
| | 5.61 | n.a. | n.a. | 0.00 | 0.94 | 0.36 | 0.00 | 0.00 | 52.08 | 1.84 | n.a. | 0.00 | n.a. | 38.08 | 0.00 | 1.50 | 0.00 | 100.41 |
| | 6.89 | n.a. | n.a. | 0.19 | 1.04 | 0.33 | n.a. | 0.27 | 51.90 | 1.66 | n.a. | 0.00 | n.a. | 35.97 | 1.15 | 0.77 | 0.14 | 100.31 |
| | 6.72 | n.a. | n.a. | 0.00 | 0.79 | 0.55 | n.a. | 0.25 | 52.46 | 1.68 | n.a. | 0.00 | n.a. | 35.75 | 1.02 | 1.11 | 0.10 | 100.43 |
| | 5.65 | n.a. | n.a. | 0.00 | 0.30 | 0.29 | n.a. | 0.27 | 51.47 | 1.75 | 0.36 | 0.00 | n.a. | 38.04 | 0.00 | 3.08 | n.a. | 101.21 |
| | 4.60 | n.a. | n.a. | 0.00 | 0.49 | 0.58 | n.a. | n.a. | 51.84 | 1.84 | n.a. | 0.00 | n.a. | 40.03 | 0.00 | 3.29 | n.a. | 102.67 |
| | 5.01 | n.a. | n.a. | 0.00 | 0.40 | 0.84 | n.a. | n.a. | 51.42 | 1.99 | n.a. | 0.00 | n.a. | 39.60 | 0.00 | 3.57 | n.a. | 102.83 |
| | 4.06 | n.a. | n.a. | 0.00 | 0.66 | 0.30 | n.a. | n.a. | 52.12 | 1.89 | n.a. | 0.00 | n.a. | 39.61 | 0.00 | 3.60 | n.a. | 102.24 |
| **Andradite** | | | | | | | | | | | | | | | | | | |
| c | 32.97 | 4.65 | 0.00 | 0.00 | 3.68 | 23.16 | 0.00 | 0.70 | 31.58 | n.a. | n.a. | 0.00 | n.a. | n.a. | n.a. | n.a. | n.a. | 96.74 |
| m | 32.95 | 4.34 | 0.00 | 0.22 | 3.97 | 22.27 | 0.22 | 0.78 | 31.65 | n.a. | n.a. | 0.00 | n.a. | n.a. | n.a. | n.a. | n.a. | 96.40 |
| r | 31.77 | 6.22 | 0.19 | 0.24 | 3.51 | 23.22 | 0.00 | 0.83 | 31.50 | n.a. | n.a. | 0.00 | n.a. | n.a. | n.a. | n.a. | n.a. | 97.48 |
| **"Hyalophane"** | | | | | | | | | | | | | | | | | | |
| | 42.02 | n.a. | n.a. | n.a. | 26.38 | 0.44 | n.a. | 0.00 | 2.38 | n.a. | 24.43 | 0.00 | 4.37 | n.a. | n.a. | n.a. | n.a. | 100.02 |
| | 41.80 | n.a. | n.a. | n.a. | 26.23 | 0.51 | n.a. | 0.00 | 2.78 | n.a. | 25.17 | 0.20 | 3.81 | n.a. | n.a. | n.a. | n.a. | 100.50 |
| | 42.68 | n.a. | n.a. | n.a. | 24.63 | 0.36 | n.a. | 0.00 | 0.99 | n.a. | 26.22 | 0.30 | 4.70 | n.a. | n.a. | n.a. | n.a. | 99.88 |
| | 42.10 | n.a. | n.a. | n.a. | 24.78 | 0.46 | n.a. | 0.00 | 1.04 | n.a. | 26.52 | 0.28 | 4.35 | n.a. | n.a. | n.a. | n.a. | 99.53 |
| | 42.72 | n.a. | n.a. | n.a. | 24.70 | 0.46 | n.a. | 0.00 | 0.92 | n.a. | 26.16 | 0.35 | 4.72 | n.a. | n.a. | n.a. | n.a. | 100.03 |
| | 38.19 | n.a. | n.a. | n.a. | 24.85 | 0.23 | n.a. | 0.00 | 1.37 | n.a. | 30.47 | 0.00 | 3.14 | n.a. | n.a. | n.a. | n.a. | 98.25 |

c, m, r – core, middle and rim of grain, n.a. – not analysed.

Table S2. Chemical composition (EDS+WDS, wt.%) of silicates in leucocratic zone and opaque segregation of plagioclase-clinopyroxene rock, Hatrurim Basin, Israel.

| | $SiO_2$ | $TiO_2$ | $Cr_2O_3$ | $V_2O_3$ | $Al_2O_3$ | FeO | MnO | MgO | CaO | $Ce_2O_3$ | SrO | BaO | $Na_2O$ | $K_2O$ | $P_2O_5$ | $SO_3$ | F | Cl | Sum |
|---|---|---|---|---|---|---|---|---|---|---|---|---|---|---|---|---|---|---|---|
| ***Leucocratic zone*** | | | | | | | | | | | | | | | | | | | |
| **Anorthite** | | | | | | | | | | | | | | | | | | | |
| | 43.83 | 0.00 | 0.00 | n.a. | 34.82 | 0.85 | 0.00 | 0.00 | 19.99 | n.a. | n.a. | 0.00 | 0.15 | 0.03 | n.a. | n.a. | n.a. | n.a. | 99.68 |
| | 43.90 | 0.00 | 0.00 | n.a. | 35.36 | 0.61 | 0.00 | 0.00 | 19.80 | n.a. | n.a. | 0.00 | 0.17 | 0.00 | n.a. | n.a. | n.a. | n.a. | 99.83 |
| | 43.41 | n.a. | n.a. | n.a. | 35.64 | 0.63 | n.a. | n.a. | 19.43 | n.a. | n.a. | n.a. | 0.44 | 0.11 | n.a. | n.a. | n.a. | n.a. | 99.66 |
| | 43.22 | n.a. | n.a. | n.a. | 35.79 | 0.41 | n.a. | n.a. | 19.46 | n.a. | n.a. | n.a. | 0.27 | 0.00 | n.a. | n.a. | n.a. | n.a. | 99.15 |
| | 44.07 | n.a. | n.a. | n.a. | 35.77 | 0.68 | n.a. | n.a. | 19.35 | n.a. | n.a. | n.a. | 0.38 | 0.00 | n.a. | n.a. | n.a. | n.a. | 100.25 |
| | 43.39 | n.a. | n.a. | n.a. | 34.82 | 1.12 | n.a. | n.a. | 19.11 | n.a. | n.a. | n.a. | 0.26 | 0.12 | n.a. | n.a. | n.a. | n.a. | 98.82 |
| | 43.59 | n.a. | n.a. | n.a. | 35.09 | 0.86 | 0.00 | n.a. | 19.31 | n.a. | n.a. | n.a. | 0.30 | 0.00 | n.a. | n.a. | n.a. | n.a. | 99.15 |
| | 43.60 | n.a. | n.a. | n.a. | 35.48 | 0.81 | n.a. | n.a. | 19.09 | n.a. | n.a. | n.a. | 0.32 | 0.00 | n.a. | n.a. | n.a. | n.a. | 99.30 |
| | 44.11 | n.a. | n.a. | n.a. | 35.81 | 0.69 | n.a. | n.a. | 19.23 | n.a. | n.a. | n.a. | 0.35 | 0.00 | n.a. | n.a. | n.a. | n.a. | 100.19 |
| | 43.54 | n.a. | n.a. | n.a. | 35.58 | 0.49 | n.a. | n.a. | 19.57 | n.a. | n.a. | n.a. | 0.23 | 0.00 | n.a. | n.a. | n.a. | n.a. | 99.41 |
| | 43.62 | n.a. | n.a. | n.a. | 35.43 | 0.89 | n.a. | n.a. | 19.85 | n.a. | n.a. | n.a. | 0.24 | 0.00 | n.a. | n.a. | n.a. | n.a. | 100.03 |
| | 43.75 | n.a. | n.a. | n.a. | 34.37 | 1.08 | n.a. | n.a. | 19.82 | n.a. | n.a. | n.a. | 0.51 | 0.18 | n.a. | n.a. | n.a. | n.a. | 99.71 |
| | 43.69 | n.a. | n.a. | n.a. | 36.05 | 0.78 | n.a. | n.a. | 19.63 | n.a. | n.a. | n.a. | 0.13 | 0.00 | n.a. | n.a. | n.a. | n.a. | 100.28 |
| | 43.73 | n.a. | n.a. | n.a. | 35.96 | 0.58 | n.a. | n.a. | 19.52 | n.a. | n.a. | n.a. | 0.30 | 0.00 | n.a. | n.a. | n.a. | n.a. | 100.09 |
| | 43.79 | n.a. | n.a. | n.a. | 35.54 | 0.76 | n.a. | n.a. | 19.42 | n.a. | n.a. | 0.00 | 0.32 | 0.00 | n.a. | n.a. | n.a. | n.a. | 99.83 |
| **K-feldspar** | | | | | | | | | | | | | | | | | | | |
| | 57.29 | n.a. | n.a. | n.a. | 23.27 | 0.77 | n.a. | 0.00 | 6.06 | n.a. | 0.00 | 1.98 | 0.23 | 10.67 | n.a. | n.a. | n.a. | n.a. | 100.27 |
| | 57.29 | n.a. | n.a. | n.a. | 22.47 | 1.18 | n.a. | n.a. | 5.54 | n.a. | n.a. | 2.47 | 0.43 | 10.71 | n.a. | n.a. | n.a. | n.a. | 100.09 |
| **Clinopyroxene** | | | | | | | | | | | | | | | | | | | |
| | 44.54 | 1.40 | 0.43 | n.a. | 8.60 | 11.26 | 0.03 | 9.76 | 24.17 | n.a. | n.a. | n.a. | 0.07 | n.a. | n.a. | n.a. | n.a. | n.a. | 100.26 |
| | 44.23 | 1.45 | 0.54 | n.a. | 8.40 | 11.04 | 0.04 | 9.66 | 23.90 | n.a. | n.a. | n.a. | 0.07 | n.a. | n.a. | n.a. | n.a. | n.a. | 99.33 |
| | 45.18 | 1.42 | 0.07 | n.a. | 8.02 | 10.58 | 0.02 | 9.84 | 24.54 | n.a. | n.a. | n.a. | 0.07 | n.a. | n.a. | n.a. | n.a. | n.a. | 99.74 |
| | 42.36 | 1.37 | 0.60 | n.a. | 10.39 | 12.02 | 0.00 | 8.19 | 23.32 | n.a. | n.a. | n.a. | 0.00 | n.a. | n.a. | n.a. | n.a. | n.a. | 98.25 |
| | 44.72 | 1.17 | 0.32 | 0.00 | 8.60 | 10.58 | 0.00 | 9.78 | 23.58 | n.a. | n.a. | n.a. | 0.00 | n.a. | n.a. | n.a. | n.a. | n.a. | 98.75 |
| | 42.69 | 0.88 | 0.00 | 0.18 | 6.46 | 18.35 | 0.23 | 7.68 | 23.33 | n.a. | n.a. | n.a. | 0.35 | n.a. | n.a. | n.a. | n.a. | n.a. | 100.15 |
| | 42.68 | 2.05 | 0.00 | 0.00 | 9.22 | 13.29 | 0.17 | 7.60 | 23.68 | n.a. | n.a. | n.a. | 0.35 | n.a. | n.a. | n.a. | n.a. | n.a. | 99.04 |
| | 41.68 | 2.20 | 0.00 | 0.18 | 10.00 | 14.24 | 0.00 | 7.08 | 23.42 | n.a. | n.a. | n.a. | 0.49 | n.a. | n.a. | n.a. | n.a. | n.a. | 99.29 |
| | 43.58 | 1.98 | 0.00 | 0.00 | 8.94 | 12.12 | 0.00 | 8.11 | 23.60 | n.a. | n.a. | n.a. | 0.26 | n.a. | n.a. | n.a. | n.a. | n.a. | 98.59 |
| | 43.47 | 1.20 | 0.50 | 0.00 | 8.45 | 12.35 | n.a. | 9.02 | 23.18 | n.a. | n.a. | n.a. | 0.27 | n.a. | n.a. | n.a. | n.a. | n.a. | 98.44 |
| **Fluorapatite** | | | | | | | | | | | | | | | | | | | |
| | 2.63 | n.a. | n.a. | 2.29 | n.a. | 0.00 | 0.00 | n.a. | 53.13 | 0.00 | 1.64 | n.a. | 0.00 | n.a. | 37.62 | 0.42 | 3.53 | 0.00 | 101.26 |
| | 6.27 | n.a. | n.a. | 0.22 | 0.17 | 0.54 | 0.00 | n.a. | 52.21 | 0.00 | 1.86 | n.a. | 0.00 | n.a. | 37.83 | 0.00 | 1.71 | 0.00 | 100.81 |
| | 5.50 | n.a. | n.a. | 0.00 | 0.36 | 0.44 | 0.00 | 0.00 | 52.11 | 0.00 | 1.81 | 0.00 | 0.24 | n.a. | 38.31 | 0.00 | 2.05 | 0.00 | 100.82 |
| | 5.69 | n.a. | n.a. | 0.00 | 0.28 | 0.49 | 0.00 | 0.00 | 52.01 | 0.00 | 1.64 | 0.35 | 0.00 | n.a. | 37.83 | 0.00 | 2.52 | 0.00 | 100.81 |
| | 3.79 | n.a. | n.a. | 0.78 | n.a. | 0.41 | n.a. | n.a. | 53.72 | n.a. | 1.77 | n.a. | 0.00 | n.a. | 37.97 | 1.55 | 1.79 | 0.00 | 101.78 |
| | 4.98 | n.a. | n.a. | 0.00 | 0.00 | 0.57 | n.a. | n.a. | 51.53 | n.a. | 1.87 | n.a. | 0.00 | n.a. | 38.66 | 0.00 | 2.49 | 0.00 | 100.10 |
| **c** | 6.65 | n.a. | n.a. | 0.00 | 0.31 | 0.75 | n.a. | n.a. | 52.34 | 0.42 | 1.82 | 0.00 | 0.00 | n.a. | 37.69 | 0.00 | 1.61 | 0.00 | 101.58 |
| **r** | 3.63 | n.a. | n.a. | 0.62 | 0.00 | 0.37 | n.a. | n.a. | 53.50 | 0.00 | 1.77 | 0.00 | 0.00 | n.a. | 38.08 | 1.66 | 2.43 | 0.00 | 102.05 |
| ***Opaque segregation*** | | | | | | | | | | | | | | | | | | | |
| **Anorthite** | | | | | | | | | | | | | | | | | | | |
| | 44.47 | 0.00 | 0.00 | n.a. | 34.32 | 0.58 | 0.00 | 0.00 | 19.61 | n.a. | n.a. | 0.00 | 0.28 | 0.18 | n.a. | n.a. | n.a. | n.a. | 99.44 |
| | 44.37 | 0.00 | 0.00 | n.a. | 34.90 | 0.53 | 0.00 | 0.00 | 19.76 | n.a. | n.a. | 0.00 | 0.26 | 0.04 | n.a. | n.a. | n.a. | n.a. | 99.87 |
| | 44.19 | 0.00 | 0.00 | n.a. | 34.78 | 0.59 | 0.00 | 0.00 | 19.81 | n.a. | n.a. | 0.00 | 0.18 | 0.07 | n.a. | n.a. | n.a. | n.a. | 99.62 |
| | 44.11 | n.a. | n.a. | n.a. | 35.45 | 0.48 | n.a. | n.a. | 19.45 | n.a. | n.a. | n.a. | 0.00 | 0.00 | n.a. | n.a. | n.a. | n.a. | 99.49 |
| | 44.27 | n.a. | n.a. | n.a. | 34.99 | 0.44 | n.a. | n.a. | 19.70 | n.a. | n.a. | n.a. | 0.00 | 0.00 | n.a. | n.a. | n.a. | n.a. | 99.40 |
| | 44.09 | n.a. | n.a. | n.a. | 35.30 | 0.68 | n.a. | n.a. | 19.69 | n.a. | n.a. | n.a. | 0.00 | 0.00 | n.a. | n.a. | n.a. | n.a. | 99.76 |
| | 44.01 | n.a. | n.a. | n.a. | 35.54 | 0.73 | n.a. | n.a. | 19.66 | n.a. | n.a. | n.a. | 0.15 | 0.11 | n.a. | n.a. | n.a. | n.a. | 100.20 |
| | 43.66 | n.a. | n.a. | n.a. | 35.82 | 0.95 | n.a. | n.a. | 19.46 | n.a. | n.a. | n.a. | n.a. | 0.25 | n.a. | n.a. | n.a. | n.a. | 100.14 |
| | 44.02 | n.a. | n.a. | n.a. | 35.63 | 0.57 | n.a. | n.a. | 19.90 | n.a. | n.a. | n.a. | 0.16 | 0.00 | n.a. | n.a. | n.a. | n.a. | 100.28 |
| | 43.95 | n.a. | n.a. | n.a. | 35.79 | 0.49 | n.a. | n.a. | 19.39 | n.a. | n.a. | n.a. | 0.26 | 0.00 | n.a. | n.a. | n.a. | n.a. | 99.88 |
| **K+feldspar** | | | | | | | | | | | | | | | | | | | |
| | 63.65 | 0.00 | n.a. | n.a. | 17.63 | 0.78 | n.a. | 0.00 | 1.13 | n.a. | n.a. | n.a. | 0.00 | 16.18 | n.a. | n.a. | n.a. | n.a. | 99.37 |
| **Clinopyroxene** | | | | | | | | | | | | | | | | | | | |
| | 42.80 | 2.35 | 0.69 | n.a. | 9.22 | 13.12 | 0.03 | 7.83 | 23.58 | n.a. | n.a. | 0.00 | 0.15 | 0.00 | n.a. | n.a. | n.a. | n.a. | 99.78 |
| | 42.95 | 1.63 | 0.64 | n.a. | 9.57 | 11.68 | 0.00 | 8.61 | 23.70 | n.a. | n.a. | n.a. | 0.00 | n.a. | n.a. | n.a. | n.a. | n.a. | 98.78 |
| | 42.72 | 1.52 | 0.60 | n.a. | 9.43 | 11.99 | 0.00 | 8.82 | 23.66 | n.a. | n.a. | n.a. | 0.00 | n.a. | n.a. | n.a. | n.a. | n.a. | 98.74 |
| | 42.44 | 1.67 | 0.67 | n.a. | 9.66 | 12.36 | 0.00 | 8.14 | 23.80 | n.a. | n.a. | n.a. | 0.00 | n.a. | n.a. | n.a. | n.a. | n.a. | 98.74 |

n.a. – not analysed.

Table S3. Chemical composition (EDS, wt.%) of opaque mineral associations in leucocratic zone and host plagioclase-clinopyroxene rock, Hatrurim Basin, Israel.

| | Phase | *n* | $SiO_2$ | $TiO_2$ | $Al_2O_3$ | $Cr_2O_3$ | $V_2O_3$ | FeO | MnO | MgO | CaO | NiO | ZnO | $Nb_2O_5$ | $Y_2O_3$ | $La_2O_3$ | $Ce_2O_3$ | Sum |
|---|---|---|---|---|---|---|---|---|---|---|---|---|---|---|---|---|---|---|
| **Leucocratic zone** | | | | | | | | | | | | | | | | | | |
| Lz-1 | Hem | *1* | n.a. | 3.72 | 2.10 | 0.00 | 0.00 | 84.90 | 0.31 | 0.71 | 0.35 | 0.00 | n.a. | n.a. | n.a. | n.a. | n.a. | 92.09 |
| | H-Ilm | *2* | n.a. | 35.35 | 3.91 | 0.00 | 0.00 | 53.38 | 0.22 | 0.75 | 0.48 | n.a. | n.a. | n.a. | n.a. | n.a. | n.a. | 94.07 |
| | Tnt | *1* | 29.72 | 35.06 | 4.36 | 0.00 | 0.00 | 5.38 | 0.00 | 0.00 | 24.88 | n.a. | n.a. | 0.00 | n.a. | n.a. | n.a. | 99.40 |
| Lz-2 | Hem | *4* | n.a. | 7.76 | 3.29 | 0.00 | 0.19 | 80.59 | 0.29 | 0.56 | 0.31 | 0.30 | n.a. | n.a. | n.a. | n.a. | n.a. | 93.27 |
| | H-Ilm | *1* | n.a. | 35.36 | 6.41 | 0.00 | 0.00 | 52.04 | 0.00 | 0.66 | 0.49 | 0.00 | n.a. | 0.00 | n.a. | n.a. | n.a. | 94.96 |
| | Tnt | *1* | 29.91 | 33.41 | 5.33 | 0.00 | 0.00 | 3.30 | 0.00 | 0.00 | 25.40 | n.a. | n.a. | 2.57 | n.a. | n.a. | n.a. | 99.92 |
| Lz-2 | Hem | *3* | n.a. | 7.85 | 3.31 | 0.00 | 0.00 | 80.23 | 0.26 | 0.52 | 0.32 | 0.11 | n.a. | n.a. | n.a. | n.a. | n.a. | 92.59 |
| | H-Ilm | *2* | n.a. | 36.22 | 4.52 | 0.00 | 0.17 | 52.96 | 0.00 | 0.48 | 0.32 | 0.00 | n.a. | n.a. | n.a. | n.a. | n.a. | 94.66 |
| Lz-3 | Hem | *2* | n.a. | 3.19 | 0.82 | 0.00 | 0.00 | 86.96 | 0.12 | 0.43 | 0.34 | 0.38 | n.a. | n.a. | n.a. | n.a. | n.a. | 92.22 |
| | Tnt | *1* | 29.84 | 37.13 | 1.51 | 0.00 | 0.00 | 4.43 | 0.00 | n.a. | 25.76 | n.a. | n.a. | 1.40 | n.a. | n.a. | n.a. | 100.07 |
| Iso-2-7 | Hem | *1* | n.a. | 7.36 | 2.40 | 0.00 | 0.00 | 79.36 | 0.00 | 0.90 | 0.28 | 0.00 | n.a. | n.a. | n.a. | n.a. | n.a. | 90.30 |
| c | Prv | *2* | 0.80 | 45.35 | 1.38 | 0.00 | 0.00 | 3.58 | 0.00 | 0.00 | 37.09 | 0.00 | n.a. | 9.23 | 0.33 | 0.50 | 0.75 | 98.99 |
| r | Prv | *2* | 0.29 | 55.00 | 1.32 | 0.00 | 0.50 | 2.08 | 0.00 | 0.10 | 38.01 | 0.00 | n.a. | 1.07 | 0.00 | 0.00 | 0.00 | 98.35 |
| Lz-x1 | Hem | *2* | 0.00 | 2.95 | 1.68 | 0.00 | 0.00 | 84.93 | 0.21 | 0.66 | 0.22 | 0.30 | n.a. | n.a. | n.a. | n.a. | n.a. | 90.94 |
| | H-Ilm | *1* | n.a. | 35.31 | 2.29 | 0.00 | 0.34 | 54.12 | 0.00 | 0.68 | 0.45 | 0.00 | n.a. | n.a. | n.a. | n.a. | n.a. | 93.19 |
| Lz-x2 | Hem | *3* | n.a. | 3.94 | 1.70 | 0.00 | 0.00 | 83.65 | 0.18 | 0.48 | 0.37 | 0.00 | n.a. | 0.00 | n.a. | n.a. | n.a. | 90.31 |
| | H-Ilm | *3* | n.a. | 35.16 | 2.46 | 0.00 | 0.25 | 53.88 | 0.00 | 0.59 | 0.45 | 0.00 | n.a. | 0.60 | n.a. | n.a. | n.a. | 93.39 |
| Lz-x7 | Hem | *2* | 0.00 | 3.47 | 2.87 | 0.00 | 0.00 | 82.63 | 0.00 | 1.03 | 0.45 | 0.00 | n.a. | 0.00 | n.a. | n.a. | n.a. | 90.44 |
| | H-Ilm | *2* | 0.00 | 35.93 | 4.49 | 0.00 | 0.64 | 51.22 | 0.00 | 1.14 | 0.29 | 0.00 | n.a. | 0.00 | n.a. | n.a. | n.a. | 93.70 |
| iso4-6 | Hem | *2* | 0.00 | 3.52 | 1.57 | 0.00 | 0.00 | 84.21 | 0.30 | 0.70 | 0.31 | 0.00 | n.a. | 0.00 | n.a. | n.a. | n.a. | 90.60 |
| | H-Ilm | *1* | n.a. | 34.94 | 2.83 | 0.00 | 0.37 | 53.49 | 0.19 | 0.46 | 0.48 | n.a. | n.a. | 0.43 | n.a. | n.a. | n.a. | 93.19 |
| | Tnt | *1* | 27.75 | 34.56 | 1.53 | 0.00 | 1.90 | 2.75 | 0.00 | n.a. | 26.58 | n.a. | n.a. | 3.13 | n.a. | n.a. | n.a. | 98.20 |
| iso4-6 | Hem | *1* | n.a. | 3.52 | 1.23 | 0.00 | 0.00 | 84.30 | 0.35 | 0.46 | 0.22 | n.a. | n.a. | n.a. | n.a. | n.a. | n.a. | 90.08 |
| | H-Ilm | *2* | 0.00 | 34.96 | 1.85 | 0.00 | 0.21 | 56.39 | 0.00 | 0.42 | 0.32 | 0.00 | n.a. | 0.00 | n.a. | n.a. | n.a. | 94.14 |
| iso-7 | Cr-Hem | *3* | 0.00 | 2.28 | 7.00 | 18.09 | 0.62 | 62.62 | 0.00 | 0.47 | 0.36 | 0.00 | 0.00 | n.a. | n.a. | n.a. | n.a. | 91.45 |
| | Cr-Spl | *1* | n.a. | 0.00 | 32.93 | 22.46 | 0.00 | 24.84 | 0.79 | 13.08 | 0.27 | 0.69 | 1.41 | n.a. | n.a. | n.a. | n.a. | 96.47 |
| **Host rock** | | | | | | | | | | | | | | | | | | |
| h-1-2 | Hem | *2* | 0.00 | 3.97 | 2.04 | 0.00 | 0.00 | 83.77 | 0.22 | 0.58 | 0.38 | 0.00 | n.a. | 0.00 | n.a. | n.a. | n.a. | 90.96 |
| | Tnt | *3* | 29.82 | 38.30 | 0.71 | 0.00 | 0.26 | 1.24 | 0.00 | 0.00 | 27.32 | 0.00 | n.a. | 1.40 | n.a. | n.a. | n.a. | 99.05 |
| h-2 | Hem | *4* | n.a. | 5.08 | 0.64 | 0.00 | 0.06 | 83.53 | 0.08 | 0.39 | 0.41 | 0.00 | n.a. | n.a. | n.a. | n.a. | n.a. | 90.18 |

See Fig. S3. *n* – average; n.a. – not analysed. Hem – hematite; H-Ilm – “hemoilmenite”; Tnt – titanite; Prv – perovskite; Cr-Hem – Cr-hematite; Cr-Spl – Cr-spinel; c, r – core-rim of grain.

Table S4. Chemical composition (EDS, wt.%) of vesicle-related minerals in plagioclase-clinopyroxene rock, Hatrurim Basin, Israel.

| Sample | Mineral | $SiO_2$ | $Al_2O_3$ | FeO | MnO | MgO | CaO | SrO | BaO | $Na_2O$ | $K_2O$ | $SO_3$ | Cl | Sum |
|---|---|---|---|---|---|---|---|---|---|---|---|---|---|---|
| iso-1-g4 | Calcite | n.a. | n.a. | 0.00 | 0.00 | 0.00 | 55.37 | 0.00 | n.a. | n.a. | n.a. | n.a. | n.a. | 55.37 |
| Iso-3 | Calcite | n.a. | n.a. | 0.00 | 0.00 | 0.00 | 55.83 | 0.00 | n.a. | n.a. | n.a. | n.a. | n.a. | 55.83 |
| | Quartz | 99.18 | n.a. | n.a. | n.a. | n.a. | 0.18 | n.a. | n.a. | n.a. | n.a. | n.a. | n.a. | 99.36 |
| | Quartz | 99.87 | n.a. | n.a. | n.a. | n.a. | 0.25 | n.a. | n.a. | n.a. | n.a. | n.a. | n.a. | 100.12 |
| Lz-4 | Calcite | n.a. | n.a. | n.a. | n.a. | n.a. | 54.44 | 0.00 | n.a. | n.a. | n.a. | 0.67 | n.a. | 55.11 |
| | Calcite | n.a. | n.a. | n.a. | n.a. | n.a. | 55.23 | 0.00 | n.a. | n.a. | n.a. | n.a. | n.a. | 55.23 |
| | Quartz | 99.89 | n.a. | n.a. | n.a. | n.a. | 0.55 | n.a. | n.a. | n.a. | n.a. | n.a. | n.a. | 100.44 |
| | Quartz | 100.10 | n.a. | n.a. | n.a. | n.a. | 0.50 | n.a. | n.a. | n.a. | n.a. | n.a. | n.a. | 100.60 |
| | Bassanite | n.a. | n.a. | 0.00 | n.a. | n.a. | 37.18 | 0.00 | n.a. | n.a. | n.a. | 55.56 | 0.37 | 93.11 |
| | Bassanite | n.a. | n.a. | 0.00 | n.a. | n.a. | 36.79 | 0.00 | n.a. | n.a. | n.a. | 54.76 | 0.36 | 91.91 |
| Iso-2-3-g | Calcite | n.a. | n.a. | 0.00 | 0.00 | 0.00 | 55.55 | 0.00 | n.a. | n.a. | n.a. | n.a. | n.a. | 55.55 |
| | Calcite | n.a. | n.a. | 0.00 | 0.00 | 0.00 | 55.43 | 0.00 | n.a. | n.a. | n.a. | n.a. | n.a. | 55.43 |
| | Calcite | n.a. | n.a. | 0.00 | 0.00 | 0.00 | 55.16 | 0.00 | n.a. | n.a. | n.a. | n.a. | n.a. | 55.16 |
| | Calcite | n.a. | n.a. | 0.00 | 0.00 | 0.00 | 55.59 | 0.00 | n.a. | n.a. | n.a. | n.a. | n.a. | 55.59 |
| | Quartz | 98.50 | 0.53 | n.a. | n.a. | n.a. | 0.42 | n.a. | n.a. | n.a. | 0.17 | n.a. | n.a. | 99.62 |
| Iso-2-7 | Ca-K-Zeolite | 41.70 | 25.87 | 0.37 | 0.00 | n.a. | 10.65 | 0.00 | 1.17 | 0.55 | 4.94 | n.a. | n.a. | 85.25 |
| Lz-x2 | Calcite | n.a. | n.a. | 0.00 | 0.00 | 0.00 | 55.29 | 0.00 | n.a. | n.a. | n.a. | n.a. | n.a. | 55.29 |
| Lz-x3 | Calcite | n.a. | n.a. | 0.00 | 0.00 | 0.00 | 55.44 | 0.00 | n.a. | n.a. | n.a. | n.a. | n.a. | 55.44 |
| | Calcite | n.a. | n.a. | 0.00 | 0.00 | 0.00 | 55.42 | 0.00 | n.a. | n.a. | n.a. | n.a. | n.a. | 55.42 |
| | K-Na-Ca-Sr-Zeolite | 50.06 | 22.20 | 0.00 | n.a. | 0.36 | 3.79 | 2.02 | n.a. | 3.38 | 5.38 | n.a. | 0.16 | 87.35 |
| | K-Na-Ca-Sr-Zeolite | 53.29 | 22.33 | 0.00 | n.a. | 0.43 | 3.71 | 1.49 | n.a. | 3.11 | 5.82 | n.a. | n.a. | 90.18 |
| | Ca-Sr-K-Na-Zeolite | 42.79 | 25.81 | 0.00 | n.a. | 0.00 | 5.96 | 4.61 | n.a. | 3.11 | 4.22 | n.a. | 0.36 | 86.86 |
| | Ca-Sr-K-Na-Zeolite | 44.31 | 24.64 | 0.18 | n.a. | 0.00 | 6.66 | 4.41 | n.a. | 2.55 | 3.98 | n.a. | 0.32 | 87.05 |
| | Ca-Sr-K-Na-Zeolite | 42.34 | 25.81 | n.a. | n.a. | 0.00 | 7.23 | 3.91 | n.a. | 3.19 | 3.23 | n.a. | 0.43 | 86.14 |
| | Ca-Zeolite | 37.25 | 29.61 | 0.28 | n.a. | 0.17 | 13.88 | 0.00 | n.a. | 0.42 | 1.26 | n.a. | n.a. | 82.87 |
| | Ca-Zeolite | 36.16 | 29.31 | 0.40 | n.a. | n.a. | 15.38 | 0.00 | n.a. | 0.20 | 0.23 | n.a. | n.a. | 81.68 |
| Lz-x6 | Calcite | n.a. | n.a. | 0.00 | 0.00 | n.a. | 55.40 | 0.00 | n.a. | n.a. | n.a. | n.a. | n.a. | 55.40 |
| Lz-x8 | Calcite | n.a. | n.a. | 0.22 | 0.00 | 0.00 | 55.22 | 0.00 | n.a. | n.a. | n.a. | n.a. | n.a. | 55.44 |
| Lz-g3 | Calcite | n.a. | n.a. | 0.00 | 0.00 | 0.00 | 55.54 | 0.00 | n.a. | n.a. | n.a. | n.a. | n.a. | 55.54 |
| host-3 | Calcite | n.a. | 0.00 | 0.00 | 0.00 | 0.00 | 55.37 | 0.00 | n.a. | n.a. | n.a. | 0.75 | n.a. | 56.12 |
| | Calcite | n.a. | 0.00 | 0.00 | 0.00 | 0.00 | 55.33 | n.a. | n.a. | n.a. | n.a. | n.a. | n.a. | 55.33 |
| | Ca-Sr-K-Na-Zeolite | 40.69 | 23.56 | 0.00 | n.a. | 0.18 | 7.93 | 3.50 | n.a. | 0.69 | 1.13 | n.a. | n.a. | 77.68 |
| | Ca-Sr-K-Na-Zeolite | 41.20 | 22.13 | 0.44 | n.a. | 0.28 | 7.04 | 3.47 | n.a. | 0.75 | 1.70 | n.a. | n.a. | 77.01 |
| | Ca-Sr-K-Na-Zeolite | 39.90 | 23.39 | 0.00 | n.a. | 0.18 | 7.57 | n.a. | n.a. | 0.94 | 1.23 | n.a. | n.a. | 73.21 |
| | Ca-Sr-K-Na-Zeolite | 40.63 | 22.92 | 0.00 | n.a. | 0.00 | 7.78 | n.a. | n.a. | 0.96 | 1.29 | n.a. | n.a. | 73.58 |
| | Ca-Zeolite | 32.88 | 27.68 | 0.22 | n.a. | n.a. | 14.02 | n.a. | n.a. | 0.00 | 0.00 | n.a. | n.a. | 74.80 |
| | Ca-Zeolite | 34.47 | 27.42 | 0.19 | n.a. | 0.23 | 13.85 | n.a. | n.a. | 0.31 | 0.14 | n.a. | n.a. | 76.61 |
| | Ca-K-Zeolite | 37.14 | 28.91 | 0.73 | n.a. | n.a. | 12.94 | n.a. | n.a. | 3.33 | 0.17 | n.a. | n.a. | 83.22 |
| | Ca-K-Zeolite | 37.70 | 27.64 | 1.04 | n.a. | n.a. | 12.10 | n.a. | n.a. | 3.13 | n.a. | n.a. | 0.28 | 81.89 |
| | Na-Zeolite | 53.72 | 21.94 | 0.75 | n.a. | 0.00 | 0.39 | n.a. | n.a. | 12.19 | 0.10 | n.a. | n.a. | 89.09 |
| | Na-Zeolite | 53.95 | 21.45 | 0.71 | n.a. | 0.00 | 0.55 | n.a. | n.a. | 11.32 | 0.16 | n.a. | n.a. | 88.14 |
| | Na-Zeolite | 52.91 | 21.65 | 0.58 | n.a. | 0.00 | 1.06 | n.a. | n.a. | 12.16 | 0.12 | n.a. | n.a. | 88.48 |
| | Na-Zeolite | 51.79 | 20.46 | 0.69 | n.a. | n.a. | 2.00 | n.a. | n.a. | 9.87 | 0.00 | 0.47 | n.a. | 85.28 |
| | Na-Zeolite | 54.45 | 21.60 | 1.02 | n.a. | n.a. | 0.39 | n.a. | n.a. | 11.61 | 0.11 | n.a. | n.a. | 89.18 |
| host-5 | Ca-Sr-K-Na-Zeolite | 41.42 | 23.96 | 0.00 | n.a. | n.a. | 6.88 | n.a. | n.a. | 0.66 | 1.07 | n.a. | n.a. | 73.99 |

See Fig. S3. n.a. – not analysed.

Table S5. Chemical composition (EDS, wt.%) of coexisting corundum and hematite from opaque segregation in plagioclase-clinopyroxene rock, Hatrurim Basin, Israel.

| Sample | Phase | *n* | $TiO_2$ | $Cr_2O_3$ | $V_2O_3$ | $Al_2O_3$ | $Fe_2O_3$ | FeO | MnO | MgO | CaO | NiO | Sum | $X_{Al2O3}$ | $X_{Fe2O3}$ |
|---|---|---|---|---|---|---|---|---|---|---|---|---|---|---|---|
| iso-1-g4 | Crn | *1* | 0.00 | 0.26 | n.a. | 92.50 | 7.45 | 0.00 | 0.00 | 0.00 | n.a. | n.a. | 100.21 | 0.95 | 0.05 |
| | Hem | *1* | 2.69 | 0.35 | 0.99 | 5.57 | 88.52 | 1.04 | 0.00 | 0.65 | 0.17 | 0.00 | 99.98 | 0.10 | 0.90 |
| iso-1-g4 | Crn | *1* | 0.00 | 0.00 | n.a. | 94.49 | 5.69 | 0.00 | 0.00 | 0.00 | n.a. | n.a. | 100.18 | 0.96 | 0.04 |
| | Hem | *1* | 1.72 | 0.50 | 0.76 | 4.74 | 91.33 | 0.39 | 0.00 | 0.50 | 0.21 | 0.00 | 100.15 | 0.09 | 0.91 |
| iso-1-g4 | Crn | *1* | 0.00 | 0.00 | n.a. | 95.74 | 4.43 | 0.00 | 0.00 | 0.00 | n.a. | n.a. | 100.17 | 0.97 | 0.03 |
| | Hem | *1* | 1.17 | 0.47 | 0.82 | 5.73 | 90.95 | 0.46 | 0.00 | 0.33 | n.a. | 0.00 | 99.93 | 0.10 | 0.90 |
| iso-1-g4 | Crn | *1* | 0.00 | 0.00 | n.a. | 94.89 | 5.18 | 0.00 | 0.00 | 0.00 | n.a. | n.a. | 100.07 | 0.97 | 0.03 |
| | Hem | *1* | 4.10 | 0.29 | 0.59 | 4.21 | 88.06 | 1.89 | 0.00 | 0.90 | 0.15 | 0.00 | 100.19 | 0.08 | 0.92 |
| iso-1-g4 | Crn | *1* | 0.00 | 0.00 | n.a. | 95.31 | 4.63 | 0.00 | 0.00 | 0.00 | n.a. | n.a. | 99.94 | 0.97 | 0.03 |
| | Hem | *1* | 3.00 | 0.41 | 0.65 | 2.72 | 90.80 | 1.25 | n.a. | 0.81 | 0.00 | 0.00 | 99.65 | 0.06 | 0.94 |
| iso-2-g | Crn | *1* | 0.00 | 0.00 | n.a. | 94.77 | 4.99 | 0.00 | 0.00 | 0.00 | n.a. | n.a. | 99.76 | 0.97 | 0.03 |
| | Hem | *1* | 1.67 | 0.35 | 0.47 | 3.85 | 92.91 | 0.06 | 0.00 | 0.65 | 0.22 | 0.00 | 100.18 | 0.07 | 0.93 |
| iso-2-g | Crn | *1* | 0.00 | 0.00 | n.a. | 94.81 | 5.19 | 0.00 | 0.00 | 0.00 | n.a. | n.a. | 100.00 | 0.97 | 0.03 |
| | Hem | *1* | 5.30 | 0.26 | 0.00 | 4.70 | 85.65 | 2.60 | 0.00 | 1.04 | 0.24 | 0.00 | 99.79 | 0.08 | 0.92 |
| iso-2-g | Crn | *2* | 0.00 | 0.00 | n.a. | 95.19 | 4.46 | 0.00 | 0.00 | 0.00 | n.a. | n.a. | 99.65 | 0.97 | 0.03 |
| | Hem | *1* | 1.55 | 0.35 | 0.19 | 5.03 | 92.34 | 0.00 | 0.00 | 0.65 | 0.18 | 0.00 | 100.29 | 0.08 | 0.92 |
| iso-2-g | Crn | *1* | 0.00 | 0.00 | n.a. | 94.69 | 5.23 | 0.00 | 0.00 | 0.00 | n.a. | n.a. | 99.92 | 0.97 | 0.03 |
| | Hem | *1* | 0.93 | 0.34 | 0.44 | 4.97 | 92.63 | 0.48 | 0.00 | n.a. | 0.28 | 0.00 | 100.07 | 0.09 | 0.91 |
| iso-2-g | Crn | *1* | 0.17 | 0.32 | n.a. | 90.98 | 8.21 | 0.15 | 0.00 | 0.00 | 0.00 | n.a. | 99.83 | 0.95 | 0.05 |
| | Hem | *1* | 3.32 | 0.35 | 0.26 | 3.10 | 90.43 | 1.77 | 0.00 | 0.48 | 0.28 | 0.00 | 99.99 | 0.06 | 0.94 |
| iso-2-g | Crn | *1* | 0.00 | 0.00 | n.a. | 95.62 | 4.55 | 0.00 | 0.00 | 0.00 | n.a. | n.a. | 100.17 | 0.97 | 0.03 |
| | Hem | *1* | 2.20 | 0.00 | 0.50 | 4.08 | 91.35 | 1.08 | 0.00 | 0.41 | 0.13 | 0.00 | 99.75 | 0.07 | 0.93 |
| iso-2-g2 | Crn | *1* | 0.00 | 0.16 | n.a. | 94.25 | 5.51 | 0.00 | 0.00 | 0.00 | 0.00 | n.a. | 99.92 | 0.96 | 0.04 |
| | Hem | *1* | 1.28 | 0.00 | 0.21 | 4.01 | 93.72 | 0.11 | 0.00 | 0.41 | 0.24 | 0.00 | 99.98 | 0.06 | 0.94 |
| iso-2-g2 | Crn | *1* | 0.18 | 0.37 | n.a. | 92.55 | 6.62 | 0.16 | 0.00 | 0.00 | n.a. | n.a. | 99.88 | 0.96 | 0.04 |
| | Hem | *1* | 5.00 | 0.26 | 0.44 | 3.70 | 87.36 | 0.72 | 0.22 | 1.69 | 0.18 | 0.32 | 99.89 | 0.07 | 0.93 |
| iso-2-g2 | Crn | *1* | 0.18 | 0.37 | n.a. | 93.49 | 5.78 | 0.16 | 0.00 | 0.00 | n.a. | n.a. | 99.98 | 0.96 | 0.04 |
| | Hem | *1* | 4.74 | 0.34 | 0.34 | 3.59 | 87.55 | 2.60 | 0.00 | 0.93 | n.a. | 0.00 | 100.09 | 0.07 | 0.93 |
| iso-2-g2 | Crn | *1* | 0.00 | 0.20 | n.a. | 94.10 | 5.95 | 0.00 | 0.00 | 0.00 | n.a. | n.a. | 100.25 | 0.96 | 0.04 |
| | Hem | *1* | 4.09 | 0.25 | 0.40 | 2.82 | 89.88 | 0.99 | 0.00 | 1.40 | 0.15 | 0.00 | 99.99 | 0.05 | 0.95 |
| iso-2-g2 | Crn | *1* | 0.00 | 0.32 | n.a. | 93.16 | 6.55 | 0.00 | 0.00 | 0.00 | n.a. | n.a. | 100.03 | 0.96 | 0.04 |
| | Hem | *1* | 4.70 | 0.39 | 0.24 | 1.70 | 89.42 | 2.21 | 0.00 | 1.03 | 0.14 | 0.00 | 99.83 | 0.04 | 0.96 |
| iso-4 | Crn | *2* | 0.20 | 0.35 | n.a. | 92.96 | 6.30 | 0.18 | 0.00 | 0.00 | n.a. | n.a. | 99.99 | 0.96 | 0.04 |
| | Hem | *2* | 3.06 | 0.47 | 0.26 | 3.88 | 90.64 | 0.19 | 0.00 | 1.31 | 0.18 | n.a. | 99.99 | 0.07 | 0.93 |
| iso-5 | Crn | *1* | 0.20 | 0.57 | n.a. | 94.02 | 5.05 | 0.18 | 0.00 | 0.00 | n.a. | n.a. | 100.02 | 0.97 | 0.03 |
| | Hem | *1* | 3.17 | 2.10 | 0.25 | 3.70 | 88.80 | 0.14 | 0.00 | 1.23 | 0.17 | 0.31 | 99.88 | 0.09 | 0.91 |
| iso-6 | Crn | *1* | 0.00 | 0.22 | n.a. | 94.13 | 5.88 | 0.00 | 0.00 | 0.00 | n.a. | n.a. | 100.23 | 0.96 | 0.04 |
| | Hem | *1* | 1.92 | 0.57 | 0.29 | 4.01 | 92.03 | 0.37 | 0.00 | 0.51 | 0.35 | 0.00 | 100.05 | 0.07 | 0.93 |
| iso-6 | Crn | *2* | 0.09 | 0.00 | n.a. | 95.37 | 4.53 | 0.08 | 0.00 | 0.00 | n.a. | n.a. | 100.06 | 0.97 | 0.03 |
| | Hem | *2* | 2.37 | 0.50 | 0.35 | 4.87 | 90.41 | 0.79 | 0.00 | 0.55 | 0.28 | n.a. | 100.11 | 0.09 | 0.91 |
| iso-6 | Crn | *1* | 0.00 | 0.20 | n.a. | 93.78 | 6.29 | 0.00 | n.a. | 0.00 | n.a. | n.a. | 100.27 | 0.96 | 0.04 |
| | Hem | *1* | 2.32 | 0.44 | n.a. | 2.08 | 93.69 | 0.35 | 0.00 | 0.73 | 0.34 | 0.00 | 99.95 | 0.04 | 0.96 |
| iso-6 | Crn | *1* | 0.00 | 0.35 | n.a. | 93.42 | 7.32 | 0.00 | 0.00 | 0.00 | n.a. | n.a. | 101.09 | 0.95 | 0.05 |
| | Hem | *1* | 3.05 | 0.48 | 0.24 | 2.10 | 92.30 | 0.42 | 0.00 | 1.06 | 0.34 | 0.00 | 99.99 | 0.04 | 0.96 |
| iso-6 | Crn | *1* | 0.00 | 0.00 | n.a. | 94.72 | 5.39 | 0.00 | 0.00 | 0.00 | n.a. | n.a. | 100.11 | 0.96 | 0.04 |
| | Hem | *1* | 2.29 | 0.44 | 0.35 | 5.29 | 89.96 | 1.01 | 0.00 | 0.38 | 0.29 | 0.00 | 100.01 | 0.09 | 0.91 |
| iso-8 | Crn | *3* | 0.00 | 0.53 | n.a. | 91.53 | 7.92 | 0.00 | 0.00 | 0.00 | n.a. | n.a. | 99.97 | 0.95 | 0.05 |
| | Hem | *1* | 2.04 | 0.57 | 0.63 | 1.72 | 93.88 | 0.03 | 0.21 | 0.65 | 0.17 | 0.22 | 100.13 | 0.04 | 0.96 |
| iso-9 | Crn | *3* | 0.19 | 0.13 | n.a. | 93.21 | 6.52 | 0.17 | 0.00 | 0.00 | 0.00 | n.a. | 100.22 | 0.96 | 0.04 |
| | Hem | *2* | 4.05 | 0.21 | 0.00 | 2.45 | 90.93 | 0.20 | 0.14 | 1.63 | 0.31 | n.a. | 99.89 | 0.04 | 0.96 |
| iso-10 | Crn | *3* | 0.00 | 0.32 | n.a. | 91.91 | 7.84 | 0.00 | 0.00 | 0.00 | n.a. | n.a. | 100.06 | 0.95 | 0.05 |
| | Hem | *1* | 2.65 | 0.39 | 0.26 | 4.44 | 90.75 | 0.36 | 0.27 | 0.98 | n.a. | 0.00 | 100.10 | 0.08 | 0.92 |
| iso-11 | Crn | *2* | 0.23 | 0.27 | n.a. | 90.63 | 8.90 | 0.20 | 0.00 | 0.00 | n.a. | n.a. | 100.23 | 0.94 | 0.06 |
| | Hem | *4* | 2.83 | 0.35 | 0.18 | 5.26 | 89.38 | 1.33 | 0.00 | 0.58 | 0.14 | n.a. | 100.05 | 0.09 | 0.91 |

n.a. – not analysed. $Fe_2O_3$ and FeO are calculated from charge balance.